Determination of the mass of the W boson using the DØ detector at the Fermilab Tevatron

B. Abbott,[30] M. Abolins,[27] B. S. Acharya,[45] I. Adam,[12] D. L. Adams,[39] M. Adams,[17] S. Ahn,[14] H. Aihara,[23] G. A. Alves,[10] E. Amidi,[31] N. Amos,[26] E. W. Anderson,[19] R. Astur,[44] M. M. Baarmand,[44] A. Baden,[25] V. Balamurali,[34] J. Balderston,[16] B. Baldin,[14] S. Banerjee,[45] J. Bantly,[5] E. Barberis,[23] J. F. Bartlett,[14] K. Bazizi,[41] A. Belyaev,[28] S. B. Beri,[36] I. Bertram,[33] V. A. Bezzubov,[37] P. C. Bhat,[14] V. Bhatnagar,[36] M. Bhattacharjee,[13] N. Biswas,[34] G. Blazey,[32] S. Blessing,[15] P. Bloom,[7] A. Boehnlein,[14] N. I. Bojko,[37] F. Borcherding,[14] C. Boswell,[9] A. Brandt,[14] R. Brock,[27] A. Bross,[14] D. Buchholz,[33] V. S. Burtovoi,[37] J. M. Butler,[3] W. Carvalho,[10] D. Casey,[41] Z. Casilum,[44] H. Castilla-Valdez,[11] D. Chakraborty,[44] S.-M. Chang,[31] S. V. Chekulaev,[37] L.-P. Chen,[23] W. Chen,[44] S. Choi,[43] S. Chopra,[26] B. C. Choudhary,[9] J. H. Christenson,[14] M. Chung,[17] D. Claes,[29] A. R. Clark,[23] W. G. Cobau,[25] J. Cochran,[9] W. E. Cooper,[14] C. Cretsinger,[41] D. Cullen-Vidal,[5] M. A. C. Cummings,[32] D. Cutts,[5] O. I. Dahl,[23] K. Davis,[2] K. De,[46] K. Del Signore,[26] M. Demarteau,[14] N. Denisenko,[14] D. Denisov,[14] S. P. Denisov,[37] H. T. Diehl,[14] M. Diesburg,[14] G. Di Loreto,[27] P. Draper,[46] Y. Ducros,[42] L. V. Dudko,[28] S. R. Dugad,[45] D. Edmunds,[27] J. Ellison,[9] V. D. Elvira,[44] R. Engelmann,[44] S. Eno,[25] G. Eppley,[39] P. Ermolov,[28] O. V. Eroshin,[37] V. N. Evdokimov,[37] T. Fahland,[8] M. Fatyga,[4] M. K. Fatyga,[41] S. Feher,[14] D. Fein,[2] T. Ferbel,[41] G. Finocchiaro,[44] H. E. Fisk,[14] Y. Fisyak,[7] E. Flattum,[14] G. E. Forden,[2] M. Fortner,[32] K. C. Frame,[27] S. Fuess,[14] E. Gallas,[46] A. N. Galyaev,[37] P. Gartung,[9] T. L. Geld,[27] R. J. Genik II,[27] K. Genser,[14] C. E. Gerber,[14] B. Gibbard,[4] S. Glenn,[7] B. Gobbi,[33] M. Goforth,[15] A. Goldschmidt,[23] B. Gómez,[1] G. Gómez,[25] P. I. Goncharov,[37] J. L. González Solís,[11] H. Gordon,[4] L. T. Goss,[47] K. Gounder,[9] A. Goussiou,[44] N. Graf,[4] P. D. Grannis,[44] D. R. Green,[14] J. Green,[32] H. Greenlee,[14] G. Grim,[7] S. Grinstein,[6] N. Grossman,[14] P. Grudberg,[23] S. Grünendahl,[41] G. Guglielmo,[35] J. A. Guida,[2] J. M. Guida,[5] A. Gupta,[45] S. N. Gurzhiev,[37] P. Gutierrez,[35] Y. E. Gutnikov,[37] N. J. Hadley,[25] H. Haggerty,[14] S. Hagopian,[15] V. Hagopian,[15] K. S. Hahn,[41] R. E. Hall,[8] P. Hanlet,[31] S. Hansen,[14] J. M. Hauptman,[19] D. Hedin,[32] A. P. Heinson,[9] U. Heintz,[14] R. Hernández-Montoya,[11] T. Heuring,[15] R. Hirosky,[15] J. D. Hobbs,[14] B. Hoeneisen,[1] J. S. Hoftun,[5] F. Hsieh,[26] Ting Hu,[44] Tong Hu,[18] T. Huehn,[9] A. S. Ito,[14] E. James,[2] J. Jaques,[34] S. A. Jerger,[27] R. Jesik,[18] J. Z.-Y. Jiang,[44] T. Joffe-Minor,[33] K. Johns,[2] M. Johnson,[14] A. Jonckheere,[14] M. Jones,[16] H. Jöstlein,[14] S. Y. Jun,[33] C. K. Jung,[44] S. Kahn,[4] G. Kalbfleisch,[35] J. S. Kang,[20] D. Karmgard,[15] R. Kehoe,[34] M. L. Kelly,[34] C. L. Kim,[20] S. K. Kim,[43] A. Klatchko,[15] B. Klima,[14] C. Klopfenstein,[7] V. I. Klyukhin,[37] V. I. Kochetkov,[37] J. M. Kohli,[36] D. Koltick,[38] A. V. Kostritskiy,[37] J. Kotcher,[4] A. V. Kotwal,[12] J. Kourlas,[30] A. V. Kozelov,[37] E. A. Kozlovski,[37] J. Krane,[29] M. R. Krishnaswamy,[45] S. Krzywdzinski,[14] S. Kunori,[25] S. Lami,[44] H. Lan,[14] R. Lander,[7] F. Landry,[27] G. Landsberg,[14] B. Lauer,[19] A. Leflat,[28] H. Li,[44] J. Li,[46] Q. Z. Li-Demarteau,[14] J. G. R. Lima,[40] D. Lincoln,[26] S. L. Linn,[15] J. Linnemann,[27] R. Lipton,[14] Y. C. Liu,[33] F. Lobkowicz,[41] S. C. Loken,[23] S. Lökös,[44] L. Lueking,[14] A. L. Lyon,[25] A. K. A. Maciel,[10] R. J. Madaras,[23] R. Madden,[15] L. Magaña-Mendoza,[11] S. Mani,[7] H. S. Mao,[14] R. Markeloff,[32] T. Marshall,[18] M. I. Martin,[14] K. M. Mauritz,[19] B. May,[33] A. A. Mayorov,[37] R. McCarthy,[44] J. McDonald,[15] T. McKibben,[17] J. McKinley,[27] T. McMahon,[35] H. L. Melanson,[14] M. Merkin,[28] K. W. Merritt,[14] H. Miettinen,[39] A. Mincer,[30] C. S. Mishra,[14] N. Mokhov,[14] N. K. Mondal,[45] H. E. Montgomery,[14] P. Mooney,[1] H. da Motta,[10] C. Murphy,[17] F. Nang,[2] M. Narain,[14] V. S. Narasimham,[45] A. Narayanan,[2] H. A. Neal,[26] J. P. Negret,[1] P. Nemethy,[30] D. Norman,[47] L. Oesch,[26] V. Oguri,[40] E. Oltman,[23] N. Oshima,[14] D. Owen,[27] P. Padley,[39] M. Pang,[19] A. Para,[14] Y. M. Park,[21] R. Partridge,[5] N. Parua,[45] M. Paterno,[41] B. Pawlik,[22] J. Perkins,[46] S. Peryshkin,[14] M. Peters,[16] R. Piegaia,[6] H. Piekarz,[15] Y. Pischalnikov,[38] V. M. Podstavkov,[37] B. G. Pope,[27] H. B. Prosper,[15] S. Protopopescu,[4] J. Qian,[26] P. Z. Quintas,[14] R. Raja,[14] S. Rajagopalan,[4] O. Ramirez,[17] L. Rasmussen,[44] S. Reucroft,[31] M. Rijssenbeek,[44] T. Rockwell,[27] N. A. Roe,[23] P. Rubinov,[33] R. Ruchti,[34] J. Rutherfoord,[2] A. Sánchez-Hernández,[11] A. Santoro,[10] L. Sawyer,[24] R. D. Schamberger,[44] H. Schellman,[33] J. Sculli,[30] E. Shabalina,[28] C. Shaffer,[15] H. C. Shankar,[45] R. K. Shivpuri,[13] M. Shupe,[2] H. Singh,[9] J. B. Singh,[36] V. Sirotenko,[32] W. Smart,[14] R. P. Smith,[14] R. Snihur,[33] G. R. Snow,[29] J. Snow,[35] S. Snyder,[4] J. Solomon,[17] P. M. Sood,[36] M. Sosebee,[46] N. Sotnikova,[28] M. Souza,[10] A. L. Spadafora,[23] R. W. Stephens,[46] M. L. Stevenson,[23] D. Stewart,[26] F. Stichelbaut,[44] D. A. Stoianova,[37] D. Stoker,[8] M. Strauss,[35] K. Streets,[30] M. Strovink,[23] A. Sznajder,[10] P. Tamburello,[25] J. Tarazi,[8] M. Tartaglia,[14] T. L. T. Thomas,[33] J. Thompson,[25] T. G. Trippe,[23] P. M. Tuts,[12] N. Varelas,[27] E. W. Varnes,[23] D. Vititoe,[2] A. A. Volkov,[37] A. P. Vorobiev,[37] H. D. Wahl,[15] G. Wang,[15] J. Warchol,[34] G. Watts,[5] M. Wayne,[34] H. Weerts,[27] A. White,[46] J. T. White,[47] J. A. Wightman,[19] S. Willis,[32] S. J. Wimpenny,[9] J. V. D. Wirjawan,[47] J. Womersley,[14] E. Won,[41] D. R. Wood,[31] H. Xu,[5] R. Yamada,[14] P. Yamin,[4] J. Yang,[30] T. Yasuda,[31] P. Yepes,[39] C. Yoshikawa,[16] S. Youssef,[15] J. Yu,[14] Y. Yu,[43] Q. Zhu,[30] Z. H. Zhu,[41] D. Zieminska,[18] A. Zieminski,[18] E. G. Zverev,[28] and A. Zylberstejn[42]

(DØ Collaboration)

[1]*Universidad de los Andes, Bogotá, Colombia*
[2]*University of Arizona, Tucson, Arizona 85721*
[3]*Boston University, Boston, Massachusetts 02215*
[4]*Brookhaven National Laboratory, Upton, New York 11973*
[5]*Brown University, Providence, Rhode Island 02912*
[6]*Universidad de Buenos Aires, Buenos Aires, Argentina*

[7]*University of California, Davis, California 95616*

[8]*University of California, Irvine, California 92697*

[9]*University of California, Riverside, California 92521*

[10]*LAFEX, Centro Brasileiro de Pesquisas Físicas, Rio de Janeiro, Brazil*

[11]*CINVESTAV, Mexico City, Mexico*

[12]*Columbia University, New York, New York 10027*

[13]*Delhi University, Delhi, India 110007*

[14]*Fermi National Accelerator Laboratory, Batavia, Illinois 60510*

[15]*Florida State University, Tallahassee, Florida 32306*

[16]*University of Hawaii, Honolulu, Hawaii 96822*

[17]*University of Illinois at Chicago, Chicago, Illinois 60607*

[18]*Indiana University, Bloomington, Indiana 47405*

[19]*Iowa State University, Ames, Iowa 50011*

[20]*Korea University, Seoul, Korea*

[21]*Kyungsung University, Pusan, Korea*

[22]*Institute of Nuclear Physics, Kraków, Poland*

[23]*Lawrence Berkeley National Laboratory and University of California, Berkeley, California 94720*

[24]*Louisiana Tech University, Ruston, Louisiana 71272*

[25]*University of Maryland, College Park, Maryland 20742*

[26]*University of Michigan, Ann Arbor, Michigan 48109*

[27]*Michigan State University, East Lansing, Michigan 48824*

[28]*Moscow State University, Moscow, Russia*

[29]*University of Nebraska, Lincoln, Nebraska 68588*

[30]*New York University, New York, New York 10003*

[31]*Northeastern University, Boston, Massachusetts 02115*

[32]*Northern Illinois University, DeKalb, Illinois 60115*

[33]*Northwestern University, Evanston, Illinois 60208*

[34]*University of Notre Dame, Notre Dame, Indiana 46556*

[35]*University of Oklahoma, Norman, Oklahoma 73019*

[36]*University of Panjab, Chandigarh 16-00-14, India*

[37]*Institute for High Energy Physics, 142-284 Protvino, Russia*

[38]*Purdue University, West Lafayette, Indiana 47907*

[39]*Rice University, Houston, Texas 77005*

[40]*Universidade do Estado do Rio de Janeiro, Brazil*

[41]*University of Rochester, Rochester, New York 14627*

[42]*CEA, DAPNIA/Service de Physique des Particules, CE-SACLAY, Gif-sur-Yvette, France*

[43]*Seoul National University, Seoul, Korea*

[44]*State University of New York, Stony Brook, New York 11794*

[45]*Tata Institute of Fundamental Research, Colaba, Mumbai 400005, India*

[46]*University of Texas, Arlington, Texas 76019*

[47]*Texas A&M University, College Station, Texas 77843*

A measurement of the mass of the W boson is presented which is based on a sample of 5982 $W \to e\nu$ decays observed in $p\bar{p}$ collisions at $\sqrt{s}=1.8$ TeV with the DØ detector during the 1992–1993 run. From a fit to the transverse mass spectrum, combined with measurements of the Z boson mass, the W boson mass is measured to be $M_W = 80.350 \pm 0.140(\text{stat}) \pm 0.165(\text{syst}) \pm 0.160(\text{scale})$ GeV/c^2. Detailed discussions of the determination of the absolute energy scale, the measured efficiencies, and all systematic uncertainties are presented. [S0556-2821(98)01613-0]

PACS number(s): 14.70.Fm, 12.15.Ji, 13.38.Be, 13.85.Qk

I. INTRODUCTION

Among electroweak measurables, the mass of the W boson M_W is of crucial importance. Along with the determination of the mass of the top quark [1,2] and in conjunction with other precisely determined quantities, including the mass of the Z boson M_Z, the electroweak standard model [3] is constrained. This paper discusses the details of the first measurement of M_W by the DØ Collaboration using data from the 1992–1993 running of the Fermilab Tevatron Collider. It includes essential calibrations which will be used in future DØ measurements. A first report of this measurement was published in Ref. [4].

An early success of the CERN $p\bar{p}$ collider was the dis-

covery and measurement of the masses of both the W and Z bosons [5–7]. Table I gives a history of the published values of the direct measurements of M_W. The approach taken in this analysis is similar to those of the UA2 [12] and Collider Detector at Fermilab (CDF) [14,15] experiments.

For the physics of W bosons, the electroweak measurables of interest are M_W and $\sin^2 \theta_W$, where θ_W is the weak mixing angle. Both can be measured precisely and can be predicted from the lowest order relations of the model [17]:

$$M_W = M_Z \cos \theta_W \tag{1}$$

$$\alpha_{\mathrm{EM}} = \frac{g^2 \sin^2 \theta_W}{4\pi} \tag{2}$$

$$\frac{G_\mu}{\sqrt{2}} = \frac{g^2}{8M_W^2}. \tag{3}$$

Here, α_{EM} is the fine structure constant, g is the gauge coupling associated with the $\mathrm{SU(2)}_L$ gauge group, and G_μ is the Fermi coupling constant. The weak coupling, the electric charge, and the weak mixing angle are related by $\tan \theta_W = g'/g$, where g' is the coupling of the $\mathrm{U(1)}$ gauge group.

The standard set of measurable input parameters is the following:

$$\alpha_{\mathrm{EM}} = 1/(137.0359895 \pm 0.0000061) \tag{4}$$

$$G_\mu = 1.16639(\pm 0.00002) \times 10^{-5} \ \mathrm{GeV}^{-2} \tag{5}$$

$$M_Z = 91.1884 \pm 0.0022 \ \mathrm{GeV}/c^2. \tag{6}$$

The fine structure constant is measured from the quantum Hall effect [18]; the Fermi coupling constant is measured from the muon lifetime [18], and M_Z is measured directly by the combined experiments at the CERN $e^+ e^-$ collider LEP [19].

In order to confront the model beyond the lowest order, a self-consistent theoretical scheme for dealing with the effects of higher orders of perturbation theory is required. Different theoretical prescriptions motivate particular definitions of the weak mixing angle. The determination of M_W and the ratio of neutral to charged current cross sections in deep inelastic neutrino scattering are most naturally interpreted in terms of the "on shell" scheme [20] in which the weak mixing angle is defined by Eq. (1) with both masses as measurable quantities.

Within a given scheme, radiative corrections are most easily included through the use of a single measurable parameter, Δr, which is analogous to $(g-2)$ in quantum electrodynamic radiative corrections. Like $(g-2)$, Δr can be determined experimentally and its measurement can be directly compared with its theoretical prediction. In the leading log approximation, it can be written in terms of M_W as

$$\Delta r = 1 - \frac{\pi \alpha_{\mathrm{EM}}/\sqrt{2}}{G_\mu M_Z^2 (M_W/M_Z)^2 [1 - (M_W/M_Z)^2]}. \tag{7}$$

Roughly 90% of the value of Δr is due to light quark loop corrections to α_{EM}, while the balance is due to the embedded physics of heavy quarks and the Higgs boson. Any physics beyond the Higgs boson and known heavy quarks would also contribute to Δr. Prior to the measurement described here, the world average of M_W ($M_W = 80.33 \pm 0.170$ GeV/c^2), M_Z [19], and Eq. (7), results in $\Delta r = 0.0384 \pm 0.0100$, which is 3.8σ from the tree level prediction.

Because Δr is dominated by QED corrections, it is interesting to separate out those "residual" effects which are distinguishable from electrodynamic effects alone. Such a separation isolates possible new physics as well as physics directly associated with the top quark and the Higgs boson. A prescription for doing this has been suggested by defining $(\Delta r)_{\mathrm{res}}$ [21],

$$\frac{\alpha_{\mathrm{EM}}}{1 - \Delta r} = \frac{\alpha_{\mathrm{EM}}(M_Z^2)}{1 - (\Delta r)_{\mathrm{res}}}. \tag{8}$$

With a determination of Δr plus a separate evaluation of $\alpha_{\mathrm{EM}}(M_Z^2)$ [22], $(\Delta r)_{\mathrm{res}}$ can be extracted. Evaluation of this quantity makes a particularly economical probe of the standard model possible.

A. Plan of the DØ measurement

The DØ detector is a calorimetric detector with nearly full kinematical coverage for electrons, hadrons, and muons. The inner tracking region does not include a magnetic field. Calibration of the electromagnetic, and by extension the hadronic, calorimeter was accomplished by exposing calorimeter

TABLE I. Previously published hadron collider measurements of M_W. In each case the first uncertainty listed is statistical, the second is systematic, and the third is due to energy scale. For the latest CDF values, the energy scales have been incorporated into the total systematic uncertainty.

Experiment	Channel	M_W (GeV/c^2)
UA1(1983) [5]	$e\nu$	81 ± 5
UA2(1983) [6]	$e\nu$	80^{+10}_{-6}
UA1(1986) [8]	$e\nu$	$83.5^{+1.1}_{-1.0} \pm 2.7$
UA2(1987) [9]	$e\nu$	$80.2 \pm 0.6 \pm 0.5 \pm 1.3$
UA1(1989) [10]	$e\nu$	$82.7 \pm 1.0 \pm 2.7$
UA2(1990) [11]	$e\nu$	$80.49 \pm 0.43 \pm 0.24$
UA2(1992) [12]	$e\nu$	$80.35 \pm 0.33 \pm 0.17$
CDF(1989) [13]	$e\nu$	$80.0 \pm 3.3 \pm 2.4$
CDF(1990) [14]	$e\nu$	$79.91 \pm 0.35 \pm 0.24 \pm 0.19$
CDF(1995) [15]	$e\nu$	$80.490 \pm 0.145 \pm 0.175$
UA1(1984) [16]	$\mu\nu$	81^{+6}_{-7}
UA1(1989) [10]	$\mu\nu$	$81.8^{+6.0}_{-5.3} \pm 2.6$
CDF(1990) [14]	$\mu\nu$	$79.90 \pm 0.53 \pm 0.32 \pm 0.08$
CDF(1995) [15]	$\mu\nu$	$80.310 \pm 0.205 \pm 0.130$
UA1(1989) [10]	$\tau\nu$	$89 \pm 3 \pm 6$
CDF(1990) [14]	$e\nu + \mu\nu$	79.91 ± 0.39
CDF(1995) [15]	$e\nu + \mu\nu$	80.410 ± 0.180

test modules to charged particle beams of known energies and compositions, as well as *in situ* decays of known particles. The D0 determination of M_W relies on the determination of the mass ratio M_W/M_Z and the subsequent scaling of this ratio by the precisely determined M_Z from LEP [19]. This approach is similar to that of the UA2 experiment [12]. The significant advantage of determining M_W/M_Z is that a number of systematic uncertainties cancel in the ratio. This paper addresses those in detail.

The production and decay characteristics of W bosons in a $p\bar{p}$ collider present a variety of challenges which drive the analysis strategy. Because the statistical power of this measurement is at the level of less than 150 MeV/c^2 ($<0.2\%$), it is necessary to understand both the experimental and theoretical systematic uncertainties to a precision comparable to this level. The Z boson data are used for studying many of the experimental uncertainties, so the total uncertainty of an M_W determination is strongly coupled with the size of the Z boson data set. Hence, future determinations will gain in statistical and systematic precision with the sizes of both the W and Z boson data sets.

Uncertainties in modeling the production of W and Z bosons present a different set of challenges which do not necessarily scale with the number of events. For example, at Tevatron energies roughly 80% of the annihilations which produce W bosons involve sea quarks. Additionally, the substantial probability of gluon radiation from the initial state quarks results in significant transverse momentum of the W boson. Both of these theoretical issues involve uncertainties which complicate the simulation.

For the Z boson the observables come from the reaction chain:

$$p\bar{p} \rightarrow Z(\rightarrow e^+ + e^-) + \mathcal{H}_Z(\rightarrow \text{hadrons}), \qquad (9)$$

where $\mathcal{H}_Z$ is the hadronic recoil against the transverse motion of the Z boson. Both electrons are fully measured and the dielectron mass is determined from

$$M_Z = \sqrt{2E^{e_1}E^{e_2} - 2\vec{p}^{e_1}\cdot\vec{p}^{e_2}}. \qquad (10)$$

With the D0 detector, the electron decay mode of the W boson leads to the most precise mass determination. This is due to the cleaner signal and better resolution, as compared to the muon or tau decay modes. In this experiment, the single relevant channel is $W \rightarrow e\nu_e$. The electrons are emitted with transverse momenta p_T^e of order 40 GeV/c and the neutrino is emitted with a comparable momentum, escaping without detection. This leaves a large component of missing energy $\not{E}$ in the event of which only the transverse component, $\not{E}_T$ is determined. Therefore, the defining characteristics of W bosons are a high p_T electron accompanied by significant $\not{E}_T$.

The observable quantities for this measurement come from the W boson production and decay chain:

$$p\bar{p} \rightarrow W(\rightarrow e + \nu) + \mathcal{H}_W(\rightarrow \text{hadrons}), \qquad (11)$$

where $\mathcal{H}_W$ is the hadronic recoil against the transverse motion of the W boson. Since a complete characterization of the

neutrino 4-momentum is impossible, the only quantities directly measured are the electron momentum and the transverse momentum of the recoil $\vec{p}_T^{rec}$.

Using these measurables, the two body kinematics of this decay provide at least two methods for measuring M_W. The transverse energy spectrum of the electron will exhibit a kinematical edge (the "Jacobian edge") at $M_W/2$ for W bosons with transverse momentum p_T^W equal to zero. However, resolution effects and nonzero values of p_T^W smear the p_T^e and $\not{E}_T$ spectra and therefore affect the use of the sharp edge as a measure of M_W.

To control the systematic effects while retaining the highest statistical precision, the "transverse mass" is used to determine M_W. It is defined as [23]

$$M_T^2 = 2E_T^e E_T^\nu - 2\vec{p}_T^e\cdot\vec{p}_T^\nu = 2E_T^e E_T^\nu(1 - \cos\phi_{e\nu}), \qquad (12)$$

where p_T^ν is the transverse momentum of the neutrino and $\phi_{e\nu}$ is the azimuthal angle between the electron and neutrino [24]. The transverse mass also exhibits a Jacobian edge, but at the value of M_W and with much less sensitivity to p_T^W. Hence, precise determination of the location of this edge determines M_W. The effect of both the finite width $\Gamma(W)$ and p_T^W does distort the shape of the M_T spectrum [25]. While the transverse momentum of the W boson is relatively low, peaking at approximately $p_T^W \sim 5$ GeV/c in this analysis, even this small amount can be significant.
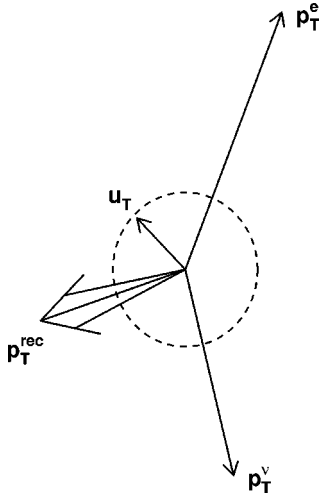
Equation (12) shows that the necessary ingredients for determining M_T are $\vec{p}_T^e$, $\vec{p}_T^\nu$, and the angle between them. Among these, only $\vec{p}_T^e$ is determined directly. Since momentum transverse to the beam is conserved, a measured imbalance can be attributed to the neutrino. Therefore, in the absence of detector effects, the neutrino transverse energy is equal to the missing transverse energy and calculated from the measured $\vec{p}_T^{rec}$ and $\vec{p}_T^e$,

$$\vec{p}_T^\nu \equiv \not{\vec{E}}_T = -\vec{p}_T^{rec} - \vec{p}_T^e. \qquad (13)$$

However, the reaction given in Eq. (11) does not fully describe the situation since energy measurement in a calorimeter includes other effects. Energy lost in detector cracks and inefficiencies can introduce biases in the magnitude and direction of the total energy. The interactions of the remaining spectator quarks in the proton and antiproton will add energy, as will noise and "pileup" due to the residual energy from multiple interactions. Designating these additional, non-recoil, luminosity dependent contributions the "underlying event," $\vec{u}_T(\mathcal{L})$, the measured neutrino transverse momentum is given by

$$\not{\vec{E}}_T = -\vec{p}_T^{rec} - \vec{u}_T(\mathcal{L}) - \vec{p}_T^e$$

$$= -[\vec{p}_T^{rec} + \vec{u}_T^{rec}(\mathcal{L})] - [\vec{u}_T^e(\mathcal{L}) + \vec{p}_T^e]. \qquad (14)$$

The underlying event contributions which are under the electron and the hadronic recoil are separately denoted as $\vec{u}_T^e(\mathcal{L})$ and $\vec{u}_T^{rec}(\mathcal{L})$. They are dependent on the instantaneous luminosity. Overall, the two quantities within the brackets are not distinguished from one another in the measurement

FIG. 1. Kinematic quantities for *W* events.

but must be dealt with in the analysis. Figure 1 shows the kinematics of the *W* boson events.

Since there is no analytic description of the transverse mass distribution, determination of M_W relied on modeling the transverse mass spectrum through a Monte Carlo simulation. The *W* boson mass was extracted by comparing the measured distribution in transverse mass to the Monte Carlo distribution generated for different *W* boson masses. The simulation relied on experimental data as much as possible and used *Z* boson events, not only to set the energy scale, but also to understand the electron energy resolution, the energy underlying the *W* boson, and the scale in p_T^W. In the simulation *W* bosons were generated with a relativistic Breit-Wigner line shape that was skewed by the mass dependence of the parton luminosities. The longitudinal and transverse momentum spectrum were given by a double differential distribution calculated to next-to-leading order.

The decay products and the *W* boson recoil system were traced through the simulated detector with resolution smearing. Minimum bias events (collisions which are recorded with little or no trigger bias) mimic the debris in the event produced by the spectator quarks and pileup associated with multiple interactions. The minimum bias events also properly included residual energy from previous crossings. The generated spectra in transverse mass for different values of M_W were compared to the measured spectra by a maximum likelihood method, and the best fit value of the mass obtained.

The measurements reported in this paper are: M_W, as determined from fits to the M_T distribution and fits to the p_T^e and p_T^ν distributions and M_W/M_Z. In addition Δr and $(\Delta r)_{res}$ are determined.

The paper is organized as follows:

Section II: a brief description of the detector;
Section III: data collection, reconstruction, the corrections applied to the data and the selection of the final sample;
Section IV: determination of the parameters used in the Monte Carlo simulation;

Section V: Monte Carlo simulation;
Section VI: results of the fits;
Section VII: effects of systematic errors due to the parameters determined in Sec. IV and the assumptions described in Sec. V;
Section VIII: consistency checks;
Section IX: conclusions;
Appendix A: *W* boson and *Z* boson production model;
Appendix B: bremsstrahlung; and
Appendix C: mean number of interactions.

II. DØ DETECTOR AND TRIGGER SYSTEM

The data collected for this measurement were taken during the exposure of the DØ detector to collisions of protons and antiprotons at a center of mass energy of $\sqrt{s} = 1800$ GeV in the 1992–1993 running period of the Fermilab Tevatron collider. This was the first beam exposure of this experiment and the total luminosity accumulated was 12.8 pb^{-1}. The average instantaneous luminosity was $\mathcal{L} = 3.4 \times 10^{30}$ cm^{-2} s^{-1}, which corresponded to less than 1 collision per crossing which occurs for $\mathcal{L} \sim 6 \times 10^{30}$ cm^{-2} s^{-1}.

The DØ detector was designed to study a variety of high transverse momentum physics topics and has been described in detail elsewhere [26]. The detector has nearly full acceptance for electrons, photons, and muons and measures jets, electromagnetic (EM) showers, and $\not{E}_T$ with good resolution [27]. The detector consists of three major subsystems: a tracking system, uranium-liquid argon calorimeters, and a muon toroidal spectrometer. The components of the detector which are most relevant to this analysis are briefly described below.

A. Tracking system

The tracking system was used to reconstruct charged particle tracks over the region $|\eta| < 3.2$ [28] and to reconstruct the interaction vertex of the event. It consists of four subsystems: a drift chamber surrounding the vertex region (VTX), a transition radiation detector (TRD), a central drift chamber (CDC) and two forward drift chambers (FDC). The VTX, TRD, and CDC cover the large angle region and are oriented parallel to the beam axis. The FDC's cover the small angle region and are oriented perpendicular to the beam axis. In addition to the $r\phi$ measurement of hits in the CDC, delay lines were used to measure track hit locations in the *z* direction. The TRD provides an independent identification of electrons, in addition to that provided by the calorimeters, allowing enhanced hadron rejection.

B. Calorimeters

The calorimeter system consists of one central (CC) and two end (EC) calorimeters which measure the energy flow in the event over a pseudorapidity range $|\eta| \leq 4.2$. The calorimeters are enclosed in three separate cryostats which surround the tracking system. They each have an electromagnetic, a fine hadronic (FH), and a coarse hadronic (CH) section. Liquid argon is employed as the active medium and uranium is the absorber material in the EM and FH sections and copper
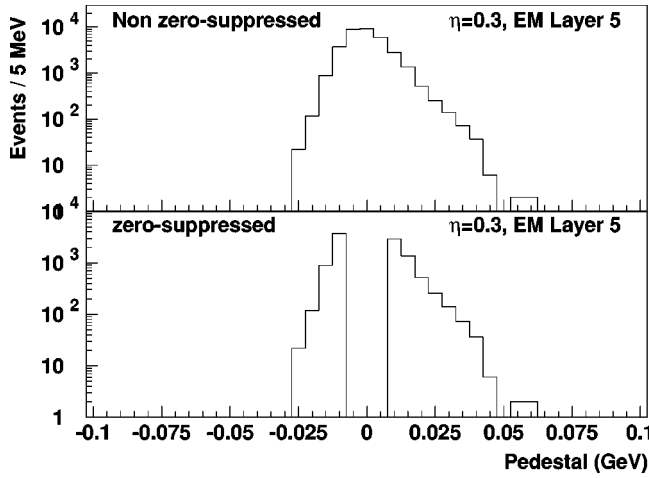
FIG. 2. Pedestal distribution of a typical electromagnetic calorimeter readout tower before and after zero-suppression.

(steel) is the absorber in the CH section for the CC (EC). The inter-cryostat region (ICR) is instrumented with scintillator tile detectors which are located in the space between the EC and CC cryostats. These detectors were used to improve the energy measurement of jets that straddle two calorimeters.

The calorimeters are arranged in a cylindrical geometry with each EM section being divided into four longitudinal readout layers, for a total depth of 21 radiation lengths. A projective tower arrangement for readout points toward the interaction region. The hadronic sections are 7–9 nuclear interaction lengths deep and are divided into four (CC) or five (EC) longitudinal readout layers. The transverse segmentation of the calorimeters is 0.1×0.1 in $\Delta \eta \times \Delta \phi$, except in the third layer of the EM calorimeter which is at shower maximum, where it is 0.05×0.05 in $\Delta \eta \times \Delta \phi$. Measured resolutions will be discussed below.

Under normal running conditions, calorimeter cells were not read out if the signal was within 2σ of the pedestal for that channel. That is, the readout was zero-suppressed. The pedestal is taken to be the mean of the energy distribution when no interactions occur. Due to a convolution of the shaping electronics and the natural radioactivity of uranium, the pedestal distributions are asymmetric with a long tail towards positive energies. (See Fig. 2.) Therefore, even when no particle strikes a read-out tower, the energy registered for that tower will on average not be zero. Great care has to be exercised in the event modeling in order to properly address these issues. This will be discussed in detail below.

C. Muon spectrometer

The muon spectrometer provides identification and momentum determination for muons. It surrounds the calorimeters and consists of planes of proportional drift tubes which surround magnetized iron toroids and covers a region $|\eta| < 3.3$. There is one layer of proportional tubes on the inner face of the magnet and two layers, separated by ≈ 1 m, outside the magnet. The material in the calorimeter and iron toroids is about 12 interaction lengths thick, making hadronic punch-through to the outer two layers negligible. The muon momentum resolution is $\sigma(1/p) = 0.18(p-2)/p^2 \oplus 0.008$ (momentum p in GeV/c).

D. Triggers

The Tevatron beam crossings occurred every 3.5 μs. For a $p\bar{p}$ total cross section at $\sqrt{s} = 1.8$ TeV of approximately 70 mb [29], there is an interaction rate of ≈ 200 kHz at a typical instantaneous luminosity of 3×10^{30} cm^{-2} s^{-1}. In order to record events at ≈ 2 Hz, three stages of hardware and software triggers were used.

To indicate the presence of a collision within the detector and to calculate a fast approximation to the vertex position, radial scintillation hodoscope arrays are positioned in the forward directions subtending angles of $2.3 < |\eta| < 3.9$. To pass the level 0 (L0) hardware trigger, coincident hits in these counters were required on both sides of the interaction region, signaling an inelastic collision within the detector volume and also providing an estimate of the z position of the interaction vertex. This trigger provided the minimum bias data set used in this analysis. The trigger rate depended on the luminosity and for the data analyzed here, was typically 90 kHz.

Events passing the L0 trigger were then passed to the level 1 (L1) hardware trigger. Here a decision was made based on the fast analog sums of all the EM layer calorimeter signals which represent the energies in trigger towers. These towers were segmented as 0.2×0.2 in $\Delta \eta \times \Delta \phi$ with coverage extending to $|\eta| < 3.2$. The L1 electronics restricted the maximum trigger rate to ≈ 200 Hz and decisions made by it and by the L0 trigger were made between beam crossings.

The final stage of triggering was the level 2 (L2) software trigger which ran on a farm of 48 VAXstation 4000 M60 processors. The typical processing time for an event in L2 was 350 μs, resulting in an average deadtime of $\approx 2\%$. The full segmentation of the calorimeter was available at this trigger level and a full event reconstruction was done, albeit with simplified algorithms and coarser segmentation. There were 32 different L1 components and 128 different L2 components which could be constructed and prescaled at different rates. Each logical combination targeted specific physics for given accelerator conditions. These data sets were written out to corresponding output data streams.

1. Trigger requirements for the W boson and Z boson data sets

For the determination of the W boson mass, the electron decay modes were required for the selection of both W and Z bosons. While the characteristics of both are similar—the presence of high transverse momentum electrons—the different rates and backgrounds require distinct selection criteria. Because of the presence of a neutrino in W boson decay events, a minimal $\not{E}_T$ requirement was used in the selection of W boson candidates.

To select electrons, the L1 trigger required the transverse energy in the EM layers of a trigger tower to be above a preselected threshold. For the selection of W boson events, the L1 trigger required at least one EM trigger tower above 10 GeV. For Z boson events, at least two EM trigger towers

TABLE II. L1 and L2 trigger requirements for *W* and *Z* event data samples. Here, f_{iso} is defined by Eq. (16).

	$W \rightarrow e\nu$ candidates	$Z \rightarrow ee$ candidates
L1 trigger requirements	1 EM tower with $E_T > 10$ GeV	2 EM towers with $E_T > 7$ GeV
L2 filter requirements	1 EM cluster with $E_T > 20$ GeV	2 EM clusters with $E_T > 10$ GeV
	$f_{\mathrm{iso}} < 0.15$	$f_{\mathrm{iso}} < 0.15$
	$\not{E}_T > 20$ GeV	

with $E_T > 7$ GeV were required.

The L2 electron algorithm used the full segmentation of the EM calorimeter to measure the energy deposited by the EM shower and is described in detail in Ref. [27]. Trigger towers above threshold were used as seeds to form energy clusters which included all calorimeter cells in the four EM layers and the first FH layer in a window $\Delta\eta \times \Delta\phi = 0.3 \times 0.3$. For the selection of *W* events, an energy cluster with $E_T > 20$ GeV was required by the L2 filter. For *Z* boson event candidates, two energy clusters, each with $E_T > 10$ GeV, were required by the L2 filter. Transverse and longitudinal shape requirements as well as isolation requirements were also placed on the energy cluster for the selection of *W* boson events.

The $\not{E}_T$ in the event was calculated in the L2 trigger and was required to be above 20 GeV for the *W* boson event selection. It was computed using the vector sum of the E_T of all the cells in the calorimeter and the ICD with respect to the *z* position of the interaction vertex, determined by L0. Prescaled triggers of *W* boson events were also recorded without the $\not{E}_T$ trigger requirement in order to study efficiencies and biases. This trigger is essentially an isolated electron or photon trigger. Table II lists a summary of the trigger requirements used in the selection of the *W* boson and *Z* boson data samples.

2. Main Ring veto

The 150 GeV/c conventional accelerator (main ring) passed through the coarse hadronic part of the DØ calorimeters. Halo particles accompanying the circulating beam can deposit energy in the calorimeter and corrupt measurements both at the trigger and offline reconstruction levels. Such unrelated energy depositions in a localized part of the detector will affect the $\not{E}_T$ determination and therefore considerable care was required in the utilization of triggers taken while the Main Ring beam passed through the detector. A veto gated on the injection period of the main ring cycle (the first 0.4 s of the 2.4 s cycle) was used in some of the L2 filters to avoid any adverse effects. For the mass analysis, all $Z \rightarrow ee$ events were used; $Z \rightarrow ee$ candidates recorded during the veto of the main-ring period were excluded from resolution studies. No *W* boson events were taken from triggers occurring during the main ring cycle.

III. *W* AND *Z* BOSON DATA SAMPLE: EVENT SELECTION AND DATA PROCESSING

A. Offline data processing and candidate event selection

Once data were written to tape, the digitized information was converted using an initial calibration. The initial calibra-

tion of the CDC was based on measurements using cosmic ray data. The calibration of the delay lines of the CDC, measuring the *z* coordinate of the hits, was derived from pulser measurements on the bench combined with cosmic ray data. The initial calibration of the calorimeter was obtained from test beam measurements [26]. Corrections to the calorimeter calibration were required, including corrections for an adjustment to the operating voltage of the calorimeter, corrections to the sampling weights, and to the gains of individual calorimeter cells. In addition, a correction due to a difference in liquid argon temperature at the test beam and DØ was applied [30]. It should be noted that none of the central EM calorimeter modules that were tested were installed in the final calorimeter.

The azimuthal uniformity of the central electromagnetic calorimeter was determined using approximately 3.5 million triggers from an inclusive electron data sample [31]. By equalizing the event rate above a 13 GeV threshold for each calorimeter module, relative calibration constants were determined to an accuracy of 0.5%, assuming that the observed ϕ variations were instrumental in origin. These relative calibration constants showed a variation in the response between different modules with a maximum difference of 5%. The variations were dependent on which of the 32 EM modules was struck by the electron, and not by other features of the calorimeter such as a variation in the amount of material in the tracking detector. All of the above corrections to the energy are propagated into the $\not{E}_T$ calculation.

1. EM clustering

Electrons and photons were reconstructed as energy clusters in the EM and first FH section of the calorimeter. Towers were defined by adding the energy measured by the calorimeter in all four EM layers plus the first FH layer for cells within 0.1×0.1 in $\Delta\eta \times \Delta\phi$. Towers were grouped together with their adjacent neighbors, provided their energies are above 50 MeV. Clusters of adjacent calorimeter towers with significant energy depositions were then formed using a nearest neighbor clustering algorithm [32].

The observed energy of the EM cluster is given by

$$E^{\mathrm{meas}} = \delta^{TB} + C \sum_i \beta_i S_i \qquad (15)$$

where δ^{TB} is an offset in the energy response due to energy loss in the material upstream of the test calorimeter. C is the conversion constant from the digital signal to energy and β_i are the sampling weights for the ith layer with energy deposition (in ADC counts) S_i. The sum runs over all five layers

in the EM calorimeter which contribute to the EM cluster. Both β_i and δ^{TB} were determined from test beam measurements using electron beams over a broad range of energy and rapidity. From these test beam measurements, the offset was determined to be $\delta^{TB} = 347$ MeV. This level of energy scale determination, based on the test beam measurements and taking into account corrections due to the transfer of the calibration from the test beam to D∅, resulted in an energy scale approximately 5% lower than the nominal energy scale for the central calorimeter, as observed from the measured Z boson mass. Both the final overall energy scale and the offset were re-computed *in situ*, as will be discussed in the next section.

2. Electron identification

Electrons were identified by a combination of topological and kinematic identifiers as described in [27]. The main electron identification requirements are below.

The cluster shower shape can be characterized by both longitudinal and lateral energy depositions. The fraction of the cluster energy which is deposited in the EM calorimeter is defined as f_{EM}. Since charged hadrons deposit less than $\approx 10\%$ of their energy in the EM calorimeter, f_{EM} provides a powerful discriminant. f_{EM} was required to be greater than 90%.

The electron candidate cluster was required to have a topology, both longitudinal and lateral, which was consistent with that of electrons from a detailed GEANT Monte Carlo simulation [33] which was extensively compared to test beam measurements. A covariance matrix of 41 observables was defined to characterize an electron shower [27]. A χ^2 parameter was defined to measure the consistency of the shower with that expected for electrons. For central electrons a $\chi^2 < 100$ was required; for electrons in the end calorimeters $\chi^2 < 200$ was imposed. These requirements were $\approx 94\%$ efficient. A rejection factor of about 4 against EM clusters that are not due to single electrons was achieved.

Electrons from W and Z boson decays tend to be isolated from other particles in the electromagnetic calorimeter. An offline isolation requirement was used which is defined as

$$f_{iso} = \frac{E_{tot}(R_4) - E_{EM}(R_2)}{E_{EM}(R_2)} \qquad (16)$$

where E_{tot} is the total energy in cone of radius $R_4 = 0.4$ in $\eta \times \phi$-space. E_{EM} is the EM energy in a cone of radius $R_2 = 0.2$. An isolation requirement of $f_{iso} < 0.15$ was placed on the cluster energies for electrons from both W and Z boson event candidates.

An important source of background for electrons is photons from π^0 or η meson decays which are adjacent to unrelated tracks. This background was reduced by requiring that a track from a charged particle in the tracking detector be consistent with the position of the cluster in the calorimeter. To qualify as a match, the shower centroid was required to link with a reconstructed track with significance σ_{trk},

$$\sigma_{trk} \equiv \sqrt{\left(\frac{R\Delta\varphi}{\sigma_{R\Delta\varphi}}\right)^2 + \left(\frac{\Delta z}{\sigma_z}\right)^2} \qquad (17)$$

where $R\Delta\varphi$ and Δz are the spatial mismatches between the track projection and cluster position in the φ and z directions, respectively, and $\sigma_{R\Delta\varphi}$ and σ_z are the associated experimental resolutions. For the data set used in this analysis $\sigma_{trk} < 10$ was imposed for CC electron candidates. This cut was used to minimize bias and results in an efficiency of $>98\%$ [34].

3. Electron direction determination

The optimum resolution in the electron polar angle is obtained using the z position of the electron cluster as obtained from the calorimeter information and the z position of the center-of-gravity (*cog*) of the CDC track. These two points thus define the polar angle of the electron. The position of an electron in the calorimeter was determined from the energy depositions in the third EM layer of the shower using a $\log(E)$ energy weighting algorithm [35]. The parameters of the algorithm were determined using both test beam and Monte Carlo data. Further study with collider data demonstrated the need to remove a residual bias in the z position of the *cog* of the track. This was accomplished *in situ* using an inclusive muon data set which demonstrated that the z position of the *cog* of the CDC track was biased. For the muon chambers, the z direction corresponds to the drift direction which has a maximum drift distance of 5 cm. The muon drift chambers were optically surveyed and confidence in the survey was established through analysis of muon data, ruling out any linear bias in the z position measurement. The residual bias was traced to a miscalibration of the effective signal propagation velocity of the signals in the pickup windings of the CDC delay lines.

The true and measured z position of the *cog* of the track are related linearly by

$$z_{true} = \alpha_{CDC} z_{meas} + \beta_{CDC}. \qquad (18)$$

With the muon data sample, the scale factor α_{CDC} was determined by defining a track using the *cog* of the muon track, as reconstructed in the first layer of muon spectrometer before the toroidal magnet, and the vertex z position. By comparing the expected and measured z positions the scale factor was determined to be $\alpha_{CDC} = 0.988 \pm 0.002$, where the error is the combination of a small statistical component (± 0.0003) and the following systematic components: the observed variations in scale factor for different azimuthal regions of the detector (0.001), observed variations for different polar angles of the muon tracks (0.001), muon chamber alignment (0.0003), and different methods to extract α_{CDC} (0.0004). The offset β_{CDC} is consistent with zero. In this analysis $\alpha_{CDC} = 0.988$ and $\beta_{CDC} = 0$ were used. The scale factor has been confirmed using cosmic ray muon data. The trajectory of cosmic ray muons traversing the full detector was reconstructed using the non-magnetic inner volume of the spectrometer. As before, the expected CDC track posi-

tions were compared to their measured positions and the scaling behavior of the *cog* of the CDC track was, within its uncertainty, confirmed.

To verify the consistency of the electron angle determination, $Z \to ee$ events were studied. Given the electron cluster position, their track intersections with the beamline were reconstructed from the $Z \to ee$ decay. These intersections in general do not coincide. After applying the correction to the CDC *cog*, the width of the distribution in the difference in z positions of the two intersections was tracked by varying the calorimeter electron z position. The resultant width of the distribution was at a minimum without applying any correction to the electron calorimeter position, showing the internal consistency of the procedure.

4. Measurement of $\vec{\not{E}}_T$

The total missing transverse energy in the event is calculated by summing over all calorimeter and ICD cells

$$\vec{\not{E}}_T = -\sum_i E_i \sin \theta_i \hat{u}_i = -\sum_i \vec{E}_T^i. \qquad (19)$$

Here $\hat{u}_i$ is a unit vector from the event vertex to the *cog* of the i-th calorimeter cell, E_i the energy in the i-th calorimeter cell, and θ_i is the polar angle given by the event vertex and the *cog* of the i-th calorimeter cell.

The nominal event vertex was determined using all tracks in the CDC. At the DØ straight section, the collision point was slightly off-center at $z = -7.98$ cm, having a Gaussian width of $\sigma = 26.5$ cm. The transverse momentum of the electron was calculated using the total energy and direction of the cluster in the calorimeter. Since, the electron direction, as computed above, may not intersect the nominal event vertex, a recalculation of the $\vec{\not{E}}_T$ was done by using the vertex obtained from the electron alone. For $Z \to ee$ events, the event vertex and the electron polar angles were determined using a constrained fit of the measured variables of the two electron directions. The missing transverse energy used in this analysis was based on calorimetric information alone and was not corrected for possible muons in the event.

B. Final $W \to e\nu$ and $Z \to ee$ data sample

After electron identification and calculation of the missing transverse energy, the final W boson and Z boson candidate samples were subjected to the following selection criteria.

Fiducial requirements were placed on the electrons in the W boson candidate events to select central electrons: $|i_\eta^e| \leq 12$. Here, i_η^e is an integer index for the calorimeter tower containing the most energetic cell of the electron cluster in the third EM layer. It is equal to $10 \times \eta$ for particles which originate at $z = 0$. In order to ensure no energy leakage into the uninstrumented regions within modules, electrons were restricted from the readout edges in ϕ by requiring that their impact to be within the central 80% of each module. An additional requirement was imposed that no event have a jet in which the fraction of energy in the CH section of the calorimeter exceeds 0.4. This eliminated events with spurious energy depositions from the Main Ring.

TABLE III. Event samples for W and Z bosons. Here, ''N'' and ''S'' refer to the end calorimeters on the north and the south. Note that the asymmetry in event numbers is due to the offset of the mean collision point.

		W boson event sample			
ECN		CC			ECS
1838		7234			1681
		Z boson event sample			
	ECN-ECN	ECN-CC	CC-CC	CC-ECS	ECS-ECS
Mass measurement	48	147	366	134	39
Resolution studies	46	143	344	130	35

The kinematic and fiducial requirements that defined the W boson candidate sample are

$$|i_\eta^e| \leq 12$$
$$E_T^e > 25 \ \text{GeV}$$
$$\not{E}_T > 25 \ \text{GeV}$$
$$p_T^W < 30 \ \text{GeV}/c.$$

This resulted in a sample of 7262 events. Additionally, including a transverse mass cut of $M_T < 110 \ \text{GeV}/c^2$ left 7234 candidates.

Z boson candidate events were accepted with the requirements:

$$|i_\eta^e| \leq 12 \ \text{ or } \ |i_\eta^e| \geq 15$$
$$E_T^{e1,2} > 25 \ \text{GeV}.$$

As in the W boson sample, the module boundary edge cut was made for CC electrons only. For the final Z data sample, only events with both electrons in the CC ($|i_\eta^e| \leq 12$) were used. This resulted in a sample of 395 candidate events with both electrons in the CC. A Z boson mass cut which eliminated events outside a window of $70 < m_{ee} < 110 \ \text{GeV}/c^2$ left 366 candidates. For some studies, events with one electron in the forward region ($|i_\eta^e| \geq 15$) were included. For resolution studies, $Z \to ee$ events had the additional requirement that events were not accepted when taken during the Main Ring cycle.

Table III lists the final number of events in the samples. Figure 3(a) shows the transverse mass distribution of the central W boson candidate events, before the transverse mass cut and 3(b) shows the invariant mass distribution of the central Z boson candidate events. Neither distribution is corrected for the electron energy scale determined *in situ* (see Sec. IV).

C. Data samples used in the analysis

There were five primary data samples which are used in this analysis.
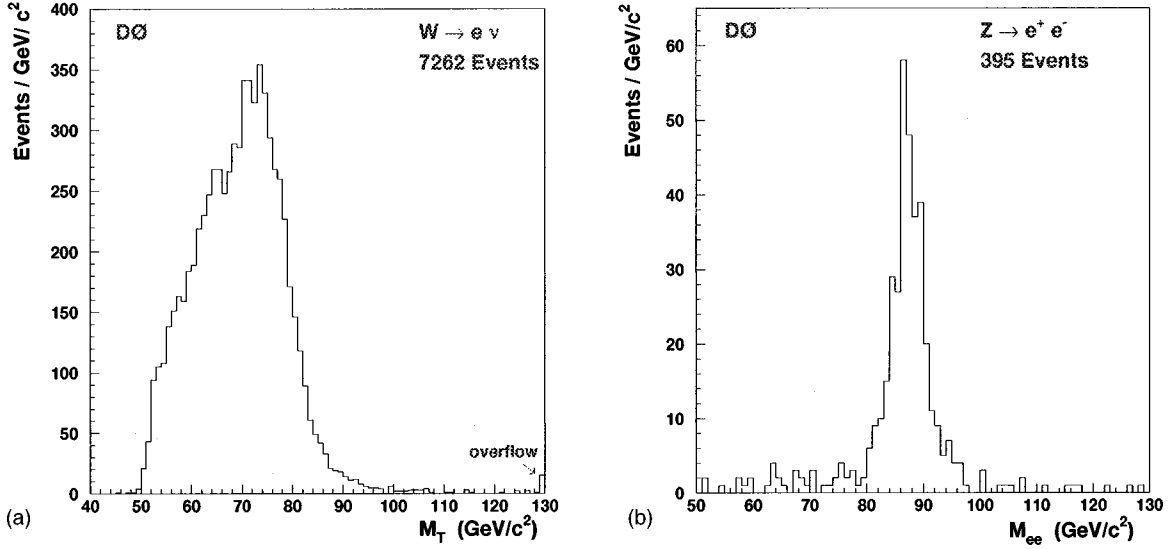
FIG. 3. (a) Transverse mass distribution of W events and (b) dielectron invariant mass distribution from Z events. Both distributions are shown before the application of fitting window cuts or energy scaling (see Sec. IV).

$W \to e\nu$ sample: A sample of 7262 $W \to e\nu$ candidates (prior to fitting and transverse mass cut) provided the main data sample used to measure the W boson mass.

$Z \to e^+e^-$ sample: A sample of 395 central $Z \to e^+e^-$ candidates (prior to the Z boson mass cut) was used along with the $W \to e\nu$ sample to measure the W boson mass. A slightly enlarged sample was used in the determination of detector response parameters.

Minimum bias sample: A sample of approximately 50,000 triggers, taken at various luminosities, was used for modeling the underlying event. (Appendix C includes a detailed discussion of how the minimum bias events were deployed in the W boson analysis.)

$J/\psi \to e^+e^-$ sample: A data set of approximately 50 observed J/ψ candidates was used in the electron energy scale determination.

$\pi^0 \to \gamma\gamma \to e^+e^-e^+e^-$ sample: A data set of approximately 2500 observed π^0 candidates was used in the electron energy scale determination.

IV. DETERMINATION OF PARAMETERS IN MONTE CARLO SIMULATION

The extraction of M_W relied on an accurate and fast Monte Carlo simulation. The details of the physics model used in the simulation will be discussed in the next section. However, many parameters such as calorimeter response, efficiencies, and resolutions, were input to the simulation and were derived from the data. The focus of this section is a detailed description of how these parameters were determined. The use of these parameters in the simulation appears in Sec. V and the systematic errors on M_W due to uncertainties inherent in these parameters is described in Sec. VII.

A. Electron energy scale

All calorimetric measurements rely on the determination of the overall energy scale using particles of known momen-

tum and/or on the reconstruction of the mass of well known particles. Both techniques have been used to calibrate the DØ calorimeter. Since the absolute energy scale of the EM calorimeter was not known to the required precision, the ratio of the measured W boson and Z boson masses and the world average Z boson mass were used to determine the W boson mass. A number of systematic effects, common to both measurements, cancel in the ratio. Most notably, as will be discussed in more detail below, the ratio was, to first order, insensitive to the absolute energy scale.

The initial calibration of the calorimeter was provided by transferring the calibration from a test beam to the collider detector, as discussed in Sec. III A [36]. An important result of these test beam measurements was the demonstration that the EM calorimeter is linear to better than 0.5% for electron energies exceeding 10 GeV. To complete the establishment of the energy scale with the desired precision, it was necessary to determine to what extent a possible offset in the energy response, as opposed to only a scale factor, was responsible for the deviation of the ratio $M_Z^{\text{DØ}}/M_Z^{\text{LEP}}$ from unity.

A strategy for establishing the final energy scale and possible offset in the response was implemented. Inherent to this program is the assumption that the measured energy E^{meas} is related to the true energy, E^{true}, by a scale α and offset δ:

$$E^{\text{meas}} = \alpha E^{\text{true}} + \delta. \qquad (20)$$

Then, for a two body decay when $\delta \ll (E_1 + E_2)$, the measured invariant mass of the decay products m^{meas} is related to the true mass m^{true} by

$$m^{\text{meas}} \approx \alpha m^{\text{true}} + \delta \times f. \qquad (21)$$

Here, f is a parameter that depends on the kinematics of the decay and is given by

$$f = \frac{(E_1^{\text{meas}} + E_2^{\text{meas}})(1 - \cos\gamma)}{m^{\text{meas}}} \qquad (22)$$

where $E^{\text{meas}}_{1,2}$ are the measured energies of the two decay products and γ the opening angle between them. When δ is small, f is nearly equal to $\partial m^{\text{meas}}/\partial \delta$. Hence, sensitivities to δ can be different, depending on f.

Consequently, the dependence of the measured ratio of the W boson to Z boson masses on α, δ can be estimated from the relation

$$\left.\frac{M_W(\alpha,\delta)}{M_Z(\alpha,\delta)}\right|_{\text{meas}} = \left.\frac{M_W}{M_Z}\right|_{\text{true}}\left[1 + \frac{\delta}{\alpha}\cdot\frac{f_W M_Z - f_Z M_W}{M_Z\cdot M_W}\right]. \tag{23}$$

Here, f_W and f_Z correspond to average values of f for the W and Z bosons, respectively. Note that the determination of M_W from this ratio is insensitive to α if $\delta=0$, and that the correction due to a non-vanishing value for δ is strongly suppressed due to the fact that the W and Z boson masses are nearly equal.

The values of α and δ were determined from the analysis of collider events containing two-body decays for which m^{true} is known from other measurements. The liquid argon calorimeter gains were measured to be stable over a period of years, varying by less than 0.2% per year. Therefore, results for the scale determined during one period of the exposure may be used during a different period. The three decays used are the $Z\to ee$ decays, measurements of $\pi^0\to\gamma\gamma\to 4e$ states, and $J/\psi\to ee$ states. These three decays probe a useful range in f. The reference mass values used as benchmarks are: $M_Z=91.1884\pm0.0022$ GeV/c^2 [19], $m_{J/\psi}=3.09688\pm0.00004$ GeV/c^2 [18], and $m_{\pi^0}=134.976\pm0.0006$ MeV/c^2 [18].

$Z\to ee$ *analysis:* The strongest constraint on the energy scale uncertainty comes from the Z boson data. The fact that electrons from Z boson decays are not monochromatic is exploited by studying the invariant mass distribution as a function of the variable f_Z. Small values of f_Z correspond to the decay of highly boosted Z bosons with, on average, higher energies. Thus an analysis of the Z boson sample directly translates into a constraint on both the energy scale and offset. This analysis was based on Z boson events with both electrons in the CC which were required to pass the same selection criteria as the final Z boson sample, except that $E_T>10$ GeV was required for both of the electrons. The data were binned in f_Z and the distribution in m^{meas}_{ee} was fit using a convolution of the Z boson Breit-Wigner resonance with a Gaussian resolution function. Using the standard Monte Carlo generator (described in the next section), sample distributions in m_{ee} were generated under different assumptions for α and δ. A χ^2 comparison was performed between the data and the Monte Carlo and the 1σ constraint on α and δ from the Z boson data, shown as the solid line in Fig. 4, was determined.

π^0 *analysis:* π^0 mesons were observed through their two photon decay and subsequent conversion to unresolved e^+e^- pairs. There is a 10% probability for each photon to convert in front of the CDC, so that when both photons convert the dE/dx can be measured in the drift chamber and a strategy for the identification of π^0 decays is possible. The
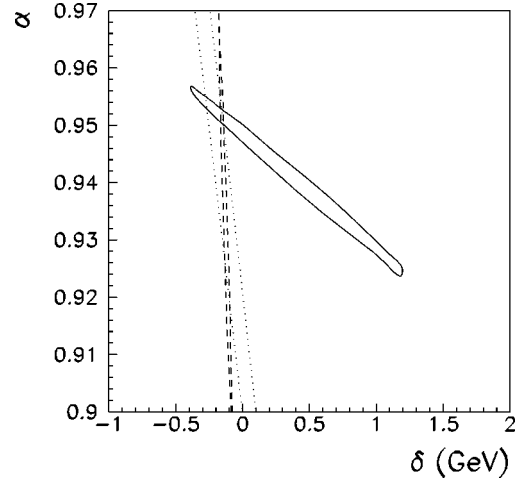
FIG. 4. Constraints on α and δ from (a) $Z\to ee$ decays (solid contour), (b) $J/\psi\to ee$ decays (dotted lines), and (c) $\pi^0\to\gamma\gamma\to 4e$ decays (dashed lines).

identification requirement was that one electromagnetic cluster be observed with two doubly ionizing tracks pointing to it. The diphoton opening angle, θ, was calculated from the center of gravity of those two tracks and the measured vertex of the event. In this way, an approximation of the mass was calculated as

$$m^{\text{meas}}_{\gamma\gamma} = (E_{\text{clus}})\sin\frac{\theta}{2}, \tag{24}$$

where E_{clus} is the cluster energy (on average, approximately 5 GeV) which is equal to the sum of the photon energies since the photons are not resolved in the calorimeter. This strategy assumes a symmetric decay. Figure 5 shows the signal and background, the latter determined from a single-conversion control sample. The invariant mass spectrum of the background-subtracted signal compares well with a Monte Carlo simulation shown as the solid line in Fig. 6. The measured mass is $m_{\pi^0}=135.4\pm10.0$ MeV/c^2. The sensitivity to the energy scale and offset is determined by varying both parameters in the Monte Carlo simulation and performing a χ^2 fit to the data. Since the response given in Eq. (20) is the response per electron, the offset in response for the π^0 is $\delta_{\pi^0}=4\delta$. This procedure maps out an allowed region in the (α,δ)-plane shown as the dashed line in Fig. 4.

J/ψ *analysis:* A sample of $J/\psi\to ee$ events was also used in the EM energy scale determination. The data were collected in a set of special runs and had an integrated luminosity of ≈ 100 nb^{-1}. The L1 trigger required two EM triggers towers above a 2.5 GeV threshold with less than 1 GeV in the corresponding hadronic towers. At L2, two EM energy clusters above 3 GeV were required and the isolation fraction was required to be $f_{\text{iso}}<0.4$. Since the major background is due to $\pi^0\to\gamma\gamma$ and $\eta\to\gamma\gamma$ decays in which one of the photons converts before it reaches the tracking chamber, the track associated with the electron cluster was required to have an energy deposition in the tracking chamber of less than 1.5 times the energy deposition of a minimum ionizing particle (MIP). In addition a cut was placed on the width of
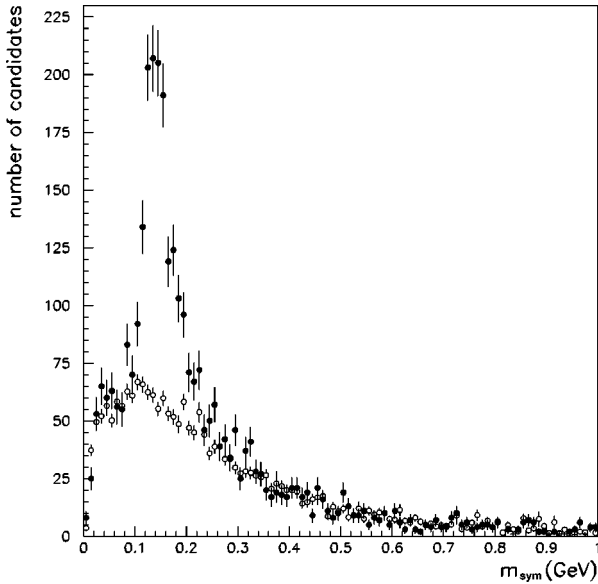
FIG. 5. The invariant mass from $\pi^0 \to \gamma\gamma \to e^+e^-e^+e^-$ decay events (points). Also shown is the background contribution (open circles).

the cluster, defined as the average weighted distance of each cell of the cluster from its center. The weights are the same as those used in the position finding algorithm. The opening angle between the two electrons was determined from the event vertex and the cluster positions in the calorimeter. Figure 7 shows a clear $J/\psi \to ee$ signal above background. The background mass distribution for the J/ψ signal was obtained independently by pairing EM energy clusters in the calorimeter in which at least one of the EM clusters had no associated track. If there was an associated track, it was required to have an energy deposition greater than 1.5 MIP. The remaining requirements imposed on the EM energy clusters were the same as in the analysis of the ee events.
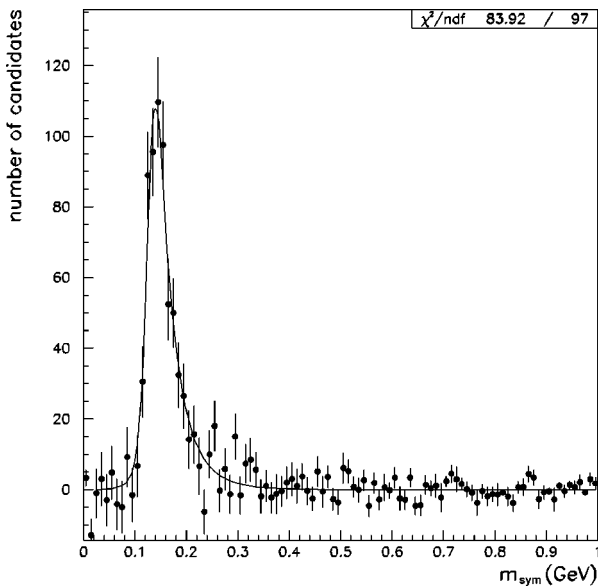
FIG. 6. Background subtracted invariant mass from the π^0 event sample (points) compared to the Monte Carlo simulation (line).
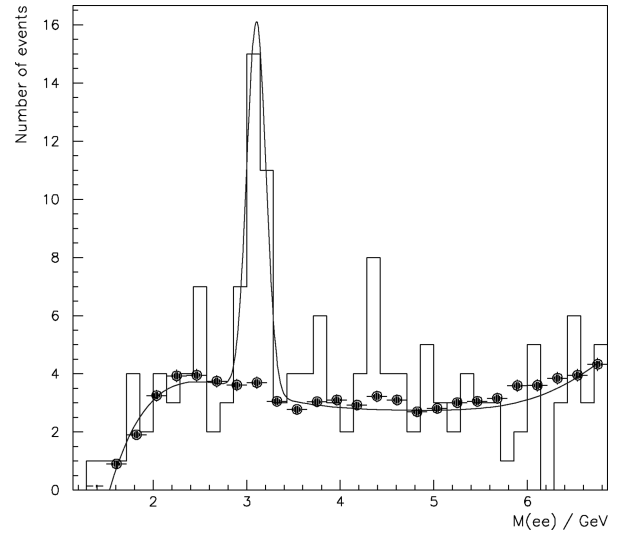
FIG. 7. Mass distribution of the observed $J/\psi \to ee$ decays (histogram) is shown above the background (points). The line is a fit to the signal plus background.

The mass value fit for these data is $m_{J/\psi} = 3.032 \pm 0.035 \pm 0.190$ GeV/c^2, where the first error is statistical and the second is systematic. The systematic uncertainty is dominated by the extreme assumption of a nonlinear response (0.170 GeV/c^2) and by the underlying event contribution (0.080 GeV/c^2).

The model used for comparison to the $m_{J/\psi}$ distribution was an ISAJET [37] based simulation for $b\bar{b}$ production and subsequent decay to J/ψ followed by a GEANT detector simulation. Since there is additional jet activity close to the electrons in J/ψ decays from b quarks, the contribution from the underlying event energy was evaluated using the simulation. Two classes of events were generated consisting of only the e^+e^- pair of the J/ψ decay and events corresponding to the full $p\bar{p}$ collision. The difference between the fully simulated and the reconstructed mass was 80 MeV/c^2. This difference was applied as a correction and an uncertainty of 100% was assigned to this correction. Figure 4 shows the constraint on α, δ from the J/ψ analysis indicated by the dotted line.

Underlying event contribution: Background energy and noise can contribute to the measurements of electron energies. The different environments for M_Z, m_{π^0}, and $m_{J/\psi}$ final states led to different corrections for each. Monte Carlo studies specialized to the scale analysis plus the understanding of instrumental effects lead to corrections for M_Z, m_{π^0}, and $m_{J/\psi}$ of 0.17 ± 0.05, 0.30 ± 0.10, and 0.08 ± 0.08 GeV/c^2, respectively. The uncertainties on these measurements form the dominant uncertainties in the determination of α and δ for the π^0 and J/ψ analyses.

Combined analysis: The data from the three samples are combined by adding the χ^2 distributions. For the combined χ^2 the minimum value is $\chi^2 = 53.8$ for 58 degrees of freedom, with a best fit of $\delta = -0.158 \pm 0.016$ GeV and $\alpha = 0.9514 \pm 0.0018$. This is consistent with the result obtained from the Z boson data only, but with substantially reduced errors. Figure 8 shows an enlargement of the region where the contours from the three data samples overlap. The
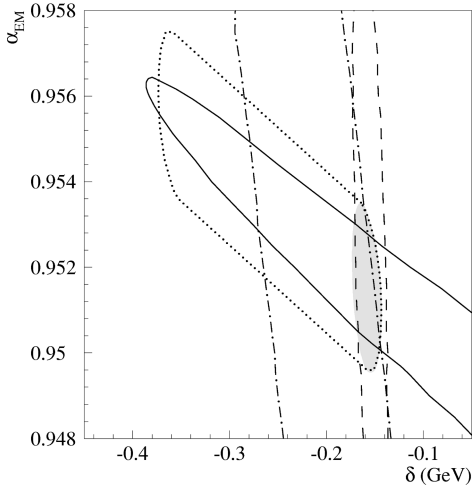
FIG. 8. Expanded view of Fig. 4 showing α versus δ with the combined best fit (shaded region). The expanded lobe (dotted contour) to lower values of δ is due to uncertainties in the low energy non-linear response of the calorimeter. The contributions are from: $Z \rightarrow ee$ decays (solid contour), $J/\psi \rightarrow ee$ decays (dashed-dotted lines), and $\pi^0 \rightarrow \gamma\gamma \rightarrow e^+e^-e^+e^-$ decays (dashed lines).

shaded area is the contour obtained from the combined analysis for a unit change in the combined χ^2.

The main contributions to the systematic uncertainties were the underlying event correction and possible non-linearities in the energy response. Varying the underlying event by the errors quoted above changes the value of δ for which the combined χ^2 is minimized by ± 2 MeV when varying the underlying event contribution to the J/ψ and by ± 30 MeV when varying the contribution to the π^0. In addition the calorimeter π^0 response was varied taking $\delta_{\pi^0} = 3\delta$, rather than 4δ as discussed above. This decreased the best value for δ by 52 MeV. The dominant uncertainty comes from a possible nonlinearity of the calorimeter and has been addressed by studying test beam data. The test beam data permitted a small nonlinear response of the EM calorimeter and was parametrized by including a quadratic term in the energy response of Eq. (20), which was constrained by the test beam data to not exceed 1 part in 10^4. Allowing for a nonlinear response characterized by such a quadratic term and repeating the above analyses results in an allowed region in α, δ indicated by the dotted line in Fig. 8. The result is to decrease δ by 200 MeV. The energy scale parameters and their uncertainties are thus

$$\delta = -0.158 \pm 0.016^{+0.03}_{-0.21} \text{ GeV}, \qquad (25)$$

$$\alpha = 0.9514 \pm 0.0018^{+0.0061}_{-0.0017} \qquad (26)$$

where the first error is statistical and the second systematic. The effect of a possible quadratic response term was included as the asymmetric contribution to the overall uncertainty shown on δ.

The result described in this section constitutes the calibration of the central EM calorimeter *after* the initial calibration based on a transfer of the calibration from the test beam

given by Eq. (15). In practice, inserting the offset as defined in Eq. (15) into Eq. (20) leads to

$$E^{\text{meas}} = \delta^{TB} + \delta + \alpha E^{\text{true}} \qquad (27)$$

demonstrating that the *in situ* determination of δ amounts to a redetermination of δ^{TB}. Combining Eq. (27) with Eq. (15) leads to

$$E^{\text{true}} = -\frac{\delta}{\alpha} + \frac{C}{\alpha} \sum_i \beta_i S_i. \qquad (28)$$

Using the redetermined values of α and δ, an overall offset of $-\delta/\alpha = 158/0.9514 = 166$ MeV was observed consistent with the average energy loss by electrons in the material before the calorimeter which was predicted by GEANT Monte Carlo simulation studies.
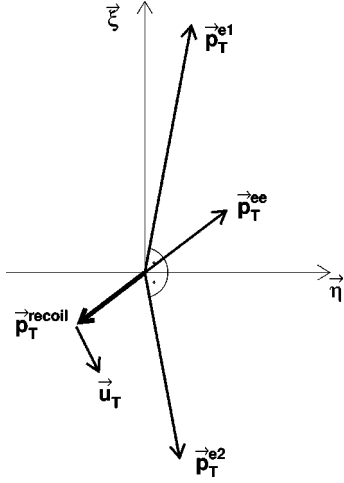
B. Hadronic energy scale

The scale of the measured recoil momentum differs from the electron energy scale because the recoil measurement also includes energy from hadronic showers and suffers from the loss of energy in uninstrumented regions of the calorimeter. The response of the hadronic calorimeter relative to the response of the electromagnetic calorimeter was determined from $Z \rightarrow ee$ events. In $Z \rightarrow ee$ events the transverse momentum of the Z boson p_T^Z can be obtained from either the measurement of the transverse momenta of the two electrons $\vec{p}_T^{ee}$ or from the recoil activity in the event $-\vec{p}_T^{rec}$. The latter was the way in which p_T^W was measured. To minimize the effects of the energy resolution in the determination of the hadronic energy scale relative to the electromagnetic energy scale, the momentum imbalance was measured with respect to the (η, ξ)-coordinate system [12]. The η axis is defined as the bisector of the two electron transverse directions. In the plane of the electrons, the axis orthogonal to the η axis is the ξ axis (see Fig. 9). The η imbalance is then defined as

$$\eta_{\text{imb}} = \vec{p}_T^{ee} \cdot \hat{\eta} + \vec{p}_T^{rec} \cdot \hat{\eta} \qquad (29)$$

with $\hat{\eta}$ a unit vector along the η axis. If the electromagnetic and hadronic responses are equal, η_{imb} is zero. Since the positive η axis is always in the direction of $\vec{p}_T^{ee}$, any systematic bias in the measurement of $\vec{p}_T^{rec}$ will manifest itself as a bias in η_{imb}. If the difference is due only to a scale, then the relationship between the two quantities can be characterized by a proportionality constant κ.

The determination of the hadronic energy scale factor requires selection of $Z \rightarrow ee$ events with the same event topology as $W \rightarrow e\nu$ events. $Z \rightarrow ee$ events were selected with at least one electron in the central calorimeter. An additional cut to eliminate events which occur during the Main Ring cycle was imposed to ensure that no spurious calorimetric depositions affecting the measurement of the hadronic recoil were present. As a consistency check, Z boson events with both electrons in the central calorimeter have been used and a consistent result for the hadronic energy scale was ob-

FIG. 9. Definition of the η-ξ coordinate system for Z events.

FIG. 11. For $Z \rightarrow ee$ events (points) with the same event topology as W events, the average value of $\vec{p}_T^{rec} \cdot \hat{\eta}$ is shown versus $\vec{p}_T^{ee} \cdot \hat{\eta}$. The line shown is obtained from a linear least-squares fit to the data.

tained. Three related determinations of the hadronic energy response relative to the electromagnetic response have been carried out:

(1) The primary method of obtaining the calorimeter response used was the measurement of the η imbalance as function of $|\vec{p}_T^{ee} \cdot \hat{\eta}|$, as shown in Fig. 10(a). A least squares fit yields $|\vec{p}_T^{rec} \cdot \hat{\eta}| = \kappa |\vec{p}_T^{ee} \cdot \hat{\eta}|$, with $\kappa = 0.83 \pm 0.03$. The offset in response, obtained from the intercept of the fit with the ordinate in Fig. 10(a), was measured to be -0.17 ± 0.24 GeV. This result is consistent with zero. Figure 10(b) shows the η imbalance for $\kappa = 0.83$. The distribution is well described by a Gaussian distribution, centered at zero, with a width of 4.2 GeV.

(2) A second, very similar approach to fixing the scale κ of the recoil system with respect to the dielectron system was the measurement of $|\vec{p}_T^{rec} \cdot \hat{\eta}|$ as function of $|\vec{p}_T^{ee} \cdot \hat{\eta}|$, as shown in Fig. 11. The linear dependence shows that, over the

p_T range of interest to the W boson mass measurement, the hadronic recoil is related to the electromagnetic energy by a simple scale factor. The scale κ was determined by a least squares fit to the data, where the errors on $\vec{p}_T^{rec} \cdot \hat{\eta}$ and $\vec{p}_T^{ee} \cdot \hat{\eta}$ have been determined using the known detector resolutions. This method gives $\kappa = 0.84 \pm 0.03$. The offset in response is 0.06 ± 0.25 GeV, consistent with zero. It should be noted that the contribution from the underlying event $\vec{u}_T$ does not affect the determination of κ since it is distributed randomly with respect to the $\hat{\eta}$ direction. The component of underlying event which is under the electron is a negligible perturbation on the vector direction of $\vec{u}_T$

(a)

(b)
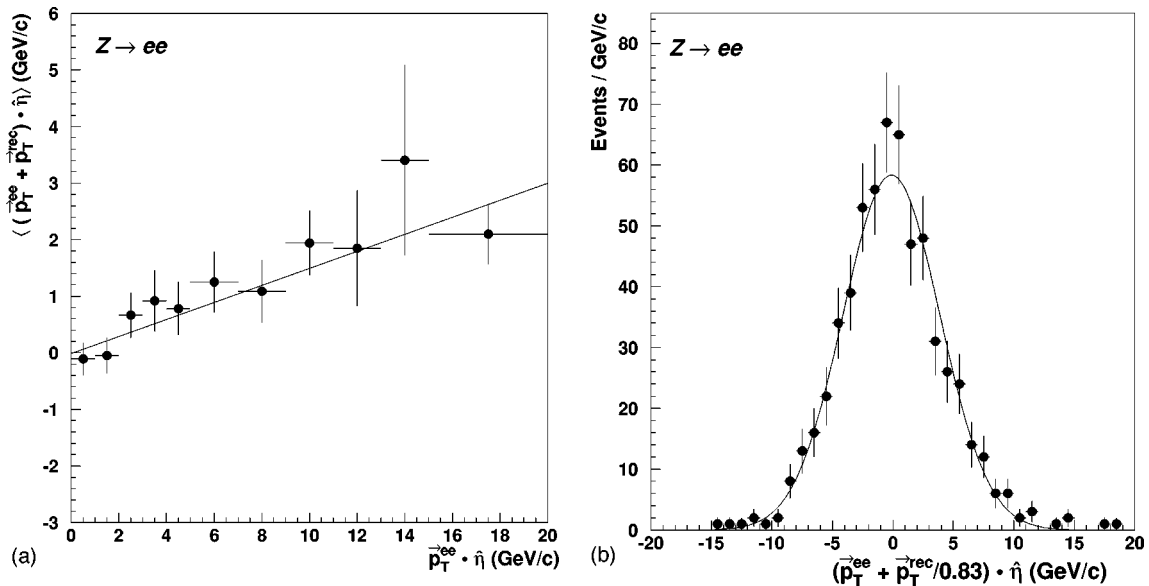
FIG. 10. For $Z \rightarrow ee$ events (points) (a) the average η imbalance versus $\vec{p}_T^{ee} \cdot \hat{\eta}$ is shown along with the line obtained from a linear least-squared fit to the data and (b) the η imbalance with a hadronic energy scale factor $\kappa = 0.83$ applied is shown with a Gaussian fit (curve).
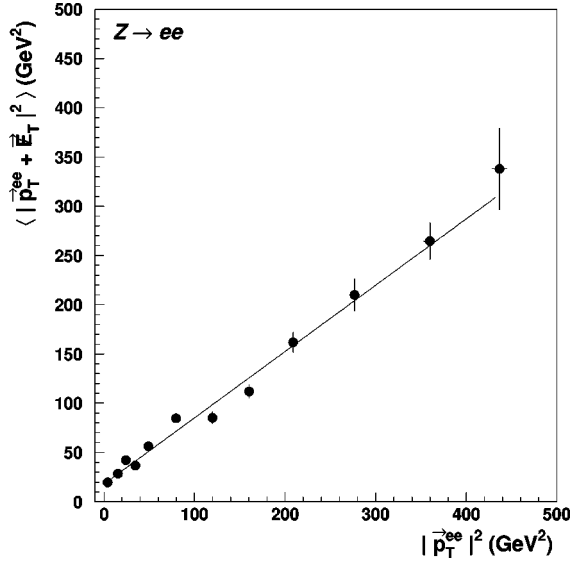
FIG. 12. Distribution of the average $|(\vec{p}_T^{\,e_1} + \vec{p}_T^{\,e_2} + \vec{E}_T)|^2$ versus $|\vec{p}_T^{\,ee}|^2$ for $Z \to ee$ events. The line shown is obtained from a linear least-squares fit to the data.

(3) The hadronic energy scale κ was also determined using a third method which yielded both the hadronic energy scale and the magnitude of the underlying event vector. The transverse momentum balance in $Z \to ee$ events is given by

$$\vec{p}_T^{\,e_1} + \vec{p}_T^{\,e_2} + \vec{E}_T = -\vec{p}_T^{\,rec} - \vec{u}_T. \qquad (30)$$

Squaring both sides, one finds for the average

$$|\vec{p}_T^{\,e_1} + \vec{p}_T^{\,e_2} + \vec{E}_T|^2 = |\vec{p}_T^{\,rec} + \vec{u}_T|^2 = \kappa^2 |\vec{p}_T^{\,ee}|^2 + |\vec{u}_T|^2 \quad (31)$$

assuming again that $|\vec{p}_T^{\,rec}| = \kappa |\vec{p}_T^{\,ee}|$. The cross term on the right-hand side averages to zero since the underlying event vector is randomly distributed with respect to the Z boson recoil system. Figure 12 shows the distribution of $|\vec{p}_T^{\,e_1} + \vec{p}_T^{\,e_2} + \vec{E}_T|^2$ versus $|\vec{p}_T^{\,ee}|^2$ for $Z \to ee$ events. Again, the data demonstrate that there is a linear relation between the electromagnetic and hadronic energy scales. The straight line is a fit to the data and yields $\kappa = 0.83 \pm 0.03$. This result is consistent with the value determined using the other two methods. The intercept of the straight line fit yields the magnitude of the underlying event vector $|\vec{u}_T|$ is 4.3 ± 0.3 GeV.

Because there was no indication of a non-linear response of the hadronic calorimeter with respect to the electromagnetic calorimeter, nor a sign of a measurable offset, the energy scale for the hadronic recoil was taken to be strictly proportional to the electromagnetic scale with a scale of $\kappa = 0.83 \pm 0.04$, the uncertainty of which was derived from the spread in the results among the three different methods. No offset of the hadronic energy scale was included in the Monte Carlo model. The effect of a possible non-linearity of the hadronic response was included when evaluating the systematic uncertainty on the W boson mass. The only use of the EC calorimeter in this analysis was in the determination of the missing transverse energy. The hadronic energy scale

was determined from the CC-CC (both electrons in the CC calorimeter) and CC-EC (one electron in each calorimeter) $Z \to ee$ events. The hadronic response gave the same numerical result as that using the CC-derived scale alone within errors which are negligible for this measurement.

C. Resolutions

1. Electron energy resolution

The electron energy resolution was parametrized according to the relation

$$\frac{\sigma_e}{E} = \sqrt{C^2 + \left(\frac{S}{\sqrt{E_T}}\right)^2 + \left(\frac{N}{E}\right)^2} \qquad (32)$$

where C, S, and N are the coefficients of the constant, sampling, and noise terms, respectively. The values of the sampling and noise terms were those as derived from test beam data. The test beam noise term was confirmed to agree with the width of the pedestal distributions in the collider environment. Smearing in E_T rather than in E is used in the sampling term because the resolution should become poorer with increasing thickness of the absorber plates at large angles. Replacing the usual E with E_T compensates for this and allows the coefficient S to remain constant over all of the central calorimeter. This observation was confirmed by test beam data [26,31]. The central values utilized in this analysis were obtained from the test beam for the central calorimeter and are $C = 0.015$, $S = 0.13\sqrt{\text{GeV}}$, and $N = 0.4$ GeV. For the EC, $S = 0.16\sqrt{\text{GeV}}$.

The value for the constant term was determined *in situ* by fitting the electron energy resolution to the observed width of the dielectron invariant mass distribution of the $Z \to ee$ events, fixing the width of the Z boson to its measured value of 2.490 ± 0.007 GeV [19]. There was little sensitivity for small values of the constant term, since for relevant values of E_T the energy resolution is dominated by the sampling term. A constant term of $C = 0.015^{+0.005}_{-0.015}$ was obtained, where the error is statistical only. The uncertainty on the shape of the background (discussed below) increased the upper limit on the error to $+0.6\%$.

2. Electron angular resolution

The polar angle of the electron was determined using the z position of the electromagnetic energy cluster in the calorimeter and the z position of the center of gravity of the CDC track. The angular resolution used in the Monte Carlo simulation was therefore determined by the resolutions on these two quantities.

The resolution of the calorimeter hit position was determined using electrons from $W \to e\nu$ decays processed through a detailed GEANT Monte Carlo. Because of the read-out geometry of the detector, it depended both on the angle of incidence of the electron and its cluster z position, z_{clus}. It was parametrized as a Gaussian distribution having a width
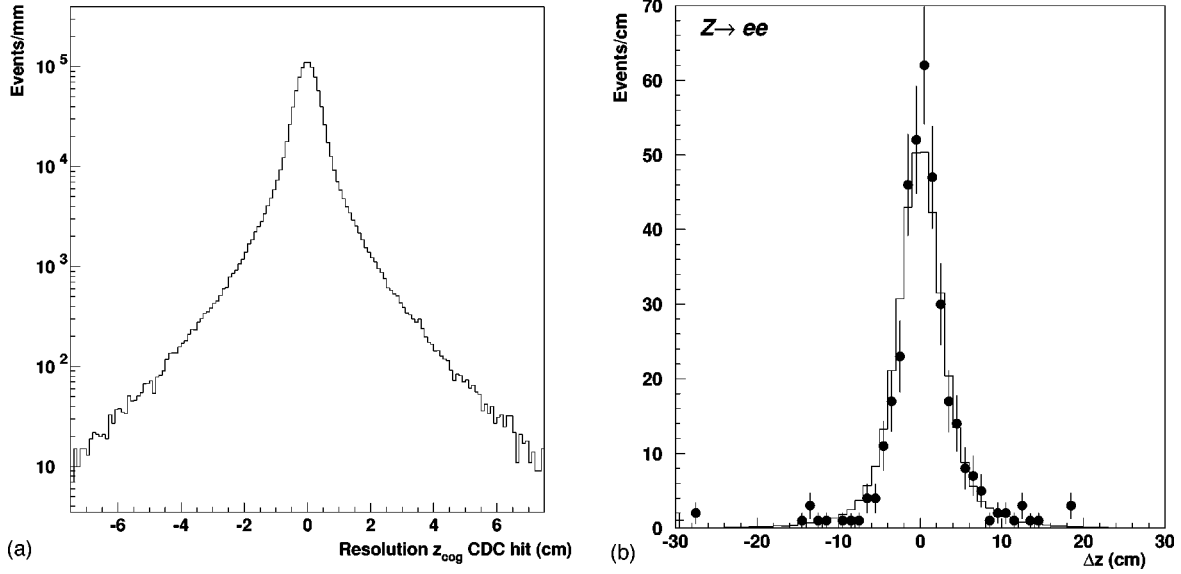
FIG. 13. (a) The modeled resolution of the z position of the center of gravity of CDC tracks and (b) the distribution in the difference of the intersections of the z axis of the two electron tracks from Z decays (points) compared with the distribution from the Monte Carlo simulation.

$$\sigma(z_{\text{clus}}) = (p_1 + p_2 \times |\varpi|) + (p_3 + p_4 \times |\varpi|)|z_{clus}| \quad (33)$$

where $p_1 = 0.33183$ cm, $p_2 = 0.52281 \times 10^{-2}$ cm/degree, $p_3 = 0.41968 \times 10^{-3}$, and $p_4 = 0.75496 \times 10^{-4}$ cm/degree. The angle ϖ is the polar angle of the electron (in degrees) as measured with respect to the $\eta = 0$ axis of the detector.

The resolution of the z position of the center of gravity of the track was measured from $Z \to ee$ events using the intersections of the two electron tracks with the beamline. The distribution of the difference in z position of the two intersections shows non-Gaussian tails which were represented in the Monte Carlo program. The simulation generates a resolution on z_{cog}^{CDC} as shown in Fig. 13(a). The model was verified by comparing a Monte Carlo generated distribution of the difference in the intersections of the two electrons from Z decays with that obtained from the data, and is shown in Fig. 13(b).

In the data analysis, the azimuthal angle of the electron was given by the φ angle as measured by the CDC. The resolution was taken to be the CDC φ resolution and is modeled as a Gaussian distribution with width $\sigma(\varphi) = 0.005$ radians. For some $Z \to ee$ studies electrons in the end calorimeters were also used. The angular resolutions of these electrons were modeled in the Monte Carlo program as Gaussian distributions with resolution $\sigma(\varphi) = 0.015$ radians and $\sigma(\theta) = 0.015$ radians.

3. Hadron energy resolution

The recoil against the vector boson was modeled by assuming it to be a single jet. The transverse momentum of the vector boson was smeared using the hadronic energy resolution determined both in the test beam and from analysis of jets *in situ*. It was parametrized as

$$\frac{\sigma_{had}}{E_T} = \sqrt{C^2 + \left(\frac{S}{\sqrt{E_T}}\right)^2 + \left(\frac{N}{E}\right)^2} \quad (34)$$

with resolution parameters $C = 0.04$, $S = 0.80\sqrt{\text{GeV}}$ and $N = 1.5$ GeV [26].

D. Efficiencies

There were two main inefficiencies which affected this measurement: those related to the hardware trigger, and those related to electron identification criteria. Both effects can potentially bias the measurement as these particular inefficiencies depend on the kinematics. These efficiencies are determined from data as discussed below.

1. Trigger efficiencies

The main data sample was recorded with an on-line filter, which required an electromagnetic cluster with $E_T^e > 20$ GeV and $\not{E}_T > 20$ GeV. The trigger efficiency as function of the offline electron and missing transverse energies was determined using a single electron trigger as well as triggers with lower requirements. After 27% of the running was completed, the missing transverse energy calculation in the L2 trigger was changed to use the event vertex as measured by the L0 system, rather than the nominal $z = 0$ value. Therefore, two different threshold curves have been used in this data analysis. Both the E_T^e and $\not{E}_T$ requirements in the trigger were more than 99% efficient for transverse energies greater than 30 GeV.

2. Electron identification efficiency

The recoil of the W boson may affect the electron identification, especially if the recoil system is close to the electron. A measure of the event selection biases can be obtained
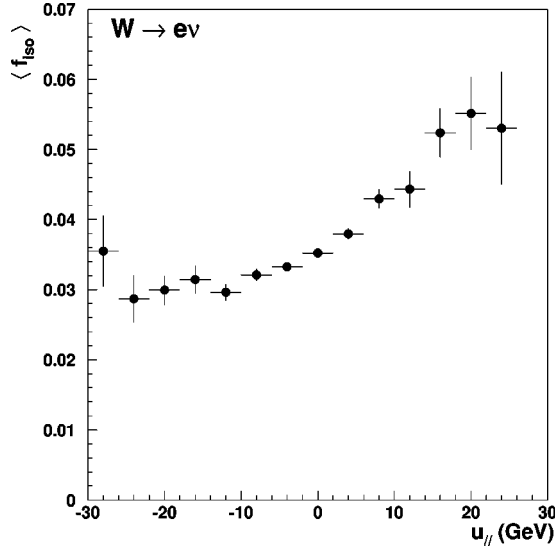
FIG. 14. Average value of the isolation versus $u_\parallel$ for electrons from $W \to e\nu$ decays.

by studying identification efficiencies as a function of the quantity $u_\parallel$, which is the projection of the momentum recoiling against the W boson along the electron [14]:

$$u_\parallel \equiv \vec{p}_T^{rec} \cdot \hat{e}, \qquad (35)$$

where $\hat{e}$ is a unit vector in the electron direction. A bias in the electron identification as function of $u_\parallel$ would distort the lepton p_T spectra. For example, an inefficiency of the electron identification at high positive values of $u_\parallel$, when the recoil is close to the electron, would result in a softer p_T^ν spectrum.

The event selection efficiency as a function of $u_\parallel$ was determined by studying the behavior of the energy isolation fraction, f_{iso}, of the electrons in the signal sample. Figure 14 shows the average isolation versus $u_\parallel$ for the electrons in the W boson data sample. For negative values of $u_\parallel$, when the recoil jet is opposite the electron, the isolation is constant. This indicates that for these event topologies the recoil system did not affect the electron, as expected. For positive values of $u_\parallel$ the isolation increases linearly with $u_\parallel$, indicating that there was a ''halo'' of constant energy flow surrounding the direction of the recoil jet. The electron identification efficiency was determined by modeling the distribution of the isolation variable for different ranges of $u_\parallel$ as shown in Fig. 15. The curves are the result of a fit to the data using a five parameter functional form. To determine the electron identification efficiency as a function of $u_\parallel$, fits to the isolation distribution were integrated over f_{iso}. The fraction of events with $f_{iso} > 0.15$ constituted a determination of the inefficiency due to the recoil jet spoiling the electron signature. The efficiency as function of $u_\parallel$ is shown in Fig. 16 where the curve is a parametrized fit.

The dominant systematic uncertainty stems from the shape of the isolation distribution for values of $f_{iso} > 0.15$, above the trigger restriction. This was addressed by studying W boson events in which the electron cluster was rotated in
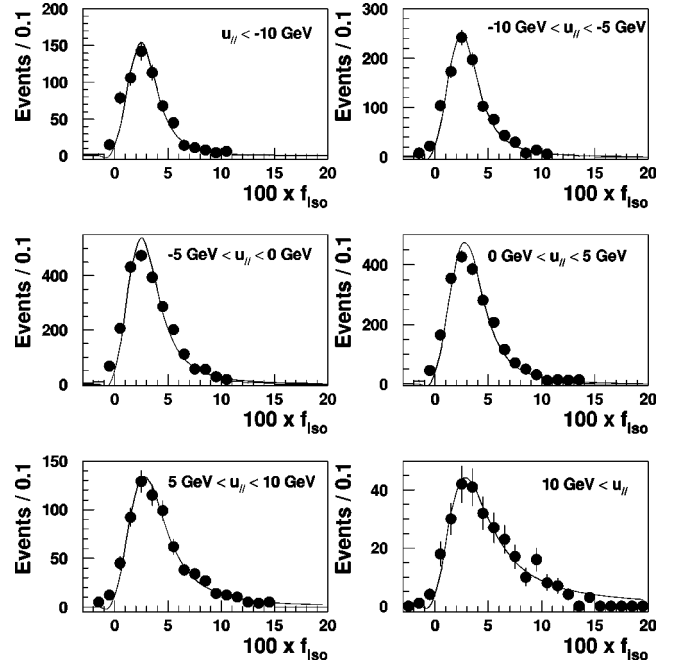
FIG. 15. Distribution of the isolation value, f_{iso}, for electrons from $W \to e\nu$ decays for different $u_\parallel$ ranges (points). The curves are fits to the data.

azimuth, re-analyzed, and the isolation re-evaluated. The tail of the isolation distribution obtained in this way was well described by the fitting function. In addition, when fitting for the isolation distribution of the rotated sample, a maximum variation in the efficiency of 1.5% was noted. To be conservative, the efficiencies were shifted coherently by
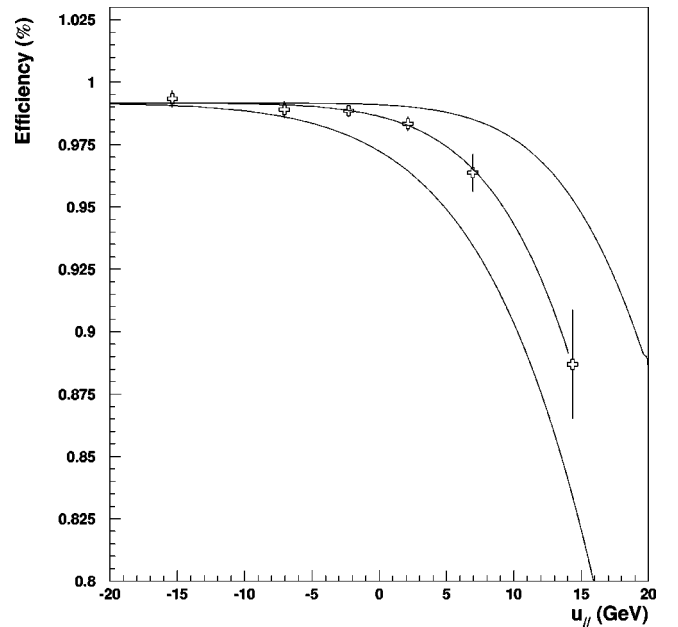
FIG. 16. Electron identification efficiency as a function of $u_\parallel$ (open crosses) from data. The central curve is a fit to the data. The outer curves show the allowed ranges for determining the systematic errors.

two standard deviations of their total uncertainties and refit. The band in Fig. 16 shows the resulting uncertainty on the efficiency.

E. Backgrounds

There was a dual approach to the treatment of backgrounds in this analysis. The process $W \to \tau \nu \to e \nu \nu \nu$ is indistinguishable from $W \to e \nu$ and was therefore explicitly included in the Monte Carlo event generation. These decays were generated with a 17.9% branching fraction for the decay $\tau \to e \nu \nu$, where the τ polarization was taken into account. Other backgrounds are characterized by data and were added to the final distributions of the fitted variables. The determination of these background contributions is discussed in this section.

1. Backgrounds to $W \to e \nu$ events

The dominant source of background to $W \to e \nu$ production was standard QCD multi-jet production, where one of the jets was misidentified as an electron and there was substantial $\not{E}_T$ from jet energy fluctuations or non-uniform energy response. This background has been estimated using data from an inclusive electron trigger that did not impose an isolation requirement at the trigger level. The background sample is selected by requiring the same kinematic and fiducial cuts as in the W boson event sample but imposing anti-electron identification cuts on the EM energy cluster. These anti-electron selections are the combination of

$$f_{\text{iso}} > 0.20$$
$$\chi^2 > 250$$
$$\sigma_{\text{trk}} > 10.$$

For multi-jet background events, it was assumed that the shape of the $\not{E}_T$ spectrum at low $\not{E}_T$ was the same independent of the electron quality cuts. The distribution in $\not{E}_T$ of the background sample was then normalized to the signal sample in the region $0 < \not{E}_T < 15$ GeV. The signal sample was selected from the same trigger by imposing the standard W boson selection criteria. The ratio of the number of events with $\not{E}_T > 25$ GeV for the signal and normalized background distributions was then taken as the amount of background in the sample. There was a 0.3% variation in the amount of background due to how the sample is normalized and how the background sample was selected.

As a consistency check, the above procedure was repeated with data taken with an inclusive electron trigger that required the EM cluster to be isolated at the trigger level. The signal sample was again taken as the events that pass the W boson event selection cuts. The background sample consisted of those events which pass the $\chi^2 > 250$ and $\sigma_{\text{trk}} > 10$ cuts. Since there was an isolation requirement in the trigger, the background sample does not have the anti-isolation cut applied as before. The two methods yielded results that are consistent within two standard deviations. The overall background fraction was taken to be $(1.6 \pm 0.8)\%$. This is an average of the two analyses which assigns a somewhat larger weight to the first method. The uncertainty assigned is about
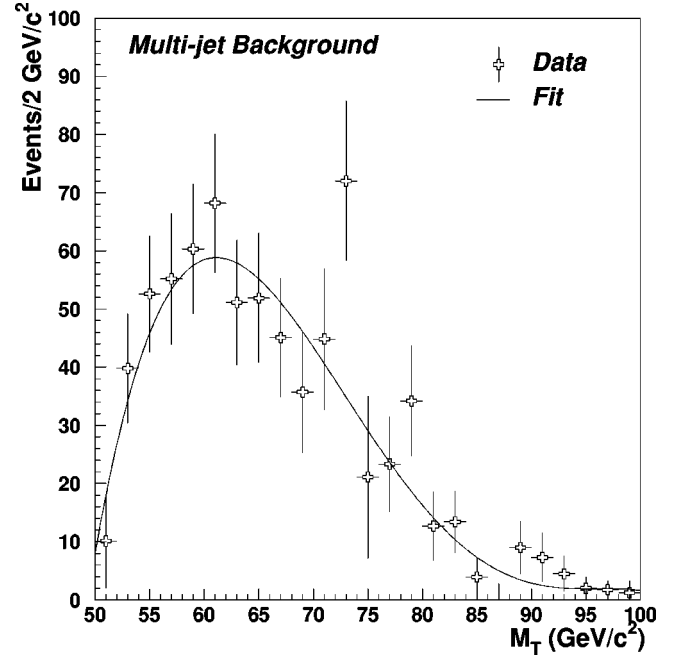
FIG. 17. Transverse mass spectrum of the multi-jet background obtained from the data (open crosses). The solid line is a fourth-order polynomial fit.

twice the error computed for this average; essentially, it encompasses the central values of both measurements.

Since very few background events survived the kinematic cuts, this method yielded only the overall background contribution leaving the shape of the background as a function of the transverse mass largely undetermined. Employing the capability of the TRD to distinguish electrons, converted photons, and pions a likelihood function was constructed employing the energy deposition in the TRD, the track dE/dx in the CDC, and the track cluster match. Using an anti-electron criterion based on this likelihood, slightly more background events survived the kinematic and acceptance cuts, allowing a determination of the dependence of the background as function of the relevant quantities. The data points in Fig. 17 show the calculated transverse mass distribution of the background obtained this way. The line is a fourth order polynomial fit. The shape of the background in lepton transverse momentum can be described by an exponentially falling spectrum with slope -0.086 ± 0.059 GeV^{-1} and -0.129 ± 0.055 GeV^{-1} for the E_T^e and $\not{E}_T$ spectra, respectively.

The other background that has been considered is the process $Z \to ee$, where one electron escapes detection and is not measured (denoted by $Z \to e \not{e}$) giving rise to a transverse momentum imbalance. This background has been estimated using ISAJET [37]. To appropriately model the underlying event in the ISAJET simulation, one minimum bias event was vectorially added to the $\not{E}_T$ for the Monte Carlo data. The overall background contribution has been estimated to be $(0.43 \pm 0.05)\%$. The M_T, p_T^e and $\not{E}_T$ spectra for this source are shown in Fig. 18. The $\not{E}_T$ spectrum does not show a Jacobian edge because the detector is hermetic and the energy of the unidentified electron is typically well measured.
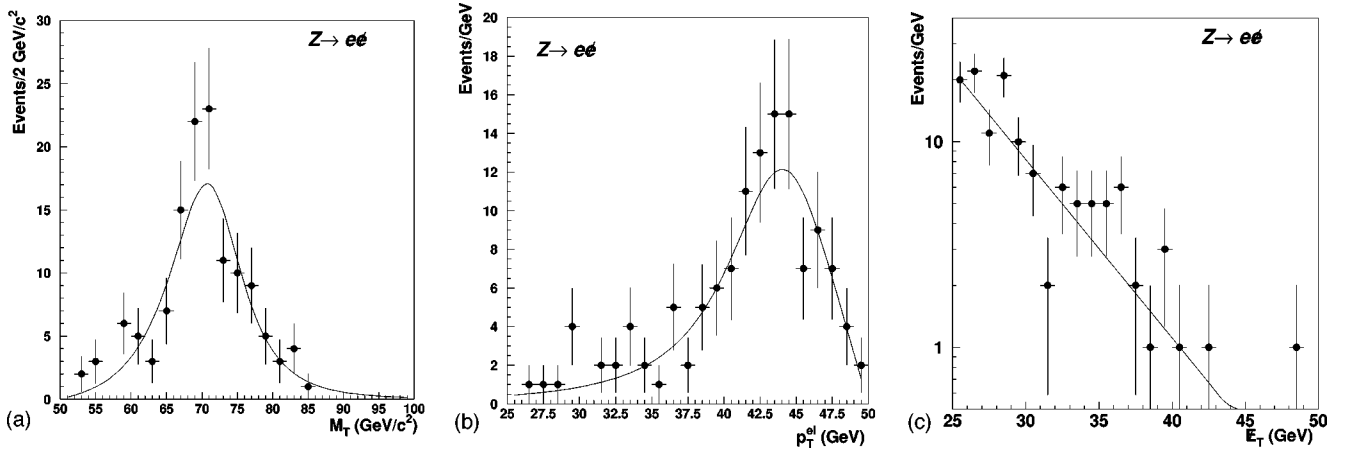
FIG. 18. Spectra in (a) M_T, (b) p_T^e and (c) $\rlap{E}{/}_T$ for the Z boson background in the W boson sample. The lines are fits to the data.

The solid lines for the M_T and p_T^e spectra are from a polynomial fit. The $\rlap{E}{/}_T$ spectrum was parametrized using an exponentially falling spectrum with slope -0.20 ± 0.03 GeV^{-1}. The average $u_{\parallel}$ for this background is -12.5 ± 0.6 GeV.

Figure 19 shows the distribution in transverse mass of the dominant background sources to the W boson event sample. The background has been normalized to the expected number of background events in the data sample.

2. Backgrounds to $Z\to ee$ events

The primary background to $Z\to ee$ events came from multi-jet production, with the jets fragmenting into a leading π^0. Since the mass is determined from the resonant cross section only, a correction also must be made for Drell-Yan and $Z\gamma^*$ interference processes. These backgrounds were determined as a function of invariant mass and were included at the fitting stage.

The total background contribution was evaluated by fitting the m_{ee} spectrum to a relativistic Breit-Wigner convoluted with a Gaussian resolution function plus a background falling exponentially in m_{ee}. For the mass range of interest, there is no distinction between a linear or exponential model of the background. This method yielded a total QCD and Drell-Yan background under the Z^0 peak of 7.4%, with a

slope of -0.0447 ± 0.018 (GeV/c^2)$^{-1}$ for an invariant mass window of 70 to 110 GeV/c^2.

The Drell-Yan and $Z\gamma^*$ contribution to the total Z boson production cross section was determined using an ISAJET simulation. In the mass range $70<m_{ee}<110$ GeV/c^2 the Drell-Yan and $Z\gamma^*$ interference terms contributed 3% to the total cross section. The background has an exponentially falling spectrum with slope -0.03 (GeV/c^2)$^{-1}$. The contribution to the background from multi-jet sources is thus 4.4%. Both the overall background contribution and its shape are in good agreement with the background determination for the cross section analysis [38].

V. MONTE CARLO SIMULATION

A. Introduction

The W boson and Z boson masses were extracted by comparing measured distributions with those generated by a Monte Carlo simulation. To determine the W boson mass the relevant distributions are those in transverse mass plus the electron and neutrino transverse momenta. For determining the mass of Z bosons the relevant distribution is in the di-electron invariant mass. The simulation was accomplished with a generator which produced all of the basic processes, incorporated the main features of the D∅ detector, and was capable of generating tens of millions of simulated events in a few hours. This section describes the physics and detector simulation. A comparison between the Monte Carlo simulation and the data is presented at the end. Table IV lists the parameters used in the Monte Carlo.

B. W and Z boson production and decay

The simulation of W and Z bosons relied on the choice of a model for the physics processes involved. This physics was divided into three parts: (i) the production model for W and Z bosons; (ii) the decay of the vector bosons and (iii) backgrounds. For the W boson the basic processes generated were $W\to e\nu$, $W\to \tau\nu\to e\nu\nu\nu$ and $W\to \gamma e\nu$; for the Z boson they were $Z\to ee$ and $Z\to\gamma ee$. As discussed in the previous sec-
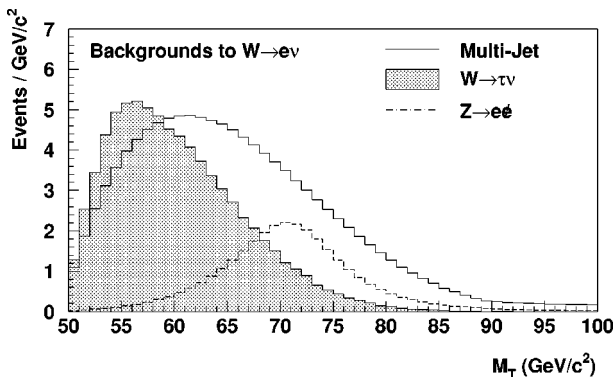
FIG. 19. Normalized distributions in transverse mass of the dominant background contributions to the W boson event sample.

TABLE IV. Parameters used in the fast Monte Carlos.

Descriptor	Nominal value
EM energy resolution, sampling (CC)	$S = 13.0\%$
EM energy resolution, constant (CC)	$C = 1.5\%$
EM energy resolution, noise (CC)	$N = 0.4$ GeV
HAD energy resolution, sampling (CC)	$S = 80.0\%$
HAD energy resolution, constant (CC)	$C = 4.0\%$
HAD energy resolution, noise (CC)	$N = 1.5$ GeV
HAD energy scale	$\kappa = 0.83$
Electron underlying event	$E_{UE}^{el} = 207$ MeV
W width	$\Gamma_W = 2.1$ GeV
Z width	$\Gamma_Z = 2.5$ GeV
# minimum bias events	1.0
Minimum E_γ	$E_\gamma^{\min} = 50$ MeV
$\Delta R(e\gamma)$	$\Delta R(e\gamma) = 0.3$
Calorimeter position resolution	$\sigma(z) \approx 0.7$ cm
CDC z_{cog} resolution	rms $z_{cog} = 2.0$ cm
φ resolution	$\sigma(\varphi) = 0.005$ rad

tion, all backgrounds, except for the $W \to \tau\nu$ decay, were not a part of the W or Z simulation and were dealt with separately.

1. Production of W and Z bosons

The triple differential cross section for vector boson production was assumed to factorize as

$$\frac{d^3\sigma}{dp_T dy dm} = C \frac{d\sigma}{dm} \times \frac{d^2\sigma}{dp_T dy}. \tag{36}$$

Here, C denotes the appropriate constants, y is the rapidity of the vector boson, and the products on the right hand side refer to shapes rather than absolutely normalized quantities. The double differential cross section was generated on a grid of p_T and y points over the region $-3.2 < y < 3.2$ and $0 < p_T < 50$ GeV/c, in steps of 0.2 in y and 0.5 GeV/c in p_T. Two choices of the production model, both based on the fully resummed theory of Collins and Soper [39], were considered. The double differential spectrum as given by Arnold and Kauffman [40] (AK) uses a next-to-leading order calculation for the high p_T region [41] with a prescription to match the low and high p_T regions. They used fits to Drell-Yan data [42] which have since been updated. The double differential cross section by Ladinsky and Yuan [43] (LY) employs a different parametrization for the non-perturbative functions describing the p_T spectrum based on a fit to more recent data. The differential spectra were generated for both models using various parton distribution functions as input. Alternative grids within the LY model were used, distinguished by a different choice of the non-perturbative parameters, g_i (see Appendix A for more details). In order to properly keep track of the helicity states for the weak decay, annihilations involving different combinations of valence quarks and sea quarks were dealt with separately. The default double differential cross section used the LY production model with the MRSA [44] parton distribution functions.

After generation of the kinematics of the W boson, the mass dependence of the production cross section was folded in. A relativistic Breit-Wigner line shape was used to model the W boson resonance

$$\frac{d\sigma}{dm}(m^2) \propto \frac{m^2}{(m^2 - M_W^2)^2 + \dfrac{m^4 \Gamma_W^2}{M_W^2}} \tag{37}$$

where M_W and Γ_W are the mass and width of the W boson. In $p\bar{p}$ production, however, the mass spectrum differs from the strict Breit-Wigner resonant line shape of the partonic cross section due to the variation of parton flux with parton momentum. This mass dependence has been calculated and the differential cross section is given by

$$\frac{d\mathcal{N}}{dm} \propto \frac{2m}{s} \int_{m^2/s}^1 \frac{dx_1}{x_1} f_{q/p}(x_1) f_{q'/\bar{p}}\left(\frac{m^2}{sx_1}\right) \frac{d\sigma}{dm}(m^2)$$

$$= \frac{1}{m} \mathcal{F} \frac{d\sigma}{dm}(m^2) \tag{38}$$

with

$$\mathcal{F} = \frac{2m^2}{s} \int_{m^2/s}^1 \frac{dx_1}{x_1} f_{q/p}(x_1) f_{q'/\bar{p}}\left(\frac{m^2}{sx_1}\right). \tag{39}$$

Here $f_{q/p(\bar{p})}(x)$ is the probability that a quark or antiquark q in the (anti)proton carries a fraction x of the (anti)proton's momentum. In this equation a sum over all qq' pairs that lead to W boson production is implicit. The factor $\mathcal{F}$ is a dimensionless quantity which will be referred to as the parton luminosity [45]. It has been parametrized as having an exponential mass dependence, $e^{-\beta m}$. The slope parameter β has been treated as a single number, calculated by evaluating the integral using the available parametrizations of the parton distribution functions [46] at a mass of 80 and 91 GeV/c^2 for W boson and Z boson production, respectively. The small mass dependence of β was included in the systematic uncertainty. Table V lists the values of β which are used for W boson and Z boson production for different sets of parton distribution functions. The most recent sets which use nearly identical modern input data are the Martin-Roberts-Stirling set A (MRSA) and CTEQ3M [47] sets. The relative contributions for vector boson production are listed separately for valence quarks and sea-sea quarks. In the event generation the widths of the intermediate vector bosons were fixed to their measured values, $\Gamma(W) = 2.12$ GeV [38] and $\Gamma(Z) = 2.487$ GeV [19].

2. Decay of W and Z bosons

The W boson decay products were generated in the W boson rest frame with an angular distribution depending on which process, valence-valence/sea or sea-sea, is involved. W^+ bosons follow the angular distribution

TABLE V. Parton luminosity slope, valence-valence $(v-v)$, valence-sea $(v-s)$ and sea-sea $(s-s)$ contributions to the W and Z boson production cross section at $\sqrt{s}=1.8$ TeV.

	$W^{\pm}$ production			Z^0 production		
pdf	$\beta\times100$ (GeV^{-1})	$v-v$ and $v-s$ (%)	$s-s$ (%)	$\beta\times100$ (GeV^{-1})	$v-v$ and $v-s$ (%)	$s-s$ (%)
MRS E$'$	0.980	82.7	17.3	0.869	84.7	15.3
MRS B	1.054	82.7	17.3	0.897	85.0	15.0
HMRS B	1.048	75.5	24.5	0.932	77.7	22.3
KMRS B0	1.022	79.2	20.8	0.908	81.4	18.6
MRS D0$'$	1.220	78.9	21.1	1.077	80.9	19.1
MRS D$'$-	1.277	79.9	20.1	1.097	81.7	18.3
MRS H	1.264	79.0	21.0	1.104	81.0	19.0
MRS A	1.282	79.6	20.4	1.101	81.0	19.0
MRS G	1.297	80.3	19.7	1.107	81.6	18.4
MT B1	1.076	83.1	16.9	0.925	85.4	14.6
CTEQ 1M	1.204	79.6	20.4	1.038	81.3	18.7
CTEQ 1MS	1.206	79.9	20.1	1.030	81.6	18.4
CTEQ 2M	1.274	79.4	20.6	1.078	81.0	19.0
CTEQ 2MS	1.231	79.7	20.3	1.043	81.2	18.8
CTEQ 2MF	1.225	78.7	21.3	1.054	80.2	19.8
CTEQ 2ML	1.310	79.7	20.3	1.113	81.4	18.6
CTEQ 3M	1.224	79.7	20.3	1.051	81.1	18.9
GRV H0	1.237	82.0	18.0	1.095	80.5	19.5

$$\frac{d^2\sigma}{dy\,d\cos\,\theta^*}\sim(1-\cos\,\theta^*)^2\cdot\left(\frac{1}{2}\frac{d\sigma_s^{W^+}}{dy}+\frac{d\sigma_v^{W^+}}{dy}\right)$$

$$+(1+\cos\,\theta^*)^2\cdot\frac{1}{2}\frac{d\sigma_s^{W^+}}{dy} \qquad (40)$$

where the subscripts v and s refer to valence and sea contributions, respectively, and the $+z$ direction is chosen along the proton direction. Here θ^* is the center of mass angle between the electron direction and the $q\bar{q}$ axis.

The $q\bar{q}\rightarrow ll$ production cross section at the Z boson resonance is proportional to

$$(g_V^{q\,2}+g_A^{q\,2})(g_V^{l\,2}+g_A^{l\,2})(1+\cos^2\,\theta^*)+4g_V^q g_A^q g_V^l g_A^l\cos\,\theta^*. \qquad (41)$$

Because the lepton charge is unmeasured, the $\cos\,\theta^*$ term averages to zero. The leptons were therefore generated with a $(1+\cos^2\,\theta^*)$ angular distribution and the $u\bar{u}$ and $d\bar{d}$ contributions to the production weighted with their respective coupling strengths, $g_V^{q\,2}+g_A^{q\,2}$. Here g_V^q and g_A^q are the vector and axial-vector coupling strengths of quark q to the Z boson

$$g_V^q=I_3^q-2Q_q\sin^2\,\vartheta_W \qquad (42)$$

$$g_A^q=I_3^q \qquad (43)$$

with I_3 the third component of the weak isospin and Q_q the charge of the quark. I_3^q is $+\frac{1}{2}$ for the charge $\frac{2}{3}$ quarks and $-\frac{1}{2}$ for the charge $-\frac{1}{3}$ quarks. The value $\sin^2\,\vartheta_W=0.2317$ [18] was used.

3. Radiative processes

Radiative W boson and Z boson decays, $q'\bar{q}\rightarrow W\rightarrow e\nu(\gamma)$ and $q\bar{q}\rightarrow Z\rightarrow ee(\gamma)$, must be properly simulated in the Monte Carlo program to extract correct values for M_W and M_Z (see Appendix B). Because the ee and $e\nu$ invariant masses are smaller in these decays than the corresponding vector boson masses, the experimentally measured mass distributions were shifted toward lower values.

The rates and distributions in lepton and photon momenta were generated to $\mathcal{O}(\alpha)$ following reference [48]. Using this calculation, in the decay of the Z boson either of the electrons (but not both) may radiate. In W boson decays, the electron or W boson may radiate the photon. Approximately 30% of $W\rightarrow e\nu$ decays and 60% of $Z\rightarrow ee$ decays had a photon of 50 MeV or more in the final state. The calculation does not include processes that in the limit of a zero width boson would be considered $W\gamma$ or $Z\gamma$ production. Therefore, initial state radiation was not included in the calculation, nor was the production of a virtual high mass W boson which decays to an on-shell W boson and a photon. In $W\gamma$ and $Z\gamma$ production, M_W and M_Z were correctly obtained from the dilepton invariant masses ($e\nu$ or ee) and the γ direction was not strongly correlated with that of either lepton. Its presence produced a background not fundamentally different from that of other processes.

In implementing radiative decays in the Monte Carlo simulation, three experimental scenarios were considered: (i) When the γ was produced inside the electron cone, taken to be a radius of $R=0.2$ in $\eta-\phi$ space, the γ was measured as part of the electron. The neutrino momentum, obtained from the missing transverse energy in the event, was calculated

correctly. Therefore, the invariant mass of the $e\nu$ system is the W boson mass, and the transverse mass and transverse momentum of the W boson was properly calculated. (ii) If the γ was far from the electron, that is outside a cone of radius $R=0.4$, the photon retains its identity. The electron energy was measured correctly, and p_T^γ becomes part of the recoil against the W boson, $\vec{p}_T^W(\text{meas})=\vec{p}_T^W(\text{generated})-\vec{p}_T^\gamma$. The transverse mass of the $e\nu$ system was calculated correctly, but was shifted downward because the $e\nu$ invariant mass is smaller than the W boson mass. Therefore, M_W was mismeasured. (iii) If the γ was produced in the region between $R=0.2$ and $R=0.4$, it alters the shape of the electron shower. Isolation and electron identification cuts then resulted in inefficiencies that can affect the W boson mass if not properly simulated in the Monte Carlo.

In the Monte Carlo simulation, the fraction of the electron's energy in the region between $R=0.2$ and $R=0.4$ was generated according to the experimental distribution measured in W boson events. The photon energy was added to the electron energy and the event was discarded if it failed the isolation cut. If the event survived the isolation cut and the radial distance $R_{e\gamma}$ between the γ and e, was less than 0.3, the γ momentum was added to the electron's and the W boson mass was correctly calculated, as in the first case above. If the radial distance was greater than $R_{e\gamma}=0.3$, the γ momentum was not added to the electron's and the reconstructed W boson mass and transverse momentum were shifted downward.

C. Detector simulation

The production of likelihood templates in M_T required large Monte Carlo samples. Twenty million generated events were required to sufficiently eliminate effects of statistics in the likelihood function. To study the effects of systematic uncertainties many complete analyses were needed. The combination of these requirements made a fast detector simulation essential.

After production and decay products were boosted into the laboratory frame, the parameters whose measurements were described in the previous section were utilized in this simulation as follows.

(i) The energies of the generated electrons and radiative photons, if they were present and retained their identity, were scaled by the measured EM energy scale. The generated transverse momenta were then smeared according to the measured resolution, as was the generated electron angle.

(ii) The transverse momentum of the recoil system was taken to be the negative of the generated transverse momentum of the W boson, $\vec{p}_T^{rec}=-\vec{p}_T^W$. Its magnitude was scaled by the product of the measured EM energy scale and the relative response of the hadronic and EM calorimeters. Smearing was added according to the jet energy resolution. The hadronic content of $Z\rightarrow ee$ events and the electrons from the Z boson decay were modeled in the same fashion as $W\rightarrow e\nu$ events.

(iii) The underlying event, denoted by $\vec{u}_T(\mathcal{L})$, was modeled using collider minimum bias events, which mimic the debris in the event due to spectator portion interactions and
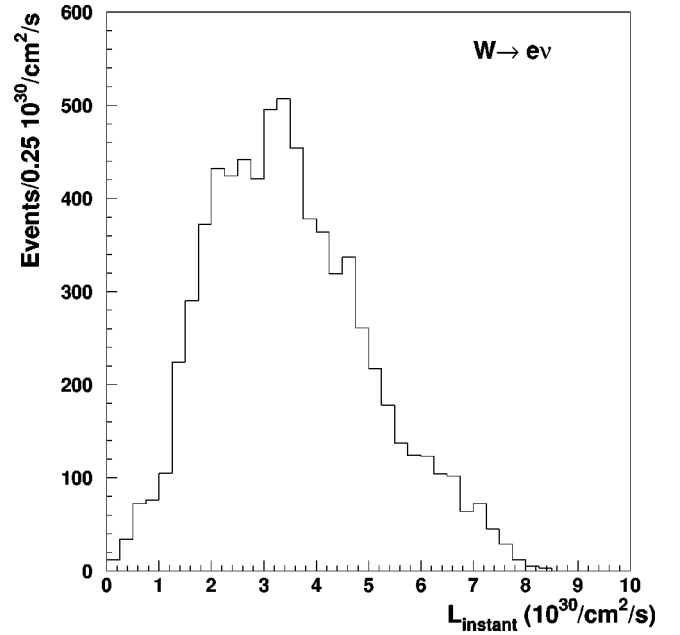
FIG. 20. Distribution in instantaneous luminosity of the W events used in the W boson mass measurement.

the pile-up associated with multiple interactions. The use of minimum bias events properly includes any residual energy which might be present from previous crossings as well as detector effects. A library of minimum bias triggers was created in bins of luminosity in order to correctly simulate overlapping event and noise characteristics of the data. Events were chosen according to the distribution of instantaneous luminosities observed during the run as shown in Fig. 20. (See the discussion in Appendix C.) Figure 21 shows the $\not{E}_T$ and total scalar E_T distributions of the minimum bias events used. The average $\not{E}_T$ is 3.93 GeV with an rms of 2.69 GeV. The mean total scalar E_T is 67.1 GeV with an rms of 39.8 GeV. (The total scalar E_T distribution is shown for completeness only, as this quantity is not used in the event modeling.)

(iv) The generated and smeared recoil hadronic energy vector and the underlying event hadronic energy vector were superimposed on one another to form a simulation of the total hadronic deposition.

(v) The vertex for each generated event was taken to be that of the minimum bias event.

(vi) The efficiencies and cuts were applied to the smeared quantities.

1. Underlying event discussion

In the data, the contribution from the underlying event cannot be separated from the measured recoil energy. In the simulation of the W events the recoil and the underlying event were treated separately. The superposition in the Monte Carlo of the underlying event and the production of the W boson and its decay is laced with intricate details. Although the average energy deposition per read-out tower in minimum bias events was very small, its effect on the W boson mass measurement is of crucial importance mainly because the corrections were correlated with the electron direction. Its presence affects not only the measurement of the electron energy but also the measurement of the missing
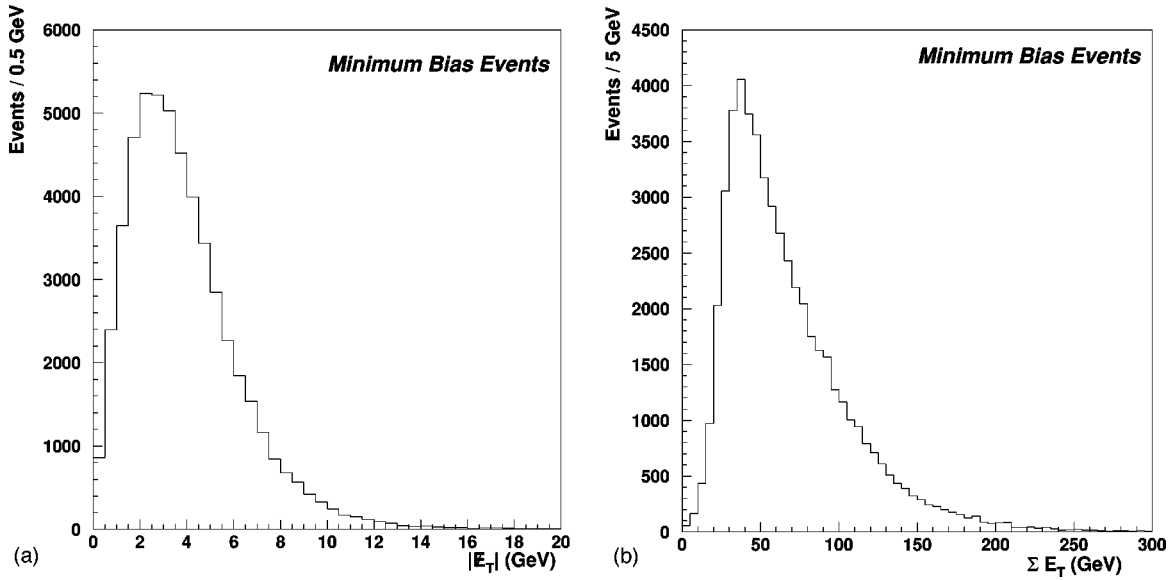
FIG. 21. (a) $\not{E}_T$ and (b) ΣE_T distributions of the minimum bias events used to model the $W \rightarrow e\nu$ and $Z \rightarrow ee$ underlying event.

transverse energy. Equation (14) shows that the neutrino transverse momentum differs from the measured missing transverse energy because of the presence of $\vec{u}_T$.

The clustering algorithm for electron identification used in this analysis was dynamic so the cluster size can vary from event to event. This complicates a description of the underlying event contribution to the electron energy. However, the clustering approach was found to be numerically equivalent to a window in (η, φ) space having a constant size of 0.5×0.5. As this will facilitate the discussion, this window analog consisting of a fixed set of 25 towers with $(\Delta \eta \times \Delta \varphi) = 0.1 \times 0.1$ will be used to illustrate the size of the effects of the underlying event on the electron energy measurement.

Because a 0.5×0.5 window in (η, φ) space is used to model the electron cluster, the cluster contains not only those cells which carry a very large energy because of the incident electron, but also those cells whose energies are just above the zero-suppression threshold. To incorporate the effects of the energy flow of the underlying event in the model, detector effects needed to be taken into account, in particular the effect of the zero-suppression. Calorimeter depositions were only read out if the absolute value of the magnitude of the energy fell outside the zero-suppression limits. This results in two distinct effects. First, small energy depositions due to the low energy tails of the electron shower which fall below the zero-suppression limit are lost, and a correction must be applied to the reconstructed electron energy. Second, the energy read out for cells which are very close to the zero-suppression threshold and which are part of the electron cluster will on average register an energy due to the asymmetric pedestal distribution. This energy is not part of the true electron energy but is an artifact of the calorimeter readout scheme. To determine the true electron energy, the size of these effects must be determined. It should also be noted that when a cell registers a very large energy, that energy is unaffected by any instrumental effects, notably any zero-suppression effects. Thus, it is important to know how many towers a typical electron occupies.

In the following subsection, first the effect of the energy flow of the underlying event on the measured energy of the electron will be discussed. The corrections to the measured electron energy introduced by the zero-suppression will then be detailed.

2. Underlying event energy and electron simulation

The 0.5×0.5 window in (η, φ) centered around the electron contains not only the energy of the electron but also the energy from the underlying event. The measured electron transverse energy, $_m\vec{p}_T^e$, is thus given by:

$$_m\vec{p}_T^e \simeq \vec{p}_T^e + \vec{u}_T^{25} \tag{44}$$

where $\vec{p}_T^e$ refers to the true electron transverse energy, folded with the appropriate resolution, and $\vec{u}_T^{25}$ is the underlying event contribution inside the 25 towers defining the electron cluster. The latter term has been estimated from W events by rotating the electron cluster in azimuth and measuring the average energy flow per tower. Care was taken to ensure that the rotated cluster was isolated and was not in proximity to any jet activity. The energy flow per tower was found to be 16.8 MeV. The average energy flow under the electron is therefore $\vec{u}_T^{25} = 25 \times 16.8\hat{e} = 420\hat{e}$ MeV, with $\hat{e}$ a unit vector in the electron direction.

This contribution has also been determined from minimum bias events, spanning an appropriate range in luminosity. An average energy flow of 15.3 MeV per tower was found. The difference of 1.5 MeV between the two methods is attributed to the presence of the W recoil. A value of 16.8 MeV per tower has been used in the simulation. The uncertainty on the average energy flow is reflected in the systematic uncertainty due to this source.

To each of the two terms in Eq. (44), a correction needed to be applied due to zero-suppression. Under normal running conditions, calorimeter cells were not read out if the signal was within 2σ of the mean pedestal for that channel; that is,

the read-out was zero-suppressed. As a consequence, the tails of the electron shower which fell within the zero-suppression limits, $\vec{u}^{e}_{T_{zs}}$, were lost. The average energy that was lost below the 2σ zero-suppression threshold was estimated to be $\vec{u}^{e}_{T_{zs}} = -152\hat{e}$ MeV for electrons from W decays, using a detailed GEANT simulation.

Because the absorber medium in the calorimeter is uranium, which is a natural β-emitter, the pedestal distributions were asymmetric. Additionally, some asymmetry in the pedestal distributions was introduced due to the shaping electronics [26]. Therefore, even when no particle strikes a read-out tower, the zero-suppressed energy read out for that tower was on average not zero. This zero-suppression contribution has been studied by analyzing non-zero-suppressed minimum bias events. By comparing the energy per 0.1×0.1 read-out tower measured in these events to the energy that results after applying the zero suppression offline, the energy per read-out tower of EM and the first FH layers, was 7.55 MeV higher than in non-zero-suppressed events. It should thus be realized that the average energy flow of 16.8 MeV per tower, derived above, has two contributions. The first contribution is from the true energy flow in the event, determined to be 9.23 MeV per tower. The second contribution is an artifact of the zero-suppression, due to the asymmetric pedestal distributions, which adds an energy of 7.55 MeV per tower to the read-out.

As mentioned before, a minimum bias event was used to model the event underlying the W boson. The presence of the electron from the W decay affected the energy flow in the underlying event. Notably, the read-out towers occupied by the electron had a very large energy deposition and therefore were not affected by the zero-suppression correction. For the W data, the electron occupied on average 8 ± 3 towers. Therefore, applying the zero-suppression correction to all 25 read-out towers of the electron cluster, which has been assumed above, is incorrect. This was corrected by applying the correction to only the 17 channels within the cluster that on average were zero-suppressed or, equivalently, by subtracting out the zero-suppressed pedestal energy from the 8 cells that on average were read-out with the electron. Thus, a correction $\vec{u}^{ue}_{T_{zs}} = -8 \times 7.55\hat{e}$ MeV needed to be applied to the energy flow under the electron, $\vec{u}^{25}_{T}$.

To summarize, the measured electron transverse energy, in MeV, is given by

$$_{m}\vec{p}^{e}_{T} = \vec{p}^{e}_{T} + \vec{u}^{e}_{T_{zs}} + \vec{u}^{25}_{T} + \vec{u}^{ue}_{T_{zs}} = \vec{p}^{e}_{T} - 152\hat{e} + 25 \times (9.23 + 7.55)\hat{e}$$
$$- 8 \times 7.55\hat{e} \qquad (45)$$

with (1) $\vec{p}^{e}_{T}$ the true electron transverse energy folded with its resolution; (2) $\vec{u}^{e}_{T_{zs}}$ the energy of the tails of the electron shower lost due to the zero-suppression, determined to be $-152\hat{e}$ MeV; (3) $\vec{u}^{25}_{T}$ the energy flow from the underlying event within the 0.5×0.5 window in (η, φ) defining the electron cluster, given by $25 \times (9.23 + 7.55)\hat{e}$ MeV; and (4) $\vec{u}^{ue}_{T_{zs}}$ the correction to the energy flow of the underlying event due to the presence of the electron which corrects for the zero-suppression effect of the underlying event for the towers oc-

cupied by the electron, $-8 \times 7.55\hat{e}$. When all of these effects were taken into account, an addition of an average of $E^{el}_{UE} = 207$ MeV to the generated electron along the electron direction was required in order to correctly simulate the measured electron p_{T}. This is indicated in the appropriate entry in Table IV.

3. Underlying event energy and recoil energy

The measured recoil energy in the detector is a combination of the true recoil of the W boson and the contribution of the underlying event. In the simulation the true recoil of the W boson was taken to be $\vec{p}^{rec}_{T}$ and the underlying event was simulated using a minimum bias event. Therefore the measured recoil was given by

$$_{m}\vec{p}^{rec}_{T} \simeq -\vec{p}^{W}_{T} + \vec{u}_{T}. \qquad (46)$$

The underlying event vector $\vec{u}_{T}$ was taken to be the sum of the E_{T} of all calorimeter cells in the minimum bias event. However, a correction needed to be applied to the underlying event energy vector due to the presence of the electron in W events. Recall that in the data analysis the recoil momentum was determined by subtracting the electron transverse energy from the total measured transverse energy in the event. Therefore the energy flow under the electron from the underlying event, pointing along the electron, should be subtracted from $\vec{u}_{T}$. In the simulation, the recoil was thus calculated as

$$_{m}\vec{p}^{rec}_{T} = -\vec{p}^{W}_{T} + \vec{u}_{T} - \vec{u}^{25}_{T} = -\vec{p}^{W}_{T} + \vec{u}_{T} - 25 \times (9.23 + 7.55)\hat{e}. \qquad (47)$$

Note the absence of the $\vec{u}^{ue}_{T_{zs}}$ term, which does not need to be applied here since $\vec{u}_{T}$ is from a minimum bias event in which no high p_{T} electrons are present.

The underlying event model and the resolution in p^{rec}_{T} has been verified using the η imbalance in Z boson events, defined previously. Since the magnitude of the E_{T} in minimum bias events was of the same order as that of the p_{T} of the vector boson, the width of the distribution of the η imbalance [see Fig. 10(b)] was very sensitive to the underlying event contribution. The rms of the η imbalance distribution in Fig. 10(b), after the correction for the hadronic energy scale has been applied, is $\sigma = 4.44 \pm 0.18$ GeV. This is the band shown in Fig. 22. The number of minimum bias events added to the Monte Carlo W event in order to mimic the underlying event was varied to match the width of the η imbalance that was observed in the data. In this optimization the jet resolution was held constant. The points in Fig. 22 show the Monte Carlo predicted widths as function of the number of minimum bias events. The number of minimum bias events preferred by the data was $N_{\text{min. bias}} = 0.98 \pm 0.06$ events. Since this number is consistent with 1.0, one minimum bias event was used to model the underlying event in W and Z boson production.

4. Underlying event and the neutrino momentum

The neutrino momentum is a derived quantity which follows directly from the electron and recoil measurements:
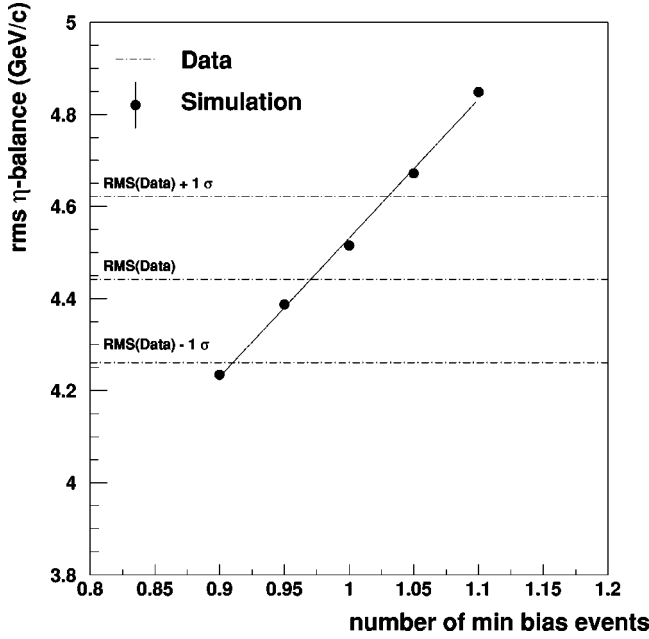
FIG. 22. Sensitivity of the width of the η imbalance distribution to the number of minimum bias events used to simulate the underlying event in the Monte Carlo simulation (points). The line is the result of a linear least-squares fit. The bands (dotted-dashed) correspond to the nominal and $\pm 1\sigma$ measurements of the width in *Z* boson events.

$$\vec{E}_T = -{}_m\vec{p}_T^{\,rec} - {}_m\vec{p}_T^{\,e} = -\vec{p}_T^{\,rec} - {}_m\vec{p}_T^{\,e} - [\vec{u}_T - \vec{u}_T^{\,25}]$$

$$= -\vec{p}_T^{\,rec} - \vec{p}_T^{\,e} - \vec{u}_T - \vec{u}_{T_{zs}} \tag{48}$$

where $\vec{u}_{T_{zs}} = \vec{u}_{T_{zs}}^{\,e} + \vec{u}_{T_{zs}}^{\,ue}$. Note that $\vec{u}_T - \vec{u}_T^{\,25}$ represents the energy vector of the underlying event with the region that the electron occupies excised.

There are two equivalent ways to view the effect of the underlying event. If one uses for the neutrino momentum the second line above, then the measured electron energy, including the contribution from zero suppression and the energy from the underlying event, appears in the neutrino and the electron in *W* decays and in both electrons in *Z* decays. This correction then cancels in the ratio of the two masses. Then what is important is the amount of the underlying event energy which should be excluded from the determination of the *W* boson recoil energy because it is inside the electron cluster. Alternatively, if one examines the expression for the neutrino momentum given in the third line above, only the total recoil momentum and the total underlying energy enter. The zero suppression correction is still irrelevant, appearing in the neutrino, the *W* electron, and the two electrons from the *Z* boson decay. Now the correction to the electron energy from the energy flow from the underlying event that appears inside the electron cluster does not cancel completely in the M_W/M_Z ratio.

The missing transverse momentum differs from the neutrino momentum because of the presence of $\vec{u}_T$. This effect has no counterpart in *Z* boson decays and it changes the measured transverse mass and must be properly modeled. As described above, in the Monte Carlo simulation $\vec{u}_T$ was obtained from minimum bias events. If there were a biased region of the calorimeter which made $\vec{u}_T$ directional, this effect would be accounted for in the Monte Carlo events. Although the above is dependent on properly extracting small energies in the calorimeter, many of the effects cancel in the ratio M_W/M_Z.

D. Application of efficiencies

After simulating the vector boson event kinematics, the efficiencies of the trigger as well as the electron identification efficiency as a function of $u_\parallel$ were applied, using the measured kinematic quantities. Fiducial cuts in η and ϕ were made as in the data. Using the measured quantities, the transverse mass was calculated and the same selection criteria as in the data were applied: $m_T > 50$ GeV/c^2; $E_T^e > 25$ GeV/c; $\not{E}_T > 25$ GeV; and $p_T^W < 30$ GeV/c.

E. Comparison of data with Monte Carlo calculation

Comparisons of various distributions of the simulated quantities with data are shown in this section. The distributions comparing the data and the results of the simulation are area normalized. The Monte Carlo calculation was generated at the final *W* boson mass value of this analysis obtained from the transverse mass fit. In the comparisons the data are generally shown as points with statistical errors; the simulation is shown as the histogram.

1. Characterization of the $W \rightarrow e\nu$ candidates

The primary measurables in $W \rightarrow e\nu$ events are the energy and direction of the electron $\vec{E}$ and the transverse momentum of the recoil $\vec{p}_T^{\,rec}$. In addition, there are a variety of derived quantities which are especially sensitive to the presence of inefficiencies or biases which serve as important checks. The comparison between the data and the Monte Carlo simulation for $W \rightarrow e\nu$ events in the electron polar angle $\cos(\theta_e)$ and the transverse momentum of the *W* boson p_T^W are shown in Figs. 23 and 24. There is reasonable agreement between the simulation and the data in both distributions.

Because of its strong correlation with the lepton transverse momenta, $u_\parallel$, defined previously, is an important quantity. As was noted in Section IV D 2, a bias in $u_\parallel$ distorts the available momentum phase space of the leptons and results in a softer or harder lepton p_T spectrum, depending on that bias. Since $u_\parallel$ involves both the electron identification efficiency and the hadronic energy scale, it is advantageous to study the distribution in the angle between the recoil system and the electron, as well as a distribution in $u_\parallel$ itself. Figure 25 shows the distribution in $\varphi_{el} - \varphi_{rec}$.

Note that for small p_T^W, assuming perfect electron identification, the *W* boson recoil would be distributed uniformly in φ around the electron direction. However, the distribution in $\varphi_{el} - \varphi_{rec}$ is asymmetric. There are two sources for this asymmetry. The dominant effect is simply the kinematics of $W \rightarrow e\nu$ decays. For transversely boosted *W* bosons, on average the electron carries away $p_T^e \approx p_T^W/2$ along the $\vec{p}_T^W$ direction, having a magnitude of $\approx M_W/2$ for small values of
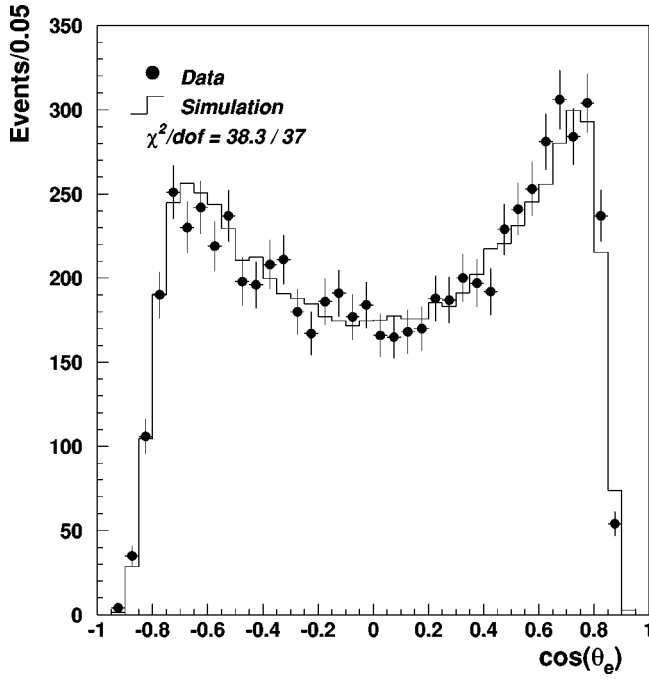
FIG. 23. Angular distribution of electrons from $W \rightarrow e\nu$ decays (points) compared to the simulation (histogram). The asymmetry is due to the fact that the luminous region was not located at $z = 0$ cm in the DØ detector, but was rather centered at $z = -7.98$ cm.

p_T^W. This implies that $\langle u_{\parallel} \rangle \approx -\langle p_T^{W^2} \rangle / M_W$. Since the mean value of p_T^W is approximately 9 GeV/c (see Fig. 24), $\langle u_{\parallel} \rangle$ is about -1 GeV and the distribution in the difference in azimuthal angle of the electron and the recoil tends to favor
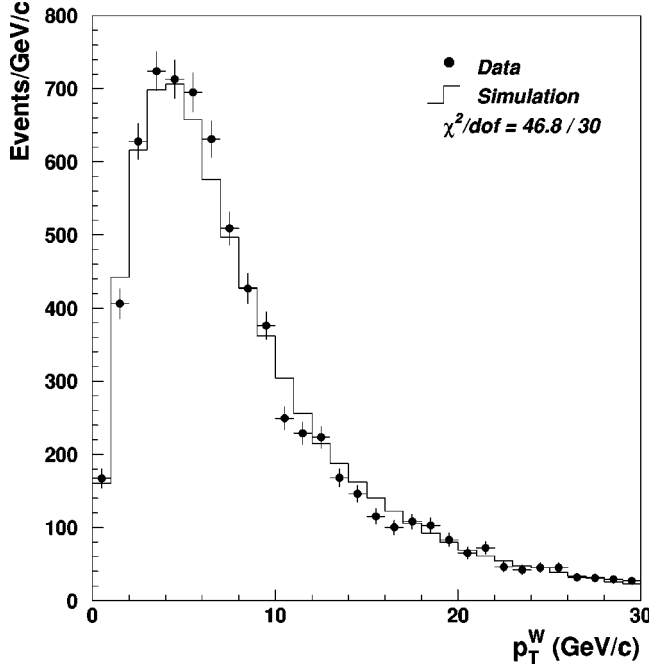
FIG. 24. Distribution of p_T^W from $W \rightarrow e\nu$ decays (points) compared to the simulation (histogram). The mean of the data (simulation) distribution is 8.11 GeV/c (8.20 GeV/c). Both distributions have the same rms, 5.97 GeV/c.
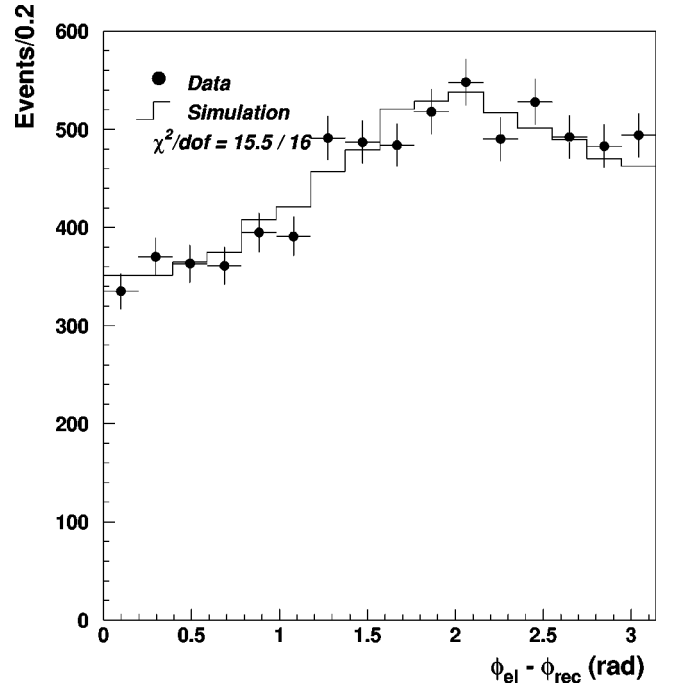
FIG. 25. Distribution of the angle between the recoil jet and the electron in the transverse plane from $W \rightarrow e\nu$ decays (points) compared to the simulation (histogram).

negative values of $u_{\parallel}$. The second effect which enhances the asymmetry is due to a decrease in electron identification efficiency as function of $u_{\parallel}$. The value of $u_{\parallel}$ is an indication of the proximity of the recoil jet to the electron. For high positive values of $u_{\parallel}$ the recoil jet is close to the electron and can spoil its signature. The observed excellent agreement between the simulation and the data indicates that the event kinematics and the electron identification efficiency are modeled adequately.

Figures 26 and 27 show the correlation between $\langle u_{\parallel} \rangle$ and p_T^e and p_T^{ν}. An important feature of the transverse mass is that, unlike p_T^e and p_T^{ν}, M_T is relatively uncorrelated with $u_{\parallel}$ as shown in Fig. 28. This shows clearly one of the advantages of using the transverse mass to obtain the W boson mass. The correlation between $u_{\parallel}$ and p_T^W is shown in Fig. 29.
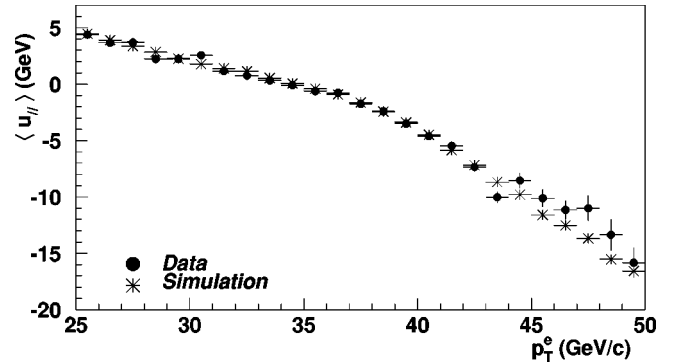
FIG. 26. Distribution of the mean $u_{\parallel}$ versus p_T^e from $W \rightarrow e\nu$ decays (points) compared to the simulation ($*$).
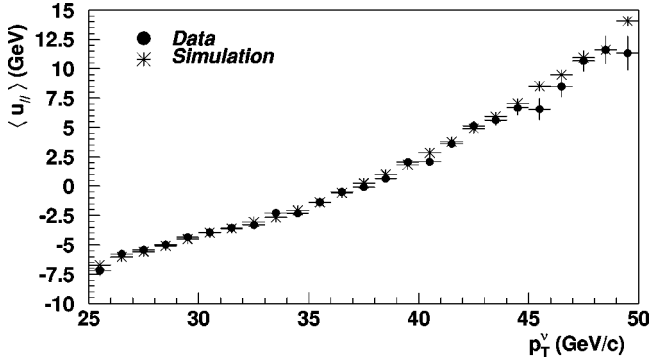
FIG. 27. Distribution of the mean $u_\parallel$ versus p_T^ν from $W \to e\nu$ decays (points) compared to the simulation (∗).

FIG. 29. Distribution of the mean $u_\parallel$ versus p_T^W from $W \to e\nu$ decays (points) compared to the simulation (∗).

Figure 30 shows the distribution in $u_\parallel$ itself. Note that there has not been a subtraction for background. The mean value of $u_\parallel$ for the data is $\langle u_\parallel \rangle = -1.19 \pm 0.08$ GeV whereas the simulation gives $\langle u_\parallel \rangle = -1.13 \pm 0.02$ GeV. An average correction for the QCD and $Z \to ee$ background has been applied to the value just quoted for $\langle u_\parallel \rangle$ for the Monte Carlo.

The distribution of $u_\perp$, Fig. 31, defined as the projection of the recoil jet onto the axis perpendicular to the electron direction, is a measure of the resolution of the recoil system. Its mean value is close to zero, as expected. For the data $\langle u_\perp \rangle = 0.025 \pm 0.087$ GeV with an rms of 7.4 GeV; the simulation gives $\langle u_\perp \rangle = 0.024$ GeV with an rms of 7.5 GeV.

2. Characterization of the $Z \to ee$ candidates

The measured quantities in $Z \to ee$ events are the energy and direction of both electrons and the transverse momentum of the recoil system. Equally important are the determination of derived quantities of the Z boson kinematics. Figures 32 and 33 show the comparison in electron energy E_{el} and the transverse momentum distribution from the recoil system, p_T^{rec}.

VI. FITTING PROCEDURE

The Monte Carlo event generation was performed for 21 equidistant mass values binned at intervals of 100 MeV/c^2 in the transverse mass for W boson spectra, 200 MeV/c^2 in

invariant mass for Z boson spectra, and 100 MeV/c for the transverse momentum spectra.

An unbinned maximum likelihood fit was used to determine the vector boson mass using the normalized Monte Carlo spectra as templates. The log-likelihood was calculated for the data for the 21 different generated masses. Since the templates were binned whereas the data were unbinned, a quadratic interpolation between adjacent bins in the templates was performed. The log-likelihood values for the 21 different vector boson masses were fit to a parabola and the minimum was taken to be the fitted mass value. A decrease of half a unit in the log-likelihood is the quoted single standard deviation statistical uncertainty.

The likelihood distribution need not be Gaussian, depending on the range of the parameter fit, the intrinsic shape of the spectrum and the resolution function. This is particularly true for spectra with a sharp edge like the Jacobian peak in the distributions considered here. Both quadratic and cubic polynomial fits were performed to the log-likelihood. The differences were small and for all results presented here, the values from the quadratic fit are quoted.

Any Monte Carlo-based fitting procedure should satisfy the requirements that, if the procedure is applied to an ensemble of Monte Carlo generated data samples, it returns the input values with which the events were generated and, secondly, that the rms spread of the values for the fitted parameter be consistent with the mean statistical uncertainty of the fit to each individual data sample. This was done for an ensemble of 125 generated data samples of 8000 events each. The average statistical error for each of the three different W boson mass fits is: $\delta(M_T) = 130$, $\delta(p_T^e) = 183$ and $\delta(p_T^\nu) = 248$ MeV/c^2, respectively. The average fitted mass values are $M_W(M_T) = 80.410 \pm 0.013$, $M_W(p_T^e) = 80.398 \pm 0.017$ and $M_W(p_T^\nu) = 80.420 \pm 0.021$ GeV/c^2, in good agreement with the input value of 80.400 GeV/c^2 within the statistical accuracy of the generated templates. They are consistent with the rms spread of the distribution of the fitted masses, $\text{rms}(M_T) = 145 \pm 9$, $\text{rms}(p_T^e) = 188 \pm 12$ and $\text{rms}(p_T^\nu) = 237 \pm 15$ MeV/c^2, respectively. Figure 34 shows the distribution of fitted mass values and fit uncertainty for W bosons as obtained from a fit to the transverse mass for this ensemble.

As discussed in the previous section, backgrounds were

FIG. 28. Distribution of the mean $u_\parallel$ versus M_T from $W \to e\nu$ decays (points) compared to the simulation (∗).
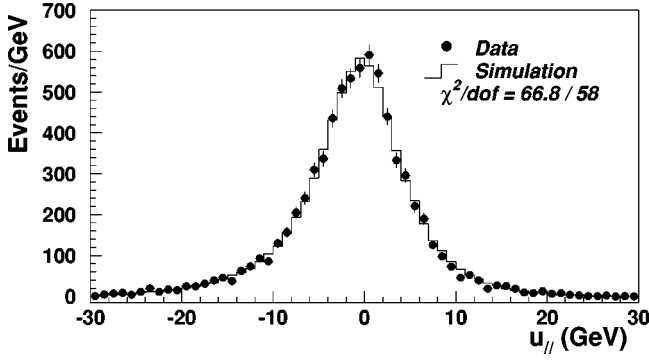
FIG. 30. Comparison of the $u_\parallel$ distribution from $W \to e\nu$ events (points) and the Monte Carlo simulation (histogram).

not included in the event simulation. Their effect on the mass determination was taken into account through inclusion of the shape of the background spectrum in the likelihood distributions. The background was properly normalized to the expected background fraction in the relevant fitting range. All results were corrected for backgrounds.

A. Results of Z boson mass fits

The dielectron invariant mass spectrum for the central-central (CC-CC) event topology, with the corresponding best fit of the templates to the data, is shown in Fig. 35. The events in the mass range $70 < m_{ee} < 110$ GeV/c^2 were used to extract the Z boson mass. The final fitted Z boson mass for events which require both electrons in the central calorimeter is

$$M_Z = 91.070 \pm 0.170 \ \text{GeV}/c^2. \tag{49}$$

The error is statistical only. Figure 35 also shows the relative likelihood distribution and signed $\sqrt{\chi^2}$ of the fit for central-central electrons.

B. Results of W boson mass fits

The W boson mass was obtained from fits to the transverse mass of the W boson, M_T (Fig. 36), the electron p_T (Fig. 37) and the neutrino p_T spectrum (Fig. 38). The transverse mass fit was performed over the range $60 < M_T < 90$
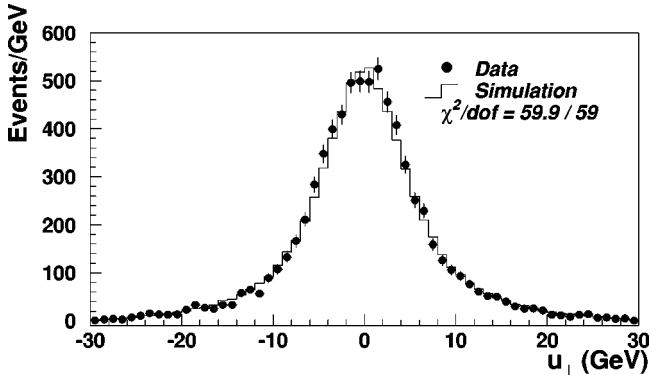
FIG. 31. Comparison of the $u_\perp$ distribution from $W \to e\nu$ events (points) and the Monte Carlo simulation (histogram).
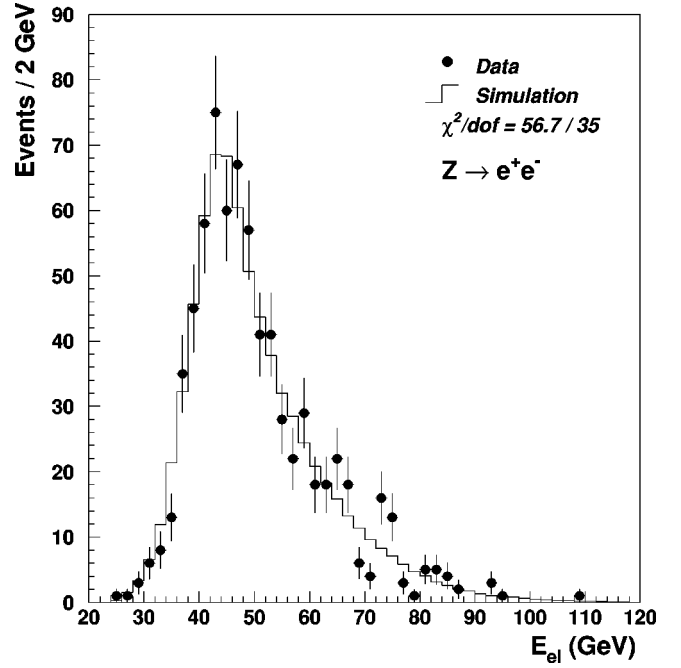
FIG. 32. Comparison of the electron energy distribution from $Z \to ee$ events (points) and the simulation (histogram).

GeV/c^2, which contains 5982 events. Placing the lower edge at 60 GeV/c^2 removed most of the QCD background. Since the probability for finding events in the very high transverse mass tail was small, relatively small fluctuations in the number of observed high transverse mass events can significantly affect the fitted mass. Given that the high transverse mass tail
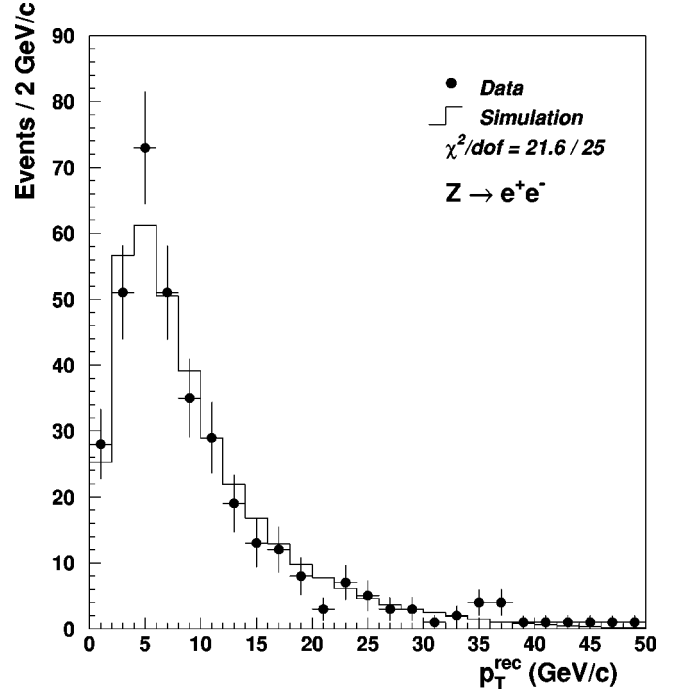
FIG. 33. Comparison between the Z boson transverse momentum distribution as measured from the recoil system in $Z \to ee$ events (points) and the simulation (histogram).
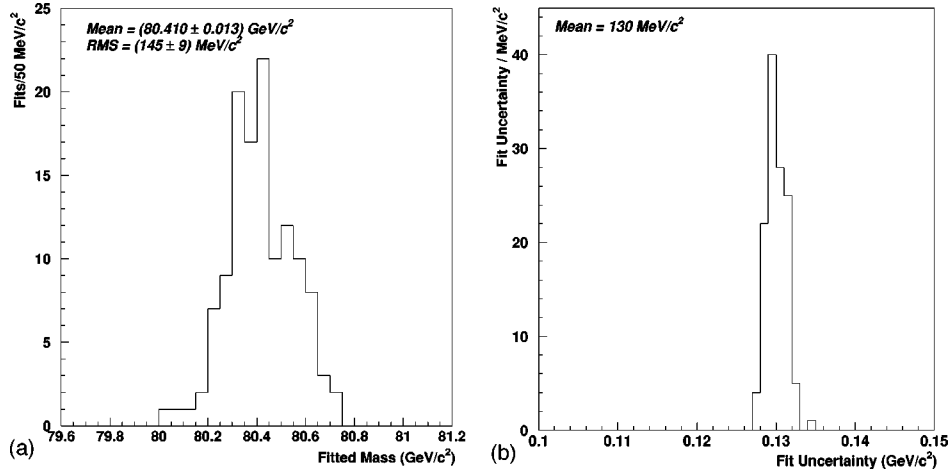
FIG. 34. Distribution of (a) the fitted masses and (b) the fit uncertainties from fits to the transverse mass distributions for an ensemble of 125 Monte Carlo generated data samples of 8000 $W \rightarrow e\nu$ decays.

of the QCD background was rather poorly known, a high M_T cut of 90 GeV/c^2 was also imposed. A transverse momentum range of 30 to 45 GeV/c was used for fits to the transverse momentum spectra. There were 5520 events in the fitting range for the electron transverse momentum spectrum and 5457 events for the neutrino transverse momentum spectrum. It should be noted that the fitting windows were placed on ''uncorrected'' energies, that is, electron energies which had not been scaled as described in Sec. IV.

The final fitted masses from the three spectra are

$$M_W(M_T) = 80.350 \pm 0.140 \ \text{GeV}/c^2 \tag{50}$$

$$M_W(p_T^e) = 80.300 \pm 0.190 \ \text{GeV}/c^2 \tag{51}$$

$$M_W(P_T^\nu) = 80.045 \pm 0.260 \ \text{GeV}/c^2. \tag{52}$$

The errors are again statistical only. Note that the W boson mass determination using the transverse mass is the most precise. After taking into account the small offset, which resulted in a change of the W boson mass of 5 MeV/c^2 as described in Sec. IV A, the measured mass ratio is

$$M_W/M_Z = 0.88114 \pm 0.00154 \tag{53}$$

where the error is statistical only.

VII. SYSTEMATIC SHIFTS AND UNCERTAINTIES

In this analysis, the W boson mass was obtained from a fit to the spectrum in transverse mass defined in Eq. (12). The Z boson mass was obtained from a fit to the spectrum in invariant mass of the two electrons, defined in Eq. (10). In this section the uncertainties in the measured masses that could arise from mismeasurements of the terms in these equations are described. Note that the errors quoted will be those for the measured W boson mass which is extracted from the ratio of the fitted W boson and Z boson masses; correlations between the two masses have been taken into account.

Unless otherwise noted, the determinations of the shifts in mass due to the various uncertainties have been obtained

through Monte Carlo studies and are labeled ''Monte Carlo'' in the tables. In these studies, high statistics Monte Carlo event samples were generated with the parameter in question varied within its allowed range. These samples were then fit to the templates with the nominal settings to determine the systematic error. The errors on these shifts reflect the statistical error on the simulation. The sensitivity, $\partial M_W/\partial P$, where P is the parameter that has been varied, was determined from a linear fit to the shifts in mass over a representative range around the nominal value of the parameter. Values in the tables labeled ''Data'' are the shifts in mass when the data are fit to a template in which one of the parameters deviates from its preferred value, with the others unchanged. No error is quoted for these data shifts, since it would be meaningless.

A. Electron energy scale uncertainty

As discussed in Sec. IV A, many systematic effects due to the calorimeter scale which are common to the measurement of both the W and Z bosons cancel in the ratio of their masses. However, there are small effects that can bias the measured Z boson mass in ways which do not cancel in the ratio, M_W/M_Z, and they are discussed in the next section.

1. Uncertainties in M_Z

The first source of a possible bias in the Z boson mass measurement is the background under the Z boson resonance. The nominal multi-jet background in the $Z \rightarrow ee$ sample and the Drell-Yan contribution caused a shift in the reconstructed Z boson mass of $+39 \pm 12$ MeV/c^2. The uncertainty on this correction has been estimated by varying the slope of the background which resulted in a change in the overall background level from 3.2% to 8.2%. Such a variation in the background results in a variation of 20 MeV/c^2 in M_Z, which was taken to be the systematic uncertainty on the Z boson mass from the background contribution. Other uncertainties arose due to parton distribution functions, radiative corrections, and a small fitting error. Among these, the change in parton luminosity for the different parton distri-
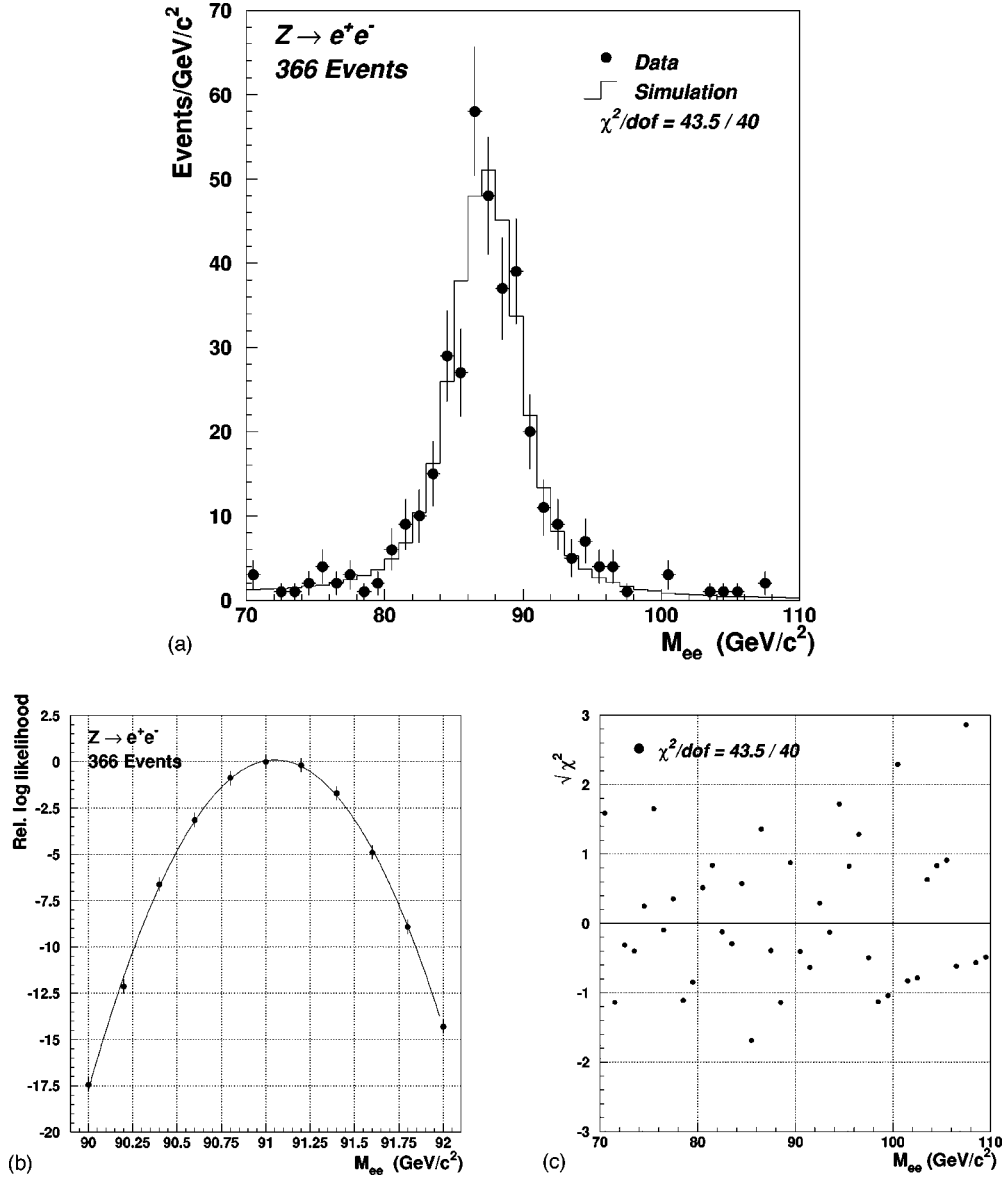
FIG. 35. (a) The central dielectron invariant mass distribution for Z events (points) and the best fit of the simulation (histogram), (b) the corresponding relative log-likelihood distribution and (c) signed $\sqrt{\chi^2}$ distribution.

bution functions was most significant. Varying the parton luminosity slope β within the range given by the various parton distribution functions considered in this analysis, $1.030 \times 10^{-2} < \beta < 1.113 \times 10^{-2}$, along with the other effects results in an overall 35 MeV/c^2 uncertainty in the Z boson mass.

2. Total M_W uncertainty due to electron scale

As was noted in Sec. IV A, the largest contribution to the overall scale uncertainty was due to the number of Z boson events. This statistical component was 150 MeV/c^2. In addition, the uncertainty due to the possible nonlinearity in the calorimeter response as determined by the combined $m_{J/\psi}$, m_{π^0}, and M_Z analysis (related to the uncertainty in δ) was assigned as 25 MeV/c^2. Combining these in quadrature with the systematic uncertainties just discussed resulted in the overall scale uncertainty assignment which is rounded up to 160 MeV/c^2.

B. Uniformity of electron energy response uncertainty

The data were corrected for the observed azimuthal variations in energy response of the different calorimeter modules, reducing the error from this source to a negligible level. Any residual non-uniformity in response was taken into account through the constant term in the energy resolution.

A non-uniform response in η, however, can introduce a bias in the mass determination, arising from the fact that the kinematic distribution of electrons from Z boson decays differs from that in W boson decays. The electrons from Z boson decays have a different average η than the electrons from W boson decays, even when event samples are very large. Moreover, a non-uniformity can distort the differential distributions. A possible η dependence of the calorimeter response will thus not cancel in the ratio of the two masses.

To address this, the response of the different η regions of the detector were scaled in the Monte Carlo with respect to
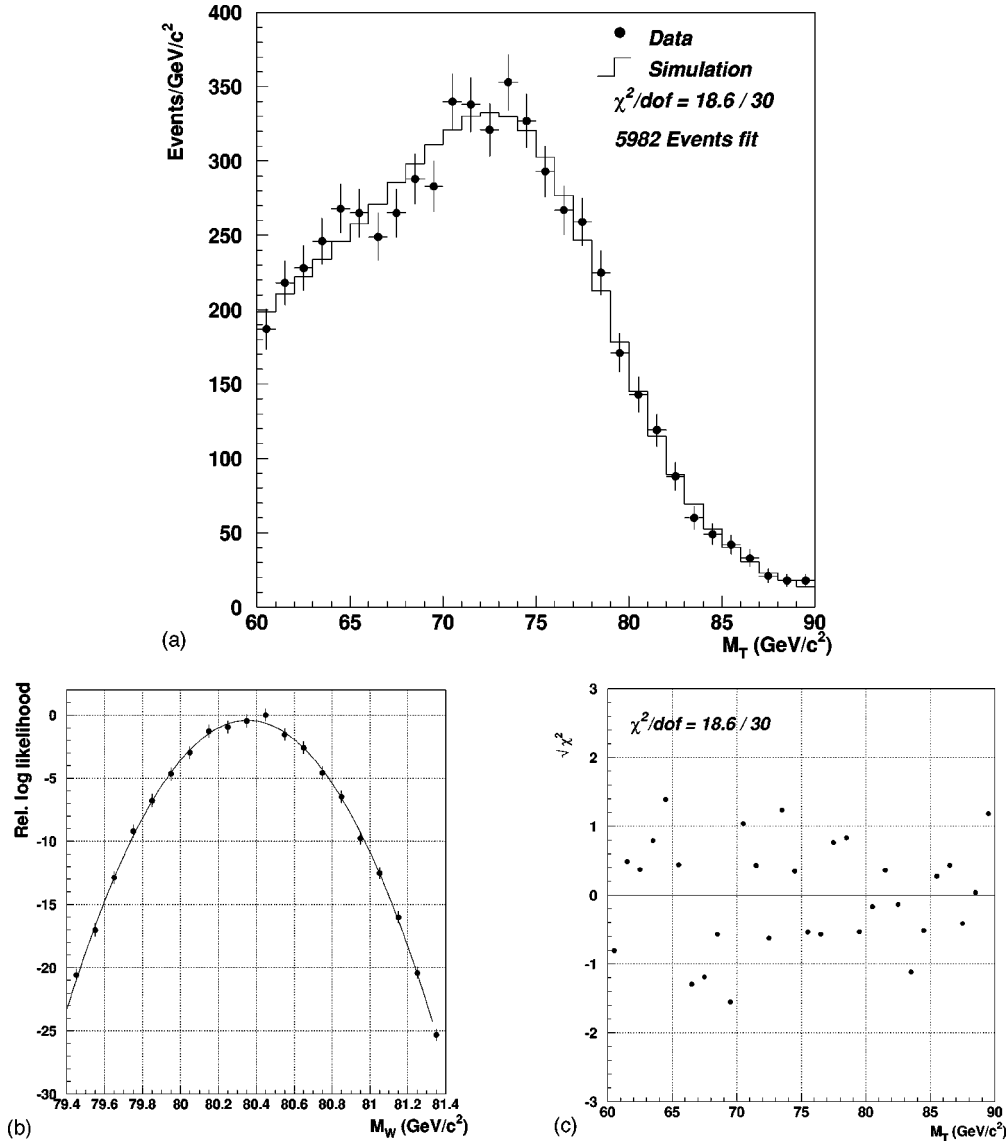
FIG. 36. (a) The transverse mass distribution for *W* events (points) and the best fit of the simulation (histogram), (b) the corresponding relative log-likelihood distribution and (c) signed $\sqrt{\chi^2}$ distribution.

the nominal uniform response. Two sets of scale factors were used, corresponding to the response of two EM modules measured in the 1991 test beam. These scale factors were applied in discrete steps in η, following the read-out geometry of the calorimeter, and varied from 0.985 to 1.013 over the central pseudorapidity range. The observed shifts in fitted mass are listed in Table VI. Assuming the η response of the test beam modules typified the variation in uniformity, a systematic uncertainty on the *W* boson mass from the transverse mass fit of 10 MeV/c^2 was assigned due to this uncertainty.

C. Electron energy resolution uncertainty

The electron energy resolution in the central calorimeter was parametrized as discussed in Sec. IV C 3. Most effects which degrade the resolution affected the resolution function constant term. For example, spatial non-uniformities in the

detector response and electronics gain variations contributed to the constant. The sampling term varies very little, from 1.9–2.4 %, as the electron p_T is varied over the range 30–45 GeV/c. Therefore changing only the constant term and noting the change in the *W* boson mass was sufficient to accommodate most sources of uncertainty in the energy resolution.

To study the dependence of the *W* boson mass on the resolution, the constant term was varied in the Monte Carlo simulation. The *W* boson mass increases if a resolution smaller than actually exists in the data is used in the Monte Carlo simulation. Better resolution in the Monte Carlo results in a sharper Jacobian edge and the fitted mass shifts upward to accommodate the larger resolution tail in the data. The transverse mass distribution was most sensitive, since the Jacobian edge was best preserved. For the p_T spectra the edge is smeared, due in part to the transverse boost of the *W* boson. Table VII lists the changes in *W* boson mass for all three fits when varying the constant term by 0.5% from its
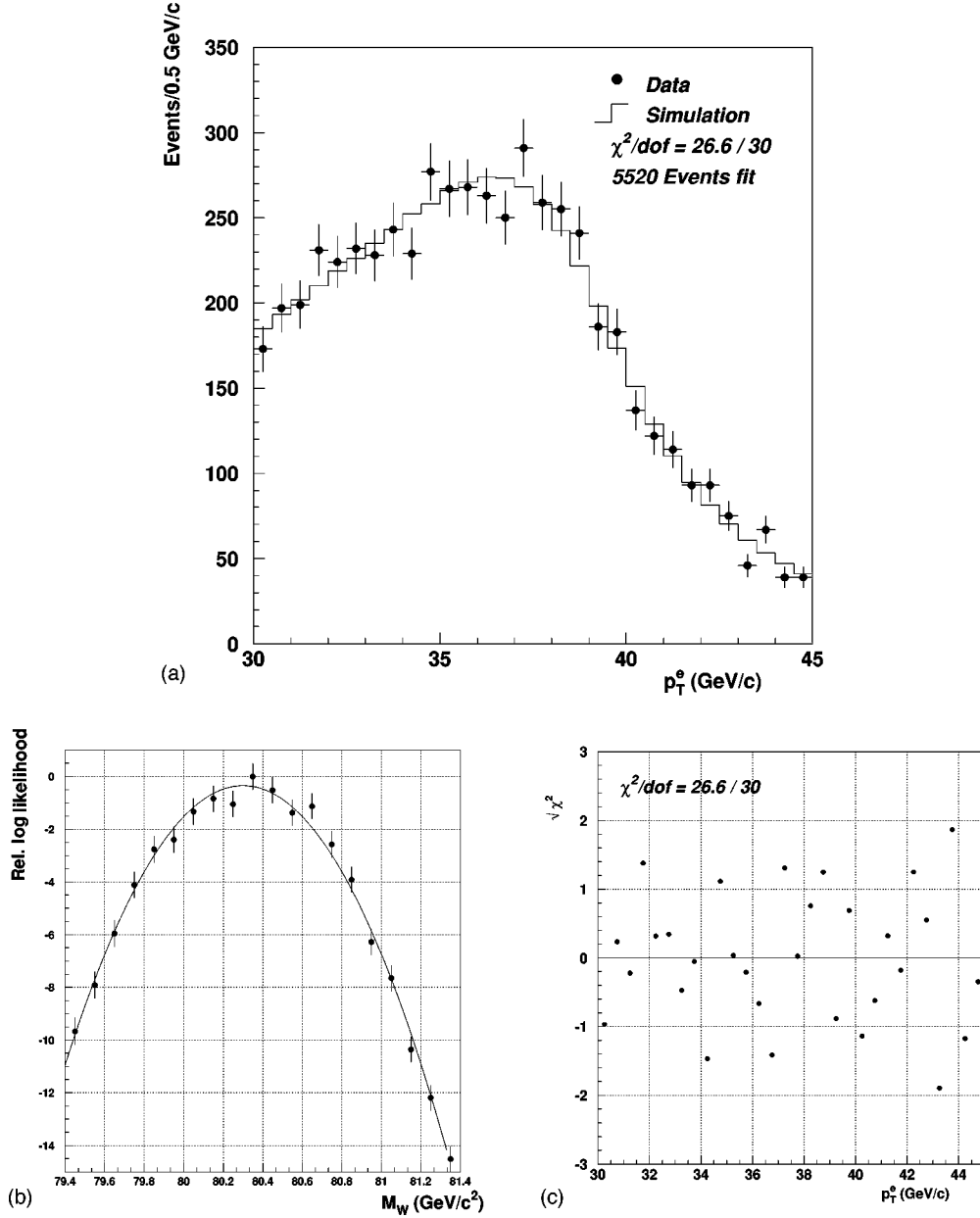
FIG. 37. (a) The electron transverse momentum distribution for W events (points) and the best fit of the simulation (histogram), (b) the corresponding relative log-likelihood distribution and (c) signed $\sqrt{\chi^2}$ distribution.

nominal value of 1.5%. An uncertainty in the measured W boson mass for the transverse mass fit of 70 MeV/c^2 was assigned according to this variation.

D. Electron angle uncertainty

The electron polar angle is defined by the position of the electromagnetic cluster in the calorimeter and the position of the *cog* of the CDC track. Recall from Eq. (18) in Sec. III that a scale factor, α_{CDC}, was applied during the data analysis to correct the bias in the z position of the *cog* of the CDC track. The uncertainty in the W boson mass due to the uncertainty in α_{CDC} has been determined by applying varying scale factors to the z position of the CDC *cog* in the W boson and Z boson data and fitting to the standard templates. By

varying the CDC scale factor around the nominal value within its tolerance of 0.002 for the W boson and Z boson data sample simultaneously, the uncertainty on the W boson mass was determined to be 50 MeV/c^2.

E. Hadronic energy scale uncertainty

The energy scale of the vectors $\vec{u}_T$ and $\vec{p}_T^{rec}$, which both include hadronic energy, was not the same as the scale of $\vec{p}_T^e$, which contains only electromagnetic energy and was calibrated by the Z boson mass. The relative hadronic to electromagnetic energy scale is set using Z boson events and the scale obtained is $\kappa = 0.83 \pm 0.04$. The sensitivity of the measured W boson mass was obtained by varying the value of κ within its uncertainty in the Monte Carlo generation of
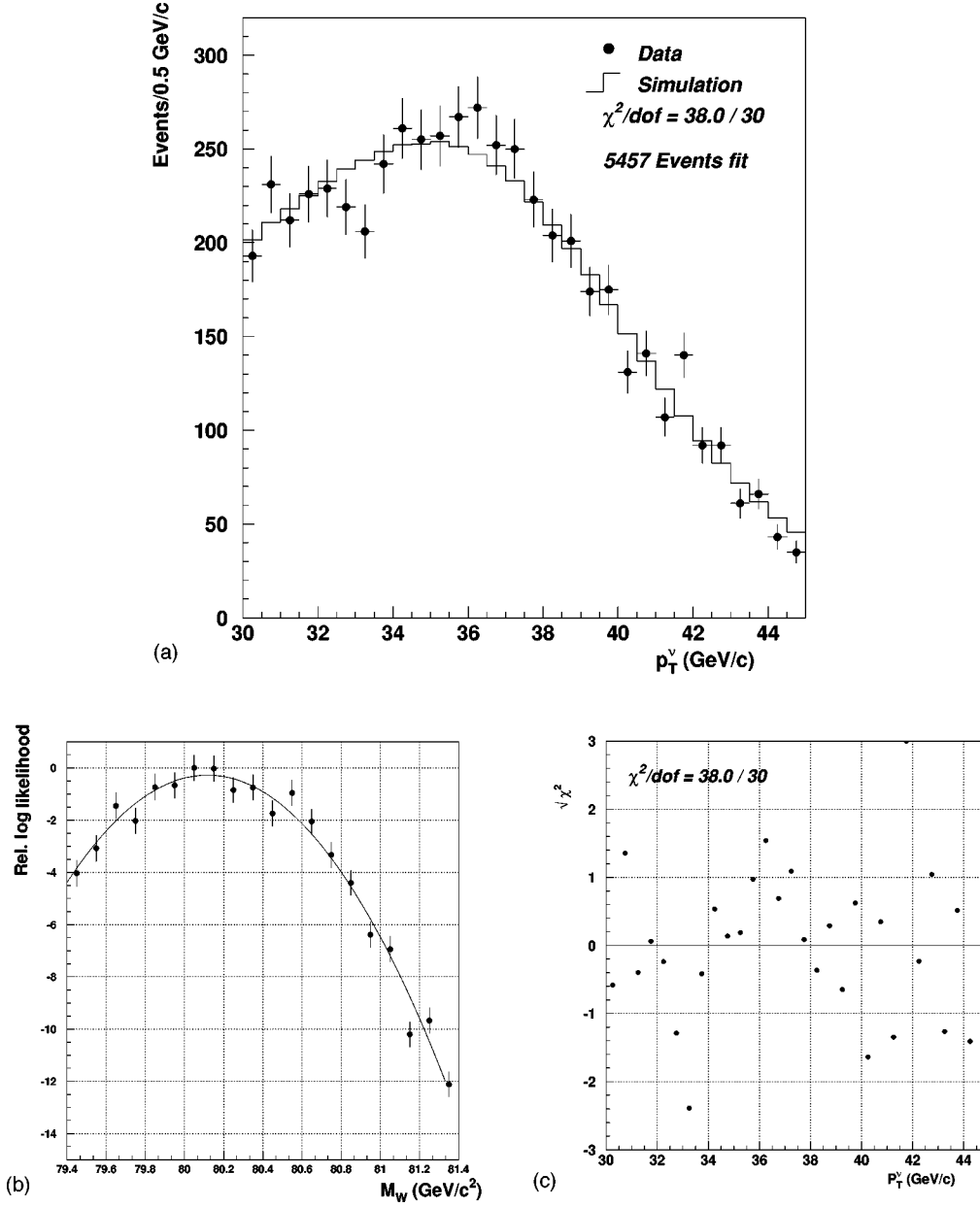
FIG. 38. (a) The neutrino transverse momentum distribution for *W* events (points) and the best fit of the simulation (histogram), (b) the corresponding relative log-likelihood distribution and (c) signed $\sqrt{\chi^2}$ distribution.

the templates. The 0.04 variation in hadronic energy scale produced a 50 MeV/c^2 uncertainty on the *W* boson mass from the transverse mass fit, where an increase in the scale factor resulted in an increase of the measured *W* boson mass. Table VIII lists the change in *W* boson mass when

varying the hadronic energy scale factor by 0.04 from its nominal value for all three fits. The mass obtained from the p_T^e fit was affected by a change in the hadron energy scale through the electron identification efficiency as function of $u_{\parallel}$.

TABLE VI. Change in *W* and *Z* boson masses in MeV/c^2 if a non-uniform calorimeter η response is assumed, bracketed by the variations observed for two EM modules exposed in a test beam.

η response	ΔM_W M_T fit (MeV/c^2)	ΔM_W p_T^e fit (MeV/c^2)	ΔM_W p_T^ν fit (MeV/c^2)	ΔM_Z m_{ee} fit (MeV/c^2)
Module A	-6 ± 16	-7 ± 22	-49 ± 30	-2 ± 6
Module B	$+5\pm16$	-15 ± 22	-26 ± 30	-8 ± 6

TABLE VII. Uncertainty on the W boson mass in MeV/c^2 due to a change in the constant term of the electromagnetic energy resolution by 0.5%. The upper numbers correspond to the lower constant term.

Fitted spectrum	Monte Carlo ΔM_W (MeV/c^2)	Sensitivity $\dfrac{\partial M_W}{\partial C}\left(\dfrac{\text{MeV}/c^2}{\%}\right)$	Data ΔM_W (MeV/c^2)
M_T	$^{+58}_{-44}\pm17$	-112 ± 19	$^{+43}_{-44}$
p_T^e	$^{+44}_{-8}\pm22$	-54 ± 14	$^{+11}_{-27}$
p_T^ν	$^{+64}_{-20}\pm30$	-56 ± 19	$^{+47}_{-5}$

F. Hadron energy resolution uncertainty

The resolution in p_T^W had two components: the energy resolution of the recoil jet which is aligned with the recoil direction [49], and the underlying event vector $\vec{u}_T$ which was randomly oriented with respect to the recoil. In the Monte Carlo the recoil momentum $\vec{p}_T^{rec}$ was simulated by assuming it is a jet with resolution $\sigma_{had}/E = 80\%/\sqrt{E}$ as discussed above. All of the uncertainty due to this quantity was presumed to be accounted for through variations in the sampling term alone. The second contribution, that from $\vec{u}_T$, dominated the overall resolution in p_T^W. It was obtained directly from the experiment using minimum bias events chosen at the proper luminosity to simulate the underlying event.

The data constrained the number of minimum bias events to $N_{\text{min. bias}} = 0.98 \pm 0.06$. The nominal value used in the simulation was 1.0. The change in W boson mass for various values of the number of underlying events is listed in Table IX. This includes the effect of resolution broadening and the neutrino scale shift which results from changing $\vec{u}_T$. The application of the randomly oriented underlying event has the effect of adding an azimuthally symmetric component to the overall resolution for the total hadron energy vector. The systematic uncertainty on the measured W boson mass due to the uncertainty on the number of minimum bias events is 60 MeV/c^2 for the transverse mass fit.

The mass determined from the p_T^e spectrum was, within errors, not affected by the hadron energy resolution. The W boson mass determined from the other two spectra would increase if a smaller average number of minimum bias events underlying the W boson were used in the Monte Carlo since the resolution improves.

TABLE VIII. Uncertainty on the W boson mass due to the change in p_T^W scale by 0.04. The upper numbers are the change in mass when the p_T^W scale factor increases and the hadronic response is closer to the electromagnetic response.

Fitted spectrum	Monte Carlo ΔM_W (MeV/c^2)	Sensitivity $\dfrac{\partial M_W}{\partial \kappa}\left(\dfrac{\text{MeV}/c^2}{0.01}\right)$	Data ΔM_W (MeV/c^2)
M_T	$^{+55}_{-73}\pm17$	$+12.1\pm1.3$	$^{+42}_{-80}$
p_T^e	$^{+38}_{-29}\pm23$	$+6.7\pm1.7$	$^{+4}_{-38}$
p_T^ν	$^{-161}_{+94}\pm30$	-30.3 ± 2.5	$^{-125}_{+100}$

TABLE IX. Uncertainty on the W boson mass due to a change by 0.1 in the number of minimum bias events underlying the W event. The upper numbers are the change in mass for a higher average number of minimum bias events.

Fitted spectrum	Monte Carlo ΔM_W (MeV/c^2)	Sensitivity $\dfrac{\partial M_W}{\partial\text{\# min.bias}}\left(\dfrac{\text{MeV}/c^2}{0.1}\right)$	Data ΔM_W (MeV/c^2)
M_T	$^{-105}_{+121}\pm17$	-117 ± 5	$^{-253}_{+201}$
p_T^e	$^{-14}_{+29}\pm23$	-20.0 ± 7.0	$^{-55}_{+9}$
p_T^ν	$^{-245}_{+318}\pm30$	-286 ± 14	$^{-535}_{+554}$

The jet energy resolution also contributed to the uncertainty attributed to the overall hadronic energy resolution. Varying the sampling term in the jet energy resolution from 0.6 to 1.0 changes the W boson mass by 65 MeV/c^2, which was taken to be the systematic error due to this source. Table X lists the change in the mass from the different fits when varying the sampling term of the hadronic energy resolution.

G. Energy under the electron uncertainty

The measured electron energy not only consisted of the electron energy itself, smeared by the detector resolution, but also included a contribution from the underlying event. In addition, there was a bias in the electron energy due to zero-suppression in the readout electronics. Following the discussion in Sec. V C the measured electron p_T was modeled as a combination of four terms, $\vec{p}_T^e$, $\vec{u}_{T_{zs}}^e$, $\vec{u}_T^{25}$, and $\vec{u}_{T_{zs}}^{ue}$. The additional contributions to the electron energy point, to a good approximation, along the electron direction with the magnitude of 207 MeV. The uncertainty on this has been estimated to be approximately 50 MeV. The measured neutrino momentum can be written in two equivalent ways:

$$\vec{\not{E}}_T = -\vec{p}_T^{rec} - {}_m\vec{p}_T^e - [\vec{u}_T - \vec{u}_T^{25}] = -\vec{p}_T^{rec} - \vec{p}_T^e - \vec{u}_T - \vec{u}_{T_{zs}}. \tag{54}$$

Using the second equation, the total recoil momentum and the total underlying energy enter in the calculation of the neutrino momentum. Both were well determined by the W boson and Z boson data. Using this approach, the overall uncertainty derived from the measured electron energy in a manner which did not completely cancel in the ratio M_W/M_Z. The zero suppression correction here was quite

TABLE X. Uncertainty on the W boson mass due to the change in the sampling term of the hadronic energy resolution by 0.2. The upper numbers are the change in mass for a larger resolution.

Fitted spectrum	Monte Carlo ΔM_W (MeV/c^2)	Sensitivity $\dfrac{\partial M_W}{\partial S}\left(\dfrac{\text{MeV}/c^2}{10\%}\right)$	Data ΔM_W (MeV/c^2)
M_T	$^{-74}_{+52}\pm17$	-31.5 ± 6.0	$^{-52}_{+31}$
p_T^e	$^{+2}_{-8}\pm23$	-2.5 ± 7.8	$^{-4}_{-26}$
p_T^ν	$^{+95}_{-58}\pm30$	-38.3 ± 11.0	$^{-87}_{+32}$
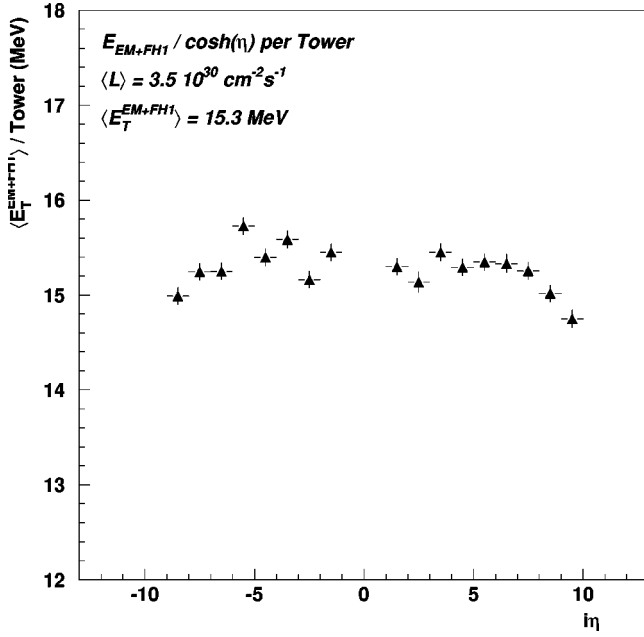
FIG. 39. Average transverse energy flow per electron cluster tower as a function of η measured from minimum bias events.

small, since it contributed to the neutrino and the W boson electron, as well as the two Z boson electrons.

Using the first equation the measured electron energy appeared in both the measured neutrino momentum and the measured electron momentum for W boson decays and in both electrons for Z boson decays. The correction to the electron energy then canceled completely in the ratio of the W boson and Z boson masses. What is important is how much of the underlying energy and W boson recoil energy should be excluded from the event for the $\vec{p}_T^{\,rec}$ determination, because it was inside the electron cone. The method used to determine the uncertainty on the W boson mass from the contribution due to energy under the electron followed this approach.

Three effects were identified that contribute to this uncertainty. Figure 39 shows the average transverse energy flow in an EM tower plus the first FH layer versus tower index (i_η^e). It is seen that the energy flow was constant in η within 0.5 MeV for the central calorimeter. In the Monte Carlo a uniform E_T distribution was assumed and the deviation of a flat distribution from that shaped like the data contributed an uncertainty of approximately 20 MeV/c^2 on the W boson mass.

The second source of uncertainty stems from the fact that the underlying energy in W boson events was measured to be 16.8 MeV per tower in the EM plus FH1 layers, whereas minimum bias events yielded 15.3 MeV. In the Monte Carlo an energy flow of 16.8 MeV was assumed. This difference of 1.5 MeV, most likely due to the presence of the W boson recoil, was treated as an uncertainty on the mass which is equal to $(25 \times 1.5)/2 \simeq 20$ MeV/c^2.

The third source is due to the uncertainty on the number of towers to be excluded from the E_T of the underlying event. In the Monte Carlo, a region of $5 \times 5 = 25$ towers was

excluded. In the data, the number of towers used by the electron in the clustering algorithm varied event by event. This uncertainty on the W boson mass was evaluated by repeating the analysis using another electron clustering algorithm that removed this error completely (see Sec. VIII B). The difference in W boson mass between the two electron clustering approaches led to a 20 MeV/c^2 uncertainty due to this effect. These three uncertainties were summed in quadrature to obtain the total uncertainty on the W boson mass of 35 MeV/c^2 due to the uncertainty in the energy flow underlying the electron.

H. Production model uncertainty

In the generation of the W boson and Z boson events a theoretical model for the vector boson transverse momentum and rapidity spectrum was used. This production model had an uncertainty associated with it which led to an uncertainty in the measured W boson mass. Since parton distributions and the spectrum in p_T^W are correlated, this correlation was addressed in the determination of its uncertainty on the W boson mass. To constrain the production model, both the measured p_T^Z spectrum as well as the published CDF W boson charge asymmetry data [50] were used.

The parton distribution functions were constrained by the CDF measured W boson charge asymmetry data. To accommodate the variation allowed by the asymmetry data while at the same time utilizing the available data from all other experiments, new parametrizations of the CTEQ3M parton distribution function were obtained [51]. The fit used to obtain these parametrizations included the CDF W boson asymmetry data with all data points moved coherently up or down by one standard deviation. These parametrizations will be referred to in the following as ''asymmetry high'' and ''asymmetry low,'' respectively. Figure 40 shows the relative change in the theoretical p_T^Z spectrum for these new parametrizations of the CTEQ3M parton distribution function with respect to the nominal spectrum.

The p_T spectra of the vector bosons were most sensitive to variations in the parameter g_2, which describes the Q^2 dependence of the parametrization of the non-perturbative functions (see Appendix A). Figure 41(a) shows the change in the p_T^Z spectrum when the parameter g_2 is varied significantly from its nominal value. Note that for low p_T, the cross section varies by approximately a factor of two. Figure 41(b) shows the constraint on g_2 by the Z boson data as given by a simple χ^2 test. For the estimate of the uncertainty on the W boson mass, the range for g_2 was limited to $-2\sigma < g_2 < 4\sigma$, which are conservative bounds in agreement with the Z boson data.

To assess the uncertainty due to parton distribution functions and p_T^W input spectrum, the change in W boson mass was noted when varying both the parton distribution function, as determined by varying the measured W boson charge asymmetry, and the g_2 parameter simultaneously. The results of the change in W boson mass are listed in Table XI. A total error on the W boson mass of 65 MeV/c^2 has been assigned due to the uncertainty on the parton distribution functions and the input p_T^W spectrum.
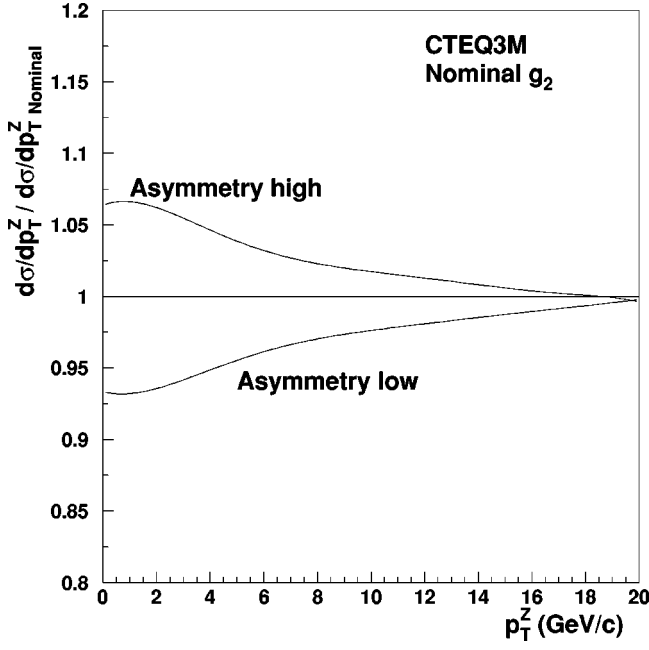
FIG. 40. Ratio of predicted differential cross section in p_T^Z and the nominal cross section for new parametrizations of the CTEQ3M parton distribution function.

The change in W boson mass obtained from high statistics Monte Carlo studies for different parton distribution functions, compared to the nominal MRSA parton distribution function is shown in Table XII. An uncertainty of 50 MeV/c^2 in the measured W boson mass could be attributed to the choice of parton distribution function. Note that this uncertainty is only listed for completeness. The more conservative estimate, varying both the parton distribution functions and the p_T^W spectrum simultaneously, was taken as the final uncertainty due to these sources.

Finally, the finite width of the W boson was taken as 2.1 ± 0.1 GeV and the effect on the W boson mass due to its uncertainty was found to be 20 MeV/c^2.

I. Background uncertainty

The presence of background caused a bias in the determination of the mass. The shift in mass has been determined by including the nominal background spectra in the likelihood templates. Systematic uncertainties arose due to the uncertainty on the overall background contribution and the shape of the background spectrum.

The QCD multi-jet background contribution to the signal sample is $(1.6 \pm 0.8)\%$. The contribution of $Z \rightarrow ee$, in which one electron is not identified, is $(0.43 \pm 0.05)\%$. The presence of these backgrounds introduced a shift in measured mass of $+33$ MeV/c^2 and $+4$ MeV/c^2, respectively, for the transverse mass fit. The background levels have been varied within the quoted uncertainties. The shape of the QCD multi-jet background for the transverse mass distribution was varied as shown by the curves labeled "excursions" in Fig. 42. Similarly, the shape of the $Z \rightarrow ee$ background was varied. The total systematic uncertainty on M_W due to the variations in the QCD and $Z \rightarrow ee$ background is 30 MeV/c^2 and 15 MeV/c^2, respectively. An overall uncertainty of 35 MeV/c^2 has been assigned to the uncertainty in the background.

J. Radiative decay uncertainty

The parameters used in the modeling of radiative decays were the minimum separation between the electron and photon for the photon to retain its identity $R_{e\gamma}$ and the minimum energy of the radiated photon E_γ^{min}. The uncertainty in the value of these parameters led to an uncertainty in the measured W boson mass. Uncertainties can also arise from inefficiencies caused by the photon affecting the electron shower
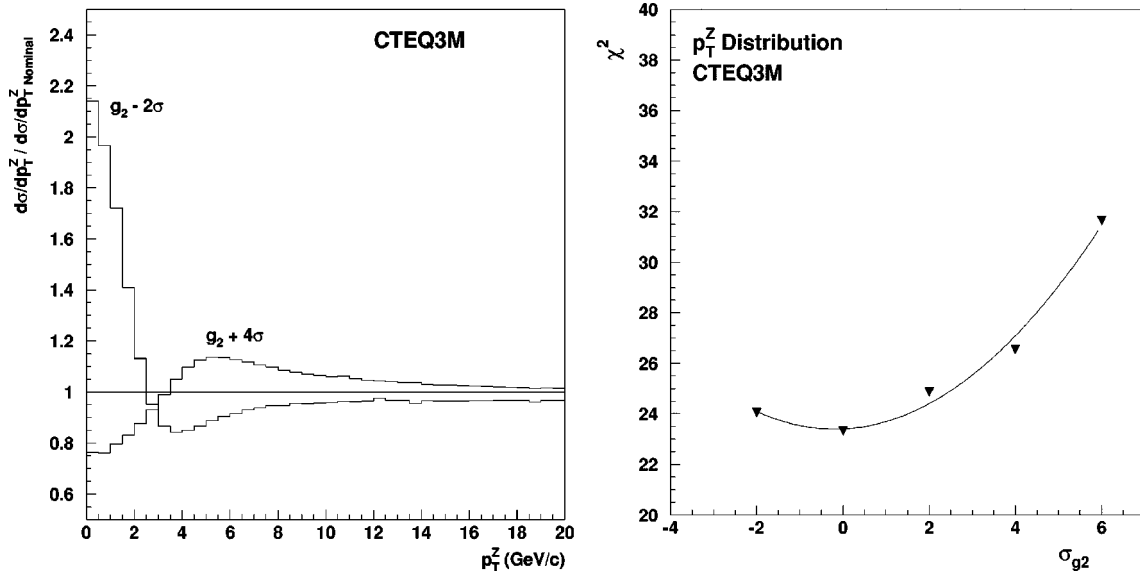
FIG. 41. (a) Ratio of predicted differential cross section in p_T^Z and the nominal cross section versus p_T^Z when the parameter g_2 is varied by multiple standard deviations from its nominal value in the Ladinsky-Yuan prediction and (b) the distribution in χ^2 for a comparison between data and Monte Carlo of the p_T^Z spectrum versus the variation of g_2 in units of its standard deviation.

TABLE XI. Shift in the *W* boson mass in MeV/c^2 when using different parametrizations of the parton distribution functions and p_T^W spectrum. There is a statistical uncertainty of 17, 24 and 31 MeV/c^2 on each value for the M_T, p_T^e and p_T^ν fit, respectively.

| | $g_2-2\sigma$ | g_2 | $g_2+2\sigma$ | $g_2+4\sigma$ | |
PDF (CTEQ3M)	ΔM_W (MeV/c^2)	ΔM_W (MeV/c^2)	ΔM_W (MeV/c^2)	ΔM_W (MeV/c^2)	Fit
CDF Asym. high	$+32$	$+14$	$+50$	$+11$	M_T
CDF Asym. nominal	-14	0	-37	-30	M_T
CDF Asym. low	-55	-67	-69	-65	M_T
CDF Asym. high	$+125$	$+51$	$+36$	-60	p_T^e
CDF Asym. nominal	$+45$	0	-93	-137	p_T^e
CDF Asym. low	-48	-127	-169	-197	p_T^e
CDF Asym. high	$+64$	$+80$	$+77$	-17	p_T^ν
CDF Asym. nominal	$+40$	0	-43	-78	p_T^ν
CDF Asym. low	-64	-69	-141	-121	p_T^ν

shape, the effect of upstream material on the energy measurement of photons and from theoretical uncertainties.

The electron photon separation parameter $R_{e\gamma}$ was varied by ±0.1 from its nominal value of 0.3 and the effect on the *W* boson mass was noted. From this, an uncertainty of 10 MeV on M_W was determined. In a second independent analysis the correlation between the effect of a photon on the isolation as well as the topological requirements was taken into account through a full detector simulation. The four-vectors of the decay products from radiative decay events were input to the GEANT simulation. The events, processed using the standard reconstruction algorithms, were then subjected to the same selection criteria as the data and electron identification efficiencies were determined as a function of E_T^γ and $R_{e\gamma}$. Modeling the resulting variation of the efficiencies determined in this fashion in the Monte Carlo led, again,

to an uncertainty on the *W* boson mass of 10 MeV/c^2 which is the same as that found in the other method.

The dependence of M_W on $E_\gamma^{\min}$ was negligible. The choice of $E_\gamma^{\min}=50$ MeV was sufficiently low that within the accuracy of the measurement it was insensitive to this parameter.

In the modeling of radiative decays, only order $\alpha_{\rm EM}$ corrections to the lowest order diagrams have been considered and processes in which two or more photons are radiated have been ignored. Also, initial state radiation and finite lepton masses were not included in the calculation. This effect has been estimated to be 10 MeV/c^2 and confirmed by a recent theoretical calculation [52].

Since the effect of radiative decays was large and changed the *W* boson and *Z* boson masses in a way that did not cancel in the ratio, it was important to also evaluate the effect when

TABLE XII. Change in the *W* and *Z* boson masses in MeV/c^2 with varying parametrizations of the structure of the proton. Amounts quoted are relative to the MRSA fit. The asterisk indicates those parton distribution functions considered obsolete for this analysis.

PDF	ΔM_W M_T fit (MeV/c^2)	ΔM_W p_T^e fit (MeV/c^2)	ΔM_W p_T^ν fit (MeV/c^2)
MRSA	—	—	—
MRSB[*]	-90 ± 19	-196 ± 24	-86 ± 34
MRSE[*]	-136 ± 19	-168 ± 24	-198 ± 34
HMRSB[*]	-157 ± 19	-280 ± 24	-204 ± 34
KMRSB0[*]	-175 ± 19	-238 ± 24	-244 ± 34
MRSD0$'$	-74 ± 19	-109 ± 24	-26 ± 34
MRSD$'$-	-31 ± 19	-9 ± 24	$+8\pm34$
MRSH	-30 ± 19	-47 ± 24	-70 ± 34
MTB1[*]	-135 ± 19	-260 ± 24	-144 ± 34
CTEQ1MS[*]	-29 ± 19	-109 ± 24	-1 ± 34
CTEQ2M	$+20\pm19$	$+1\pm24$	$+53\pm34$
CTEQ2MS	0 ± 19	-26 ± 24	$+62\pm34$
CTEQ2MF	-59 ± 19	-112 ± 24	-84 ± 34
CTEQ2ML	$+29\pm19$	$+19\pm24$	$+57\pm34$
CTEQ3M	-31 ± 19	-75 ± 24	-102 ± 34
GRVH0	-47 ± 19	-88 ± 24	-50 ± 34
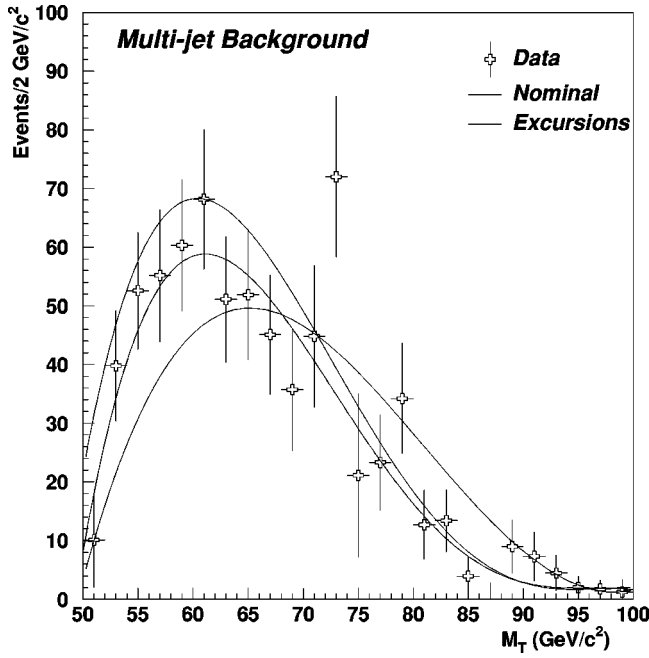
FIG. 42. The measured multi-jet background distribution versus M_T from the data (open crosses). The allowed variations in the shape of the transverse mass spectrum (dotted lines) are shown. The solid line indicates the nominal background distribution.

the photon is produced by bremsstrahlung in the central detector. For the photon to have an effect on the measured W boson mass, it must be separated from the electron in (η, φ) space by at least $R = 0.2$.

The probability for radiating a photon is very strongly peaked at small angles (see Appendix B), with very little dependence on the fraction of the electron's energy carried by the photon [53]. The photon never separates from the electron beyond a cone of 0.2 by radiation alone and therefore external bremsstrahlung has no effect on the W boson mass.

As shown in Appendix B, the electron and photon can also separate if the electron undergoes multiple scattering through a large angle. The angles resulting from multiple scattering are generally larger than those produced in the radiation itself, particularly when the electron is low in energy. In spite of the possibly large angles between the electron and the photon, the probability for this to occur is negligible and it can safely be concluded that bremsstrahlung and multiple scattering have no effect on the measured W boson mass.

A last issue regarding radiation is the energy loss by ionization and by radiative processes where, for example, the electron radiates a photon that does not reach the calorimeter but produces an e^+e^- pair that loses energy by dE/dx. These processes affect the W boson and Z boson mass and produce an offset in the energy scale, which was included in the energy scale determination. Small offsets produced in this way cancel to first order in the mean of the ratio of the W boson to Z boson masses, since the energy is lost to both the neutrino and the electron in each W boson event in which it occurs. In Z boson events only one electron loses the en-

TABLE XIII. Uncertainty on the W boson mass due to uncertainty on the electron identification efficiency as a function of the quantity $u_\parallel$. The upper numbers are the change in mass when the overall efficiency decreases.

	Monte Carlo	Data
Fitted spectrum	ΔM_W (MeV/c^2)	ΔM_W (MeV/c^2)
M_T	$^{+37}_{-9} \pm 17$	$^{+2}_{-13}$
p_T^e	$^{-46}_{+52} \pm 23$	$^{-63}_{+41}$
p_T^ν	$^{+124}_{-143} \pm 30$	$^{+136}_{-95}$

ergy but the probability of such loss is twice as large. Using a GEANT simulation, a study of the effect of upstream material on the photon energy response was carried out. The photon response observed in the GEANT simulation was consistent with the response measured *in situ*, as described in Sec. IV A. Notably, the offset in response was found to be consistent with the *in situ* measurement. Combining all effects an overall systematic uncertainty of 20 MeV/c^2 was assigned to M_W due to radiative effects.

K. Efficiency and bias uncertainties

1. Trigger efficiencies

The effect of the uncertainty in the trigger efficiency has been studied by varying the nominal trigger efficiency distributions in the Monte Carlo within the range determined by the data. This resulted in an uncertainty on the W boson mass of 20, 20 and 60 MeV/c^2 from the M_T, p_T^e and p_T^ν fits, respectively. In addition, the W boson mass was determined from a data sample that did not have the $\not{E}_T$ requirement imposed at the trigger level. The resulting fitted value was different from that using the standard trigger by -29 ± 26 MeV/c^2. The fitted mass from this sample was consistent with the nominal fit result within the statistical uncertainty, taking into account the large overlap between the two data samples.

2. Efficiency as a function of $u_\parallel$

The transverse mass is relatively uncorrelated with the uncertainty in $u_\parallel$, unlike the fits to the lepton transverse momentum spectra, which are very sensitive to this efficiency. The nominal variation in the electron identification efficiency encompasses the band shown in Fig. 16. The results of large statistics Monte Carlo data samples generated with the nominal variations of the efficiency are given in Table XIII. Also listed are the results of the change in mass when fitting the data to templates generated with the different efficiencies. It is seen that the Monte Carlo studies and the data exhibit the same behavior. The corresponding electron identification uncertainty on the W boson mass is 20, 70 and 115 MeV/c^2 from the M_T, p_T^e and p_T^ν fits, respectively.

L. Error in the fitting procedure

The W boson mass was obtained from an unbinned maximum likelihood fit in which the data were fit to transverse

TABLE XIV. Summary of systematic errors on the W boson mass from the three mass fits. Those errors that are strongly correlated with the measured Z boson mass are indicated by an asterisk.

Source	Variation used	$\sigma(M_W)$ M_T fit (MeV/c^2)	$\sigma(M_W)$ p_T^e fit (MeV/c^2)	$\sigma(M_W)$ p_T^ν fit (MeV/c^2)
Statistical		140	190	260
Energy scale		160	160	160
Other systematic errors		165	180	305
EM energy resolution	$C=(1.5^{+0.6}_{-1.5})$	70	35	35
CDC z scale$^{(*)}$	$\alpha=(0.988\pm0.002)$	50	55	55
Hadronic energy resolution	$S_{\text{had}}=0.8\pm0.2$	65	5	80
Underlying event$^{(*)}$	$E_T^{\text{Tower}}=(16.8\pm1.5)$ MeV	35	35	35
Γ_W	$\Gamma_W=(2.1\pm0.1)$ GeV	20	20	20
Hadronic energy scale	$\alpha_{\text{had}}=(0.83\pm0.04)$	50	30	120
Number of minimum bias events	(1.0 ± 0.06)	60	10	150
QCD background	$(1.6\pm0.8)\%$	30	35	35
$Z\to ee$ background	$(0.43\pm0.05)\%$	15	20	20
Electron ID efficiency	parametrization	20	70	115
Radiative decays	$E_\gamma^{\text{min}},R_{e\gamma},\chi^2$	20	40	40
$p_T(W)$, pdf	$p_T(W)$ variation	65	130	130
Trigger efficiency	efficiency spread	20	20	60
Non-uniformity in η	test beam	10	10	25
Fitting error		5	10	10
Total		275	315	435

mass spectra which were generated for 21 different values of the W boson mass. The log-likelihood values for the different vector boson masses were fit to a parabola and the minimum was taken to be the fitted mass value. A decrease of half a unit in the log-likelihood was the one standard deviation statistical error. The likelihood distribution need not be Gaussian, depending on the range of the parameter fit, the intrinsic shape of the spectrum and the resolution function. The resulting log-likelihood curve was then non-quadratic. In addition, there will be fluctuations in the log-likelihood reflecting the Monte Carlo statistics. In order to determine the uncertainty, the fitting was redone with a cubic polynomial parametrization and the mass spacing was altered. This led to the assignment of 5 MeV/c^2 for the uncertainty due to the M_T fitting procedure.

M. Results of systematic errors

The systematic errors on the W boson mass as obtained from the transverse mass, electron transverse momentum and neutrino transverse momentum are summarized in Table XIV. The measured mass results from this analysis are

$$M_W(M_T)=80.350\pm0.140\pm0.165\pm0.160 \ \text{GeV}/c^2;$$

$$M_W(p_T^e)=80.300\pm0.190\pm0.180\pm0.160 \ \text{GeV}/c^2;$$

$$M_W(p_T^\nu)=80.045\pm0.260\pm0.305\pm0.160 \ \text{GeV}/c^2;$$

and from the transverse mass analysis,

$$M_W/M_Z=0.88114\pm0.00154\pm0.00181\pm0.00175.$$

In each result, the first uncertainty is due to statistics, the second is due to systematic effects, and the third is due to the electron energy scale determination.

VIII. CONSISTENCY CHECKS

To verify the stability of the W boson mass result, consistency checks have been performed in which the W boson mass is determined from various modified data samples. These samples include those in which the fitting window was varied, additional selection criteria were applied, and a different electron clustering algorithm was used. Fully overlapping data samples were used to check the consistency of the results obtained from fits to the p_T^e and p_T^ν spectra. Also, two-dimensional fits were done to check the consistency of parameters used in the Monte Carlo simulation.

In general, the data sample was reduced or enlarged in these consistency studies. There was a large overlap between the original data sample and the samples used to verify the result. In order to quantify this verification, define the mass from the original data sample M_W^{nom}, and that from the sample used in the verification M_W^{con}. Then the estimator of the independent statistical error on the difference in the two results that were used is $\sigma(M_W^{\text{nom}}-M_W^{\text{con}})=\sigma\sqrt{N_2/N_1}$. Here σ is the statistical error on the original data sample, consisting of N_1+N_2 events. The sample used for the consistency check contained N_1 events. This is the error that is quoted for the difference in mass for the consistency checks.

A. Additional selection and fitting criteria

To investigate the effect of multiple interactions, events were selected with low hit multiplicity and a narrow time

TABLE XV. Change in *W* mass from nominal for different subsamples of the data. Those subsamples for which the Monte Carlo templates were not modified are indicated by an asterisk*. Errors are statistical only.

Data subsample	ΔM_W (MeV/c^2)
One track in electron road[*]	-2 ± 54
One reconstructed event vertex[*]	-76 ± 76
Single interaction events[*]	-107 ± 95
$p_T^W < 10$ GeV/c	-166 ± 90

distribution in the small-angle scintillation counters (see Sec. II D). This yielded a sample in which approximately 77% were single interaction events. Also events with one and only one reconstructed event vertex and with only one track from the central detector in the electron road were selected. The latter cut removed mainly events with a random track from the underlying event. The change in fitted *W* boson mass from the transverse mass spectrum, with respect to the nominal mass value for each of these cross checks, is listed in Table XV. Note that the errors are statistical only. Any systematic error on the shifts is not included.

To test the event modeling, the p_T^W cut was tightened to 10 GeV/c and the result is listed in Table XV. When requiring p_T^W to be less than 10 GeV/c, there is an additional uncertainty due to the error on the hadronic energy scale factor and change in background contribution, which have not been included in the error estimate.

Another important check of the event modeling is testing both the sensitivity and consistency of the result by tracking the change in mass during the process of applying different cuts. As an example, the first column in Table XVI lists the change in *W* boson mass from the nominal fit when $u_{\parallel}$ in the data is required to be less than 10 GeV without modifying the templates. The change was rather dramatic for the mass from the p_T^{ν} spectrum. The second column lists the change in mass when the templates are made consistent with the data. Even though the *W* boson mass is rather sensitive to the cut on $u_{\parallel}$, the fitted masses agreed well with the nominal values when data and Monte Carlo were treated consistently, indicating that both the p_T^W scale and $u_{\parallel}$ efficiency were modeled correctly.

To check for any systematic bias in detector response, event samples were selected with different fiducial requirements. For *W* boson events the η range of the electron was restricted to electrons produced in the central region. For *Z*

TABLE XVI. Change in *W* mass from nominal when applying a cut on $u_{\parallel}$ of 10 GeV.

Fitted spectrum	ΔM_W (MeV/c^2) Data, no $u_{\parallel}$ cut MC, $u_{\parallel} < 10$ GeV	ΔM_W (MeV/c^2) Data, $u_{\parallel} < 10$ GeV MC, $u_{\parallel} < 10$ GeV
M_T	$+78$	-16
p_T^e	-280	$+40$
p_T^{ν}	$+810$	-45

TABLE XVII. The ratio of the *W* and *Z* boson masses when restricting the η range of the electron. The errors are the independent statistical errors with respect to the nominal fitted mass.

η range	$R = \dfrac{M_W}{M_Z}$
$|\eta^e| < 1.0$	1.0003 ± 0.0005
$|\eta^e| < 0.8$	1.0010 ± 0.0012
$|\eta^e| < 0.6$	1.0011 ± 0.0019

boson events the restriction was placed on only one of the two electrons, ensuring that a variation in detector response to the electron in *W* boson events was tracked in an identical manner in *Z* boson events. Table XVII lists the resultant change in the ratio of masses. The errors on the change were again statistical errors only. The ratio, tabulated in Table XVII, was with respect to the normalized ratio for the nominal η range. The ratio of masses did not change within errors. When the restriction was placed on both electrons in *Z* boson events, the ratio also did not change but had a large statistical uncertainty due to the significant loss of events.

The variation in mass was also tracked when the nominal fitting range in transverse mass was varied. Figure 43 shows the change in *W* boson mass when varying the lower and upper edge of the fitting window for the fit to the M_T distribution. Changing the fitting window led to a negligible systematic trend.

B. Modified electron clustering

Electron clusters were found by the reconstruction program using a nearest neighbor clustering algorithm [32]. The number of calorimeter towers included in the cluster was dynamic and depended on the environment of the electron. This algorithm thus introduced an uncertainty on the amount of underlying event energy included in the electron energy cluster, and therefore an uncertainty on how much energy was excluded from the underlying event for the calculation of the p_T^W. In the discussion in Sec. V C the energy assignments and the modeling of the underlying event are described using a window algorithm for the reconstruction of the electron energy. The corrections necessary to translate these results to the cluster algorithm then had to be dealt with properly. These ambiguities can be completely circumvented if a fixed electron definition is used. To verify the internal consistency, the *W* boson mass was also determined using a fixed size electron cluster.

The definition employed for the fixed size cluster is the "5×5 window algorithm." In this procedure, the electron energy was defined as the energy in the 25 towers in the region ± 0.2 in η and φ from the most energetic tower of the electron cluster as found by the nearest neighbor algorithm. Using the original $W \rightarrow e\nu$ data sample, the electron energies were recalculated using the 5×5 window algorithm and the p_T^W was calculated with respect to the electron vertex, excluding the 5×5 window occupied by the electron. The region excluded from the underlying event for the calculation of the $\rlap{/}E_T$ was thus exactly known for each event. Subjecting
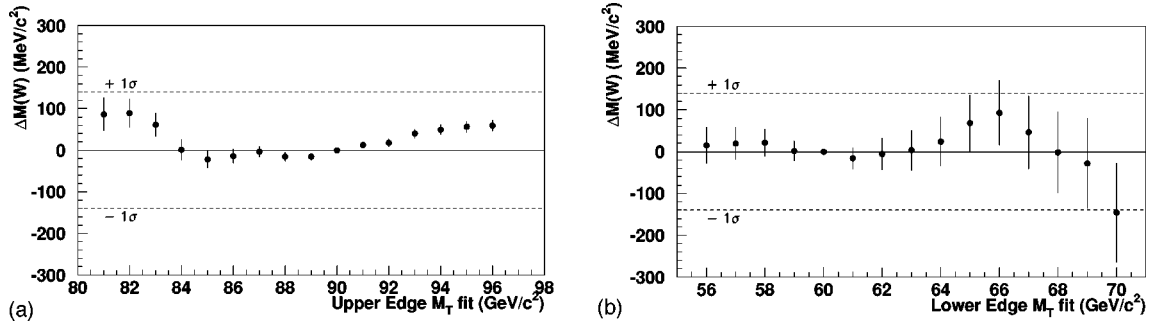
FIG. 43. Change in fitted *W* boson mass when varying the (a) upper and (b) lower edge of the fitting window from the fit to the transverse mass spectrum (points). The horizontal bands indicate the 1σ statistical error on the nominal fit.

these events to the standard event selection criteria yielded 7167 events, 7131 of which were in the nominal data sample. The fitted *W* boson mass obtained from this data sample, using the window algorithm to define the electron, was 12 MeV/c^2 lower than when using the nearest neighbor algorithm. As noted above, a systematic uncertainty on the *W* boson mass of 20 MeV/c^2 has been attributed due to the difference in these two approaches and has been included in the underlying event uncertainty in Table XIV.

C. Fully overlapping data samples

The nominal fits to obtain the *W* boson mass were performed using events within a certain range either in transverse mass or in transverse momentum. These event samples did not fully overlap. Fully overlapping event samples are obtained when applying a fitting window in one variable and then utilizing the full unrestricted spectra in the other two variables, using all events in this window. Figure 44 shows the p_T^e and p_T^ν spectra with only the requirement that $60 < M_T < 90$ GeV/c^2. The change in *W* boson mass obtained from a fit to these spectra is $+84 \pm 55$ MeV/c^2 from the fit to the p_T^e spectrum and $+54 \pm 81$ MeV/c^2 from fitting the p_T^ν

spectrum. The errors on the shift in mass are the statistical errors due to the different number of events fit. Again, the results are consistent with the nominal results for the fits to the transverse momentum spectra.

D. Two-dimensional fits

Two-dimensional fits were carried out to check the stability and correctness of parameters used in the Monte Carlo simulation. The first two-dimensional fit was performed on the *W* boson mass and the constant term in the electron energy resolution. Rather than expressing the likelihood in terms of the constant term, which resulted in a very asymmetric likelihood distribution, it was expressed in terms of the energy resolution at an electron p_T of 40 GeV/c

$$\mathcal{R}_{40} \equiv \sqrt{C^2 + \frac{S^2}{40}} \qquad (55)$$

where S and C are the coefficients of the sampling and constant term, respectively. The sampling term was taken to be 0.13 and the constant term is varied. The error matrix for the fit in M_W and $\mathcal{R}_{40}$ is:
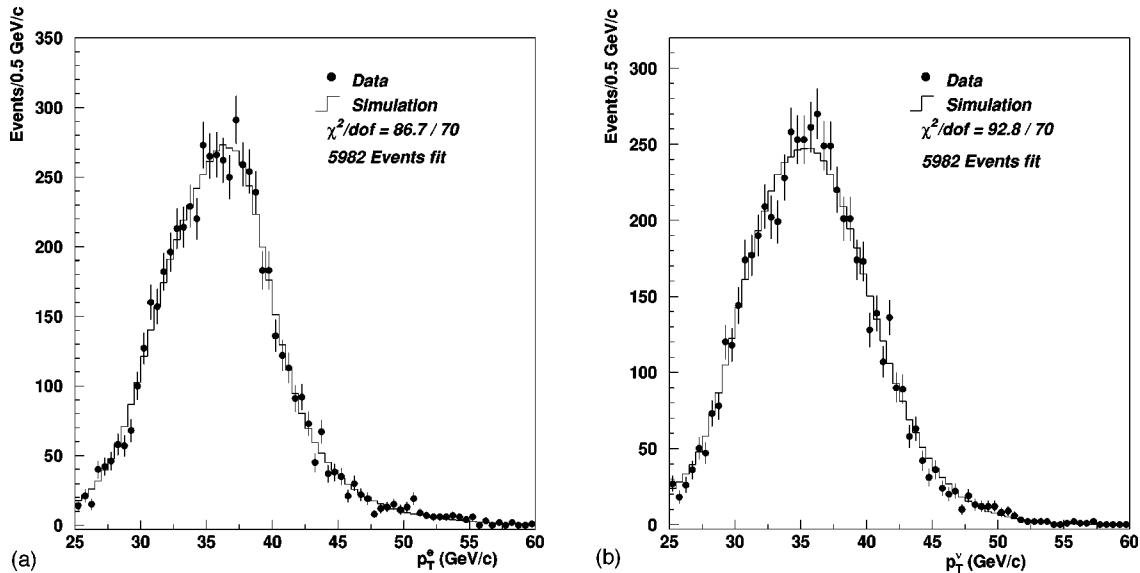
FIG. 44. The (a) electron and (b) neutrino transverse momentum distribution for the events in the transverse mass window $60 < M_T < 90$ GeV/c^2 (points). The histograms are the best fits of the simulation.
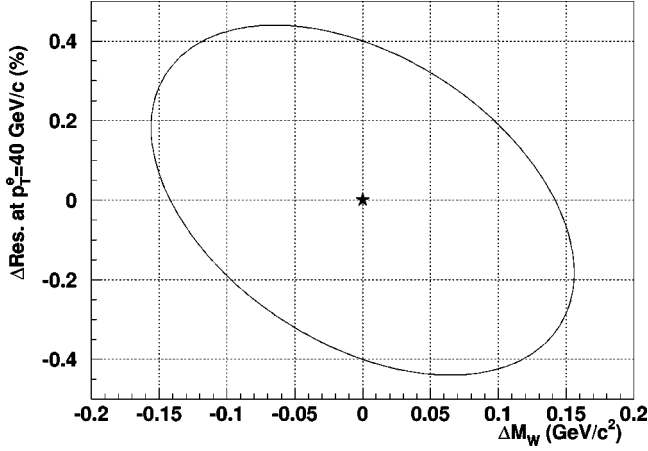
FIG. 45. The 1σ contour in the change in M_W and the electron energy resolution at $p_T^e = 40$ GeV/c from fits of the simulation, in which the constant term is allowed to vary, to W boson events.

$$\begin{pmatrix} 0.0243 & -0.0286 \\ -0.0286 & 0.1933 \end{pmatrix} \tag{56}$$

with a correlation coefficient of $\rho = -0.4155$. Figure 45 shows the contour in M_W and $\mathcal{R}_{40}$ for a change of 0.5 units in the log-likelihood. The values on the axes are with respect to the central value of the fit. The fitted W boson mass was higher by 26 MeV/c^2 compared to the value obtained when the constant term in the energy resolution was fixed at 1.5%, in agreement with the nominal fit. The error on the mass from the two-dimensional fit was 156 MeV/c^2. For a fixed value of the constant term the error would be $0.156\sqrt{1-\rho^2}$ $= 142$ MeV/c^2, consistent with the nominal fit result. The fitted value for the resolution [see Fig. 46(a)] was $\mathcal{R}_{40}$ $= (2.34 \pm 0.440)\%$ which, assuming a sampling term of S $= 0.13$, corresponded to a constant term of $C = (1.1^{+0.8}_{-1.1})\%$. This is again consistent with the result obtained from fitting the width of the Z boson resonance from which the constraint on the resolution is actually slightly tighter. The correlation between the W boson mass and $\mathcal{R}_{40}$ was given by $\rho[\sigma(M_W)/\sigma(\mathcal{R}_{40})] = -147$ MeV/c^2 per 1% change in $\mathcal{R}_{40}$, which was also consistent within errors with the result obtained in Sec. VII C and shown in Fig. 46(b).

A two-dimensional fit was also performed in mass and hadronic energy scale factor κ. The error matrix for this fit in M_W and κ is

$$\begin{pmatrix} 0.0250 & 0.0043 \\ 0.0043 & 0.003121 \end{pmatrix} \tag{57}$$

with a correlation coefficient of $\rho = 0.457$. Figure 47 shows the one σ contour in M_W and κ. The values on the axes are with respect to the central value of the fit. The fitted W boson mass was lower by 7 MeV/c^2 compared to the value obtained when the p_T^W scale was fixed at 0.83, in agreement with the nominal fit. The error on the mass from the two-dimensional fit is consistent with the nominal fit keeping the hadronic energy scale factor fixed. The fitted value for the hadronic energy scale factor was $\kappa = 0.834 \pm 0.056$, consis-
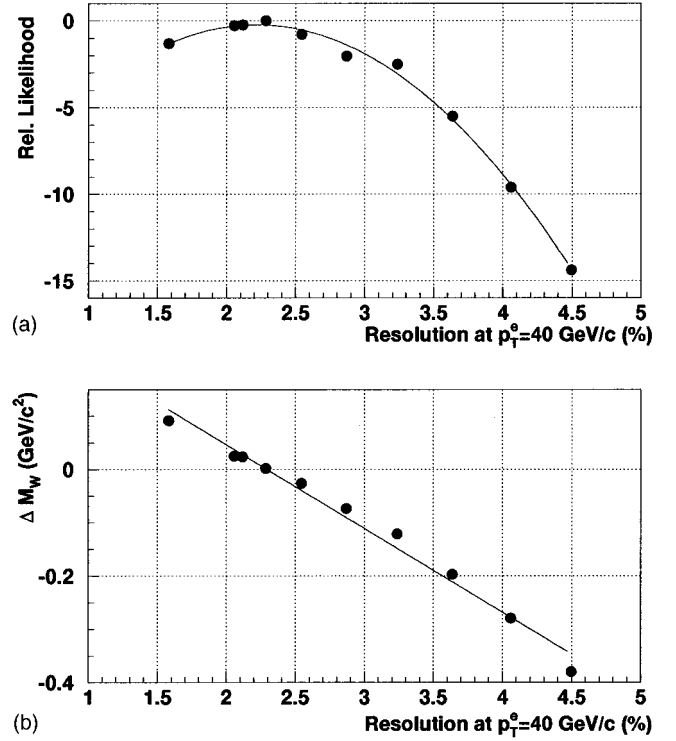
FIG. 46. From fits of the simulation, in which the constant term is allowed to vary, to W events: (a) The relative likelihood versus the electron energy resolution at $p_T^e = 40$ GeV/c. (b) The change in the fitted W mass versus the electron energy resolution at $p_T^e = 40$ GeV/c.

tent with the result obtained from the Z boson data. The error is large because the W boson mass was not very sensitive to the hadronic energy scale. The correlation between the W boson mass and κ is given by $\rho[\sigma(M_W)/\sigma(\kappa)] = 12.8$ MeV/c^2 per 1% change in scale factor. This is to be compared to the sensitivity of 12.1 MeV/c^2 per 1% change in scale factor obtained in Sec. IV B.

In conclusion, the mass values obtained for different subsamples of the nominal data sample were all consistent
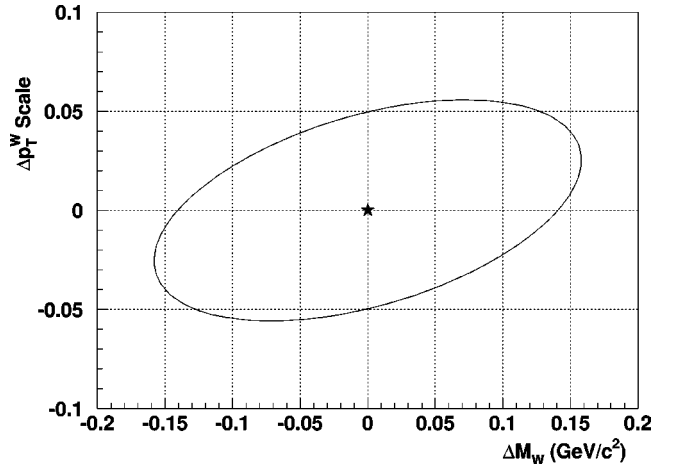
FIG. 47. The 1σ contour in the change in M_W and p_T^W scale from fits of the simulation, in which the p_T^W scale factor is allowed to vary, to W boson events.

within the quoted statistical uncertainty. Moreover, when leaving crucial parameters in the event modeling as free parameters in the fit, the *W* boson data preferred values for these parameters which were completely consistent with those obtained from external constraints, a strong indication of the stability of the result.

IX. CONCLUSION

A measurement of the *W* boson mass determined from the transverse mass distribution using electrons in the central region of the D∅ detector from the 1992–1993 Fermilab Tevatron running in 12.8 pb^{-1} has been described. The determination of M_W was based on a ratio of the measured *W* boson and *Z* boson masses, normalized to the world average *Z* boson mass as determined by the LEP experiments. This measurement yielded a *W* boson mass value of

$$M_W = 80.350 \pm 0.140 \pm 0.165 \pm 0.160 \text{ GeV}/c^2$$

and has an uncertainty comparable to that of other recent measurements in a single channel. The first uncertainty is due to statistics, the second is due to systematic effects, and the third is due to the electron energy scale determination. The 160 MeV/c^2 uncertainty due to the uncertainty on the absolute energy scale has a contribution of 150 MeV/c^2 due to the limited *Z* boson statistics. The measured ratio of the *W* boson and *Z* boson masses is

$$M_W/M_Z = 0.88114 \pm 0.00154 \pm 0.00181 \pm 0.00175.$$

Here, the first uncertainty is due to statistics, the second is due to systematic effects, and the third is due to the electron energy scale determination.

Based on this measurement alone, the values for Δr and Δr_{res}, as defined in Eqs. (7), (8), were determined to be

$$\Delta r = 0.0372 \pm 0.0160 \text{ and}$$

$$\Delta r_{\text{res}} = -0.0236 \pm 0.0170.$$

This measurement alone is thus sensitive to quantum corrections in the standard model at the 2.3σ level with evidence for bosonic radiative corrections with a significance of 1.4σ.

An average *W* boson mass can be determined by combining the current result with recent previous measurements. The measurements are weighted with their uncorrelated uncertainties. The correlated uncertainty for the most recent measurements is that due to proton structure as parametrized in global parton distribution function fits. For each measurement, the uncertainty due to the common effect is removed to determine the uncorrelated error. Based on the UA2 [12] and most recent CDF publication [15], the common uncertainty is taken to be 85 MeV/c^2, the largest of the individual uncertainties due to the uncertainty on the structure of the proton. This procedure then yields a world average *W* boson mass of $M_W = 80.34 \pm 0.15$ GeV/c^2.

Figure 48 (top) presents a comparison of the world's direct determinations of M_W including this measurement and the overall $p\bar{p}$ world average. Also shown (band) is the stan-

dard model prediction using the LEP data as calculated by the LEP Electroweak Working Group [19]. Figure 48 (bottom) shows the recently measured top quark mass [1] from the D∅ Collaboration versus the world average *W* mass. The top quark mass value used is

$$m_t(\text{D0}) = 172.0 \pm 5.1(\text{stat}) \pm 5.5(\text{syst}) \text{ GeV}/c^2 \quad (58)$$

which is from the combined measurement of the dilepton and lepton plus jets channels. The standard model prediction for different values of the Higgs mass [54] is also shown as the shaded bands.

Using the world average *W* boson mass, the derived values for the quantum corrections in the SM are

$$\Delta r = 0.03834 \pm 0.00885 \text{ and}$$

$$\Delta r_{\text{res}} = -0.0224 \pm 0.00944.$$

The direct measurement of the *W* boson mass at $p\bar{p}$ colliders indicates the existence of radiative corrections in the standard model at the $\sim 4.3\sigma$ level and evidence of bosonic radiative corrections at the $\sim 2.4\sigma$ level.

ACKNOWLEDGMENTS

APPENDIX A: *W* AND *Z* BOSON PRODUCTION MODEL

The theory and phenomenology of production of *W* and *Z* bosons can be divided into three regions of the p_T of the vector boson. These regions are imprecisely ordered as follows:

(1) The high-p_T region in which perturbation theory is expected to be valid. This region is roughly 50 GeV/c and above.

(2) The low-p_T region where perturbation theory is not helpful and soft gluons are freely emitted. There is a model for this process, and the validity of this theory is roughly below 15 GeV/c. By far, the bulk of the cross section for *W* boson and *Z* boson production is in this region.

(3) The intermediate region for which there is no theoretical description. Some analyses attempt to smoothly connect the two regions, beyond that which occurs naturally by simply adding the cross sections from region 1 to those of region 2.

The Monte Carlo generation of the vector bosons relied on the resummation formalism of Collins, Soper, and Sterman (CSS) [39] which treats the emission of soft gluons in region 2 by summing all contributions in impact parameter
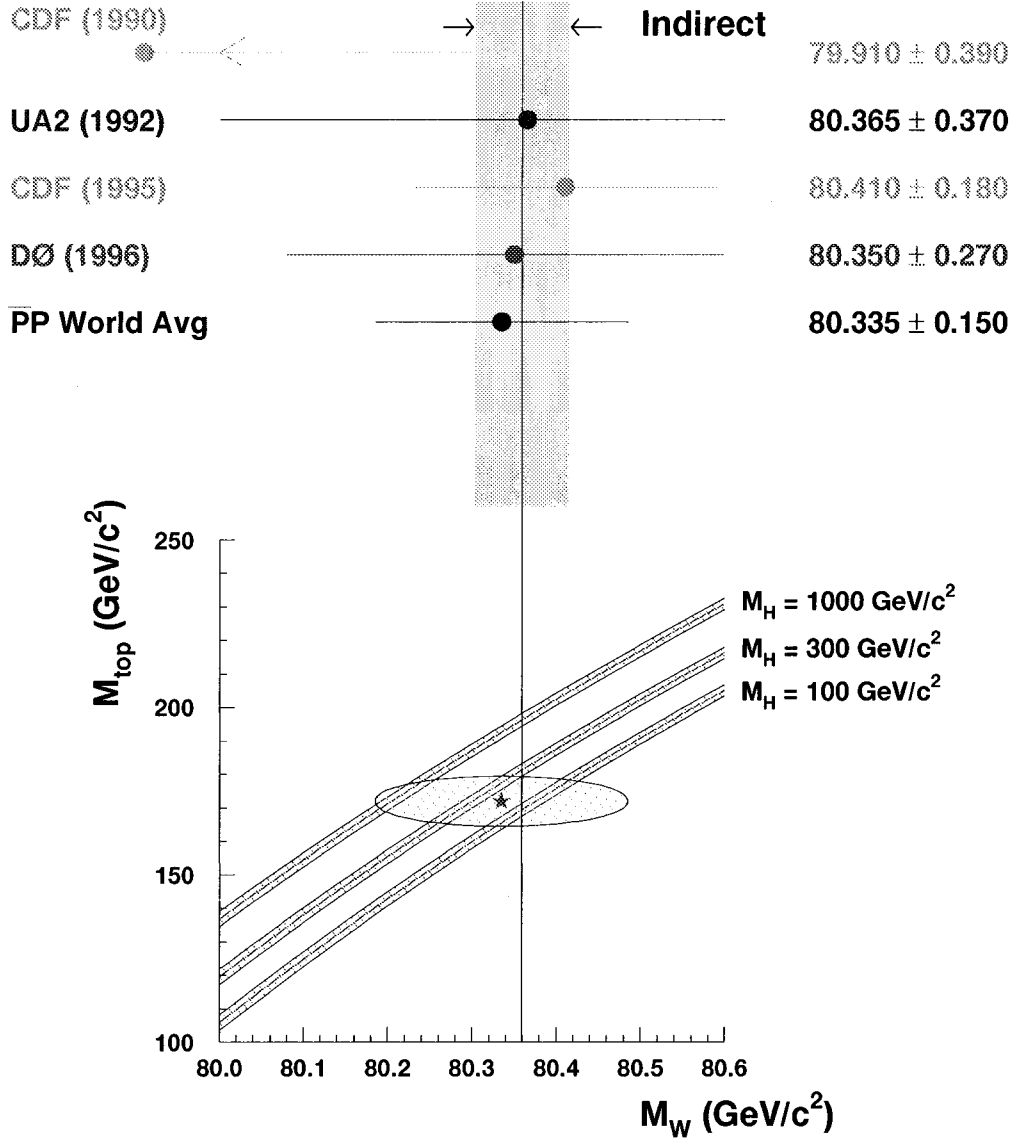
FIG. 48. The upper half of the figure shows the DØ determination of M_W along with recent results from other hadron collider experiments and the $p\bar{p}$ world average (see the text for a discussion of the world average calculation). The band is the standard model prediction from the combined LEP results. The lower half of the figure shows the DØ determination of the mass of the top quark versus the world average determination of M_W ($\star$). The contour shows the allowed range in each value. The standard model prediction (see the text) for various assumptions of the Higgs boson mass is indicated by the bands.

space. There are few free parameters in this model and it is shown below that it satisfactorily matches the DØ data. The triple differential cross section for production of a W boson can be written

$$\frac{d\sigma(AB \rightarrow W)}{dp_T^2 dy dQ^2} = \frac{\pi}{s} \sigma_0 \delta(Q^2 - M_W^2) \frac{1}{(2\pi)^2} \int d^2\vec{b} e^{i\vec{p}_T \cdot \vec{b}}$$

$$\times \sum_{ij} \widetilde{W}_{ij}(b^*, Q, x_A, x_B) e^{-S(b^*, Q)}$$

$$\times F_{ij}^{NP}(b, Q, Q_0, x_A, x_B)$$

$$+ Y(p_T, Q, x_A, x_B). \qquad \text{(A1)}$$

Here, $\widetilde{W}_{ij}(b^*, Q, x_A, x_B)$ includes the convolution of parton densities for partons i, j and the splitting functions, the Cabibbo-Kobayashi-Maskawa elements, and the electroweak parameters. The quantity Q is the invariant mass of the annihilating partons, while $x_{A,B}$ is the Bjorken x variable representing the fraction of the colliding hadron's momenta carried by the annihilating partons. Q_0 is taken to be the lowest scale where perturbation theory is presumed to be sensible. The quantity σ_0 is for normalization. The Sudakov form factor $S(b, Q)$ is fixed by the order in α_s and is an integral over a running scale. The combination of these terms describe region 2. The quantity $Y(p_T, Q, x_A, x_B)$ contains terms which are less singular than p_T^{-2} and is the term which dominates in the perturbative regime, region 1.
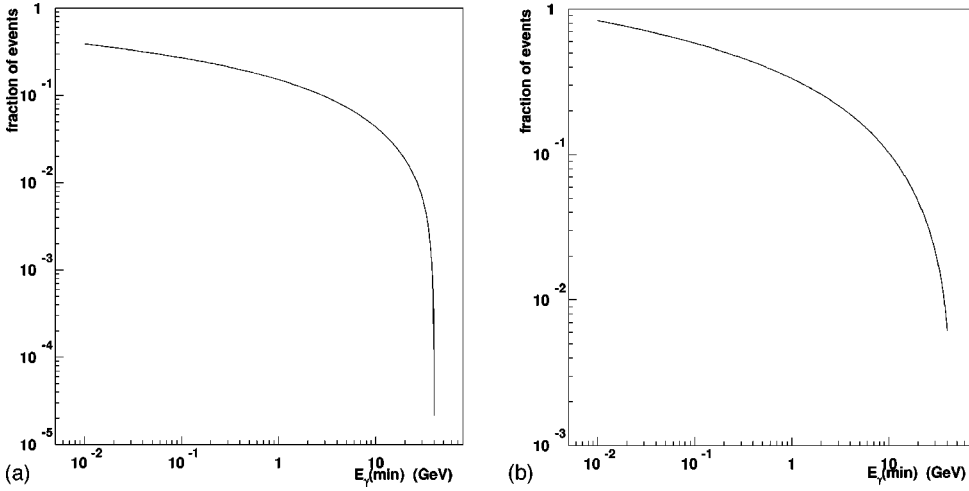
FIG. 49. Fraction of radiative (a) *W* decays and (b) *Z* decays as function of the minimum photon energy.

The complication inherent in this formalism is the Fourier transformation of the cross section, which involves an integral over all values of the impact parameter b. This is dealt with by regulating b to behave well near the origin, forcing it to tend to a constant as $b \rightarrow 0$. In the CSS formalism, this amounts to a replacement of $b \rightarrow b* \equiv b/\sqrt{1 + b^2/b_{max}^2}$. The price for making this modification is the obligation to add a term to ''replace'' the missing contribution to the integral from this $b \rightarrow b*$ substitution. This extra factor is the so-called non-perturbative function, represented in Eq. (A1) as F_{ij}^{NP}. Theoretical arguments fix the form of F_{ij}^{NP}, up to phenomenological parameters.

There have been two efforts to determine the non-perturbative function. One such recent fit is by Ladinsky and Yuan [43] (LY) who parametrized the non-perturbative function as

$$F_{ij}^{NP}(b,Q,Q_0,x_A,x_B) = \exp\left[-b^2 g_1 - g_2 b^2 \ln\left(\frac{Q}{2Q_0}\right)\right.$$
$$\left. - g_1 g_3 b \ln(100 x_A x_B)\right]. \quad \text{(A2)}$$

The g parameters are not specified by theory, but are measurable. A much earlier effort by Davies and Stirling [42] (DS) used an identical parametrization, but essentially with $g_3 = 0$. Recently, Arnold and Kaufman [40] (AK) employed the CSS formalism including the DS fits, a NLO calculation for the *Y* term [41] (region 1), and a strategy of dealing with region 3. A computer program has been available for the AK approach. Likewise, the LY calculation was done with an independent computer program which is identical in its coding of the CSS theory, but utilized a simple $\mathcal{O}(\alpha_S)$ calculation for the *Y* term. LY made no attempt to match the two regions. Both computer codes have been used in this analysis.

This description of *W* boson and *Z* boson production is taken as the *ansatz* for the Monte Carlo production model. The more recent LY fits to modern Drell-Yan and collider *Z* boson data constrain the *g* parameters and have been used here as representative of the best available information. In this sense the *g* parameters function operationally like the parton distribution functions. The LY fits result in $g_1 = 0.11_{-0.03}^{+0.04}$ GeV^2, $g_2 = 0.58_{-0.20}^{+0.10}$ GeV^2, and $g_3 = -1.5 \pm 0.10$ GeV^{-1}. These central values have been used as the nominal production model for *W* and *Z* bosons, with the major sensitivity to g_2.

APPENDIX B: BREMSSTRAHLUNG

The fraction of decays which involves radiation depends on the minimum photon energy, E_γ^{min}, which was taken to be 50 MeV. Figure 49 shows this fraction as function of E_γ^{min} for (a) *W* boson and (b) *Z* boson decays. For *Z* boson decays the fraction of radiative decays is about a factor of two higher than for *W* boson decays, as expected. For the default E_γ^{min}, 31% of the *W* boson decays and 66% of the *Z* boson decays were radiative. Only order α_{EM} corrections have been included and so processes in which two or more photons are radiated were not generated.

For radiative *W* boson decays, $W \rightarrow e \nu \gamma$, it is important to determine the minimum spatial separation between the photon and electron that would result in the photon energy not being included with that of the electron by the reconstruction program. For events with $R = \sqrt{\Delta \eta^2 + \Delta \varphi^2}$ above approximately 0.2 the photon energy may not be added to that of the electron. Instead, it was reconstructed as part of the *W* boson recoil. The neutrino energy was unchanged, but the electron energy is too low. The *W* boson and *Z* boson masses were then too low in a manner which does not cancel in the ratio. Since this effect is large, it is important to evaluate the effect when the photon is produced by bremsstrahlung in the central detector.

For the photon to have an effect on the measured *W* boson mass, it must be separated from the electron in (η, φ) space by at least $R_{e\gamma} = 0.2$, that is,

$$\Delta \eta^2 + \Delta \varphi^2 > R_{e\gamma}^2. \quad \text{(B1)}$$

With $\Delta \eta = \Delta \vartheta / \sin \vartheta = \cosh \eta \Delta \vartheta$, this can be written as

$$\left(\frac{\Delta \vartheta}{\sin \vartheta}\right)^2 + \Delta \varphi^2 > R_{e\gamma}^2. \quad \text{(B2)}$$
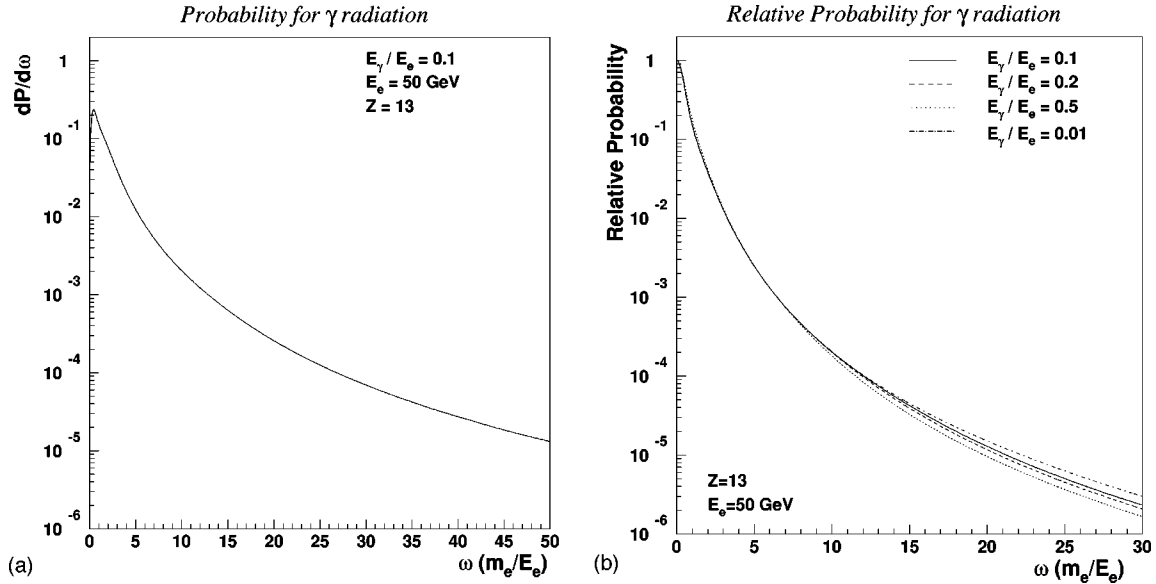
FIG. 50. (a) Probability for an electron to radiate a photon in aluminum ($Z=13$) as a function of the angle ω between the electron and the photon in units of m_e/E, where m_e is the electron mass and E its energy. (b) Relative probability for radiating a photon for different values of $y=k/E$, with k the photon energy.

Switching to coordinates measured with respect to the electron

$$\Delta\vartheta = \omega\cos\alpha \qquad (B3)$$

$$\Delta\varphi = \frac{\omega\sin\alpha}{\sin\vartheta}, \qquad (B4)$$

where ω is the angle between the electron and the photon and α the azimuthal angle of the photon with respect to the electron, one can write

$$(\omega\cos\alpha)^2 + (\omega\sin\alpha)^2 > \left(\frac{R_{e\gamma}}{\cosh\eta}\right)^2 \qquad (B5)$$

or

$$\omega > \frac{R_{e\gamma}}{\cosh\eta}. \qquad (B6)$$

The angle between the electron and photon must be greater than 0.2 rad for $\eta=0$ and greater than 0.13 rad for $\eta=1$. In units of m_e/E, where m_e is the electron mass and E the electron energy, this corresponds to $E/m_e \times \omega > 13,000$ for an electron energy E of 50 GeV and $\eta=1$.

Figure 50(a) shows the probability $dP/d\omega$ for radiating a photon at an angle ω for the case $y=0.1$, where y is the fraction of the electron's energy carried by the photon [53]. The angle ω is expressed in units of m_e/E. For all calculations in this analysis, $Z=13$ (aluminum) has been assumed and the energy of the electron has been fixed to $E=50$ GeV. The probability decreases by four orders of magnitude at m_e/E-scaled angles of 50. Figure 50(b) shows the relative probability for radiating a photon at an angle ω and its dependence on y. Although the probability for radiating a photon is larger at small y, after normalization, there is little y

dependence of the angle at which the photon is radiated. Since scaled angles of 13,000 or more are needed, the photon never separates from the electron by radiation alone and therefore bremsstrahlung has no effect on the W boson mass.

The electron and photon can also separate if the electron scatters through a large angle. The probability that an electron radiates a photon of momentum between k and $k+dk$ in dx in a medium with radiation length X_0 is [53,48]

$$P(E,k)dkdx = \frac{dx}{X_0}\frac{dk}{k}\left(\frac{4}{3} - \frac{4}{3}y + y^2\right). \qquad (B7)$$

The quantity y is the fraction of the electron's energy carried by the photon, $y=k/E$, and E and k are the electron and photon energies. Integrating from $k=k_{min}$ to E one finds

$$P(E,k>k_{min})dx$$

$$= \frac{dx}{X_0}\left[-\frac{4}{3}(\ln y_{min}+1-y_{min})+\frac{1}{2}(1-y_{min}^2)\right]dx. \qquad (B8)$$

For y_{min} close to 1 this gives

$$P(E,k>k_{min})dx = \frac{dx}{X_0}\left(\zeta+\frac{1}{6}\zeta^2\right)dx \qquad (B9)$$

with $\zeta \equiv 1-y_{min}$. For example, the probability that a 50 GeV electron radiates a 49 GeV photon in $0.15X_0$ is

$$0.15\times 0.02 \approx 3\times 10^{-3}. \qquad (B10)$$

The 1 GeV electron can then scatter through a large angle [18]

$$\omega_{rms} = \sqrt{2}\times\frac{13.6\ \text{MeV}}{1\ \text{GeV}}\times\sqrt{0.15} = 7.4\ \text{mrad}. \qquad (B11)$$
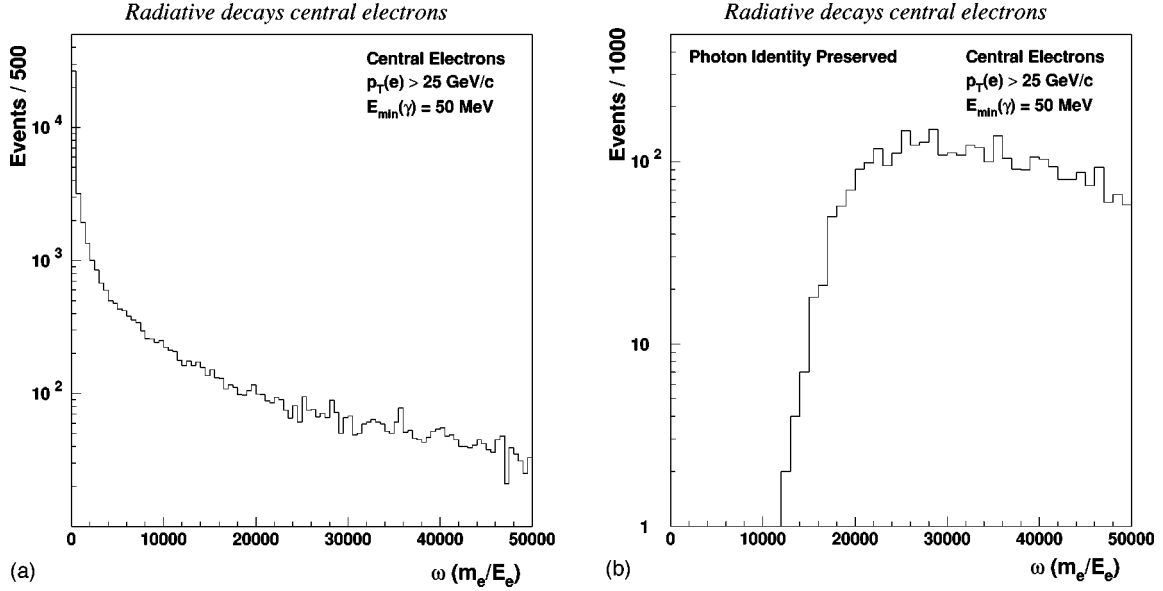
FIG. 51. Distribution in ω, in units of m_e/E, for radiative W boson events in the central calorimeter and (b) for events where the photon retains its identity.

The angles resulting from multiple scattering are generally larger than those produced in the radiation itself, particularly when the electron is low in energy ($\omega_{\rm rms} \approx 1/E$). Nevertheless, it is still difficult to separate the photon and electron sufficiently. The 7.4 mrad angle calculated above translates, in units of m_e/E, into $E/m \times 7.4 \times 10^{-3} \approx 800$, still small compared to 13,000. The falloff in scattering is rapid (Gaussian). If one considers a 50 GeV electron radiating 99.8% of its energy, the probability becomes small, 3×10^{-4}. The resulting 100 MeV electron, however, can now multiple scatter through a large angle, 80 mrad or 8000 in units of m_e/E.

This situation is compared with radiative W boson decays in Fig. 51(a) which shows the distribution in ω, in units of m_e/E, for radiative W boson events with the electron in the central calorimeter with $p_T^e > 25$ GeV/c. The distribution has a very long tail extending to values of 50,000 for ω. At small angles of $E/m_e \times \omega = 10,000$ the cross section is down by a factor of approximately 200. Nevertheless, 21% of the events have angles greater than 5000. Figure 51(b) shows the event distribution in ω for events in which the photon and electron reconstruct as separate entities with the photon retaining its identity. As was estimated above, the threshold at $E/m_e \times \omega$ is approximately 15,000.

APPENDIX C: MEAN NUMBER OF INTERACTIONS

The library of minimum bias events was stored in bins of luminosity according to the following rule. Given a W boson event, recorded at a luminosity $\mathcal{L}$ with corresponding average number of interactions per crossing $\langle n \rangle$, the minimum bias event, mimicking the underlying event, was taken at a scaled value of the instantaneous luminosity, $\mathcal{L}'$. $\mathcal{L}$ was chosen so that the mean multiple interaction rate in Monte Carlo generated W boson events is the same as in the W boson data sample.

The probability of getting a W boson trigger in a crossing

in which there are n interactions is given by

$$P(W,n) = nP(n) \frac{\sigma_W}{\sigma_{\rm inel}}. \tag{C1}$$

Here $P(n)$ is the Poisson probability of n interactions in the crossing, $\sigma_W/\sigma_{\rm inel}$ the probability that the inelastic interaction is one in which a W boson is produced. The factor n represents the number of ways one can choose the W boson interaction from the n interactions in the crossing. Note that the probability of getting a W boson in a crossing is then

$$P(W) = \sum_n nP(n) \frac{\sigma_W}{\sigma_{\rm inel}} = \langle n \rangle \frac{\sigma_W}{\sigma_{\rm inel}}, \tag{C2}$$

which is the expected rate when $\langle n \rangle$ is written in terms of the luminosity and the inelastic cross section, σ_{inel}. The probability distribution of getting n interactions in a crossing in which there is a W boson is

$$P(n|W) = nP(n), \tag{C3}$$

and has a mean value of $\langle n \rangle + 1$. This shows that the mean number of interactions in a crossing in which there is a W is $\langle n \rangle + 1$.

For the minimum bias trigger, the average number of interactions per crossing $\langle n_{min} \rangle$ given that there is at least one, is

$$\langle n_{min} \rangle = \frac{\sum_{n'=0}^{\infty} n' P(n')}{\sum_{n'=1}^{\infty} P(n')} = \frac{\langle n' \rangle}{1 - e^{-\langle n' \rangle}}. \tag{C4}$$

The minimum bias events are chosen at a luminosity $\mathcal{L}'$ such that the mean $\langle n_{min} \rangle$, as given by equation C4, is equal to $\langle n \rangle + 1$, where $\langle n \rangle$ is the mean number of interactions at

luminosity $\mathcal{L}$ at which the W event was recorded. This guaranteed that the mean number of interactions was correct. The distributions in the number of interactions per crossing are somewhat different, though. The minimum bias distribution is a Poisson distribution, cut off at $n = 1$, while the number of interactions in W events is a Poisson distribution, beginning at $n = 1$. The impact of this difference in this analysis is negligible.

[1] DØ Collaboration, S. Abachi *et al.*, Phys. Rev. Lett. **74**, 2632 (1995); S. Abachi *et al.*, *ibid.* **79**, 1197 (1997); B. Abbott *et al.*, *ibid.* **80**, 2063 (1998).

[2] CDF Collaboration, F. Abe *et al.*, Phys. Rev. Lett. **74**, 2626 (1995).

[3] S. Weinberg, Phys. Rev. Lett. **19**, 1264 (1967); A. Salam, in *Elementary Particle Theory: Relativistic Groups and Analyticity (Nobel Symposium No. 8)*, edited by N. Svartholm (Almqvist and Wiksell, Sweden, 1968), p. 367; S. L. Glashow, Nucl. Phys. **22**, 579 (1961).

[4] DØ Collaboration, S. Abachi *et al.*, Phys. Rev. Lett. **77**, 3309 (1996).

[5] UA1 Collaboration, G. Arnison *et al.*, Phys. Lett. **122B**, 103 (1983).

[6] UA2 Collaboration, M. Banner *et al.*, Phys. Lett. **122B**, 476 (1983).

[7] UA1 Collaboration, G. Arnison *et al.*, Phys. Lett. **126B**, 398 (1983); UA2 Collaboration, M. Banner *et al.*, *ibid.* **129B**, 130 (1983).

[8] UA1 Collaboration, G. Arnison *et al.*, Europhys. Lett. **1**, 327 (1986).

[9] UA2 Collaboration, R. Ansari *et al.*, Phys. Lett. B **186**, 440 (1987).

[10] UA1 Collaboration, C. Albajar *et al.*, Z. Phys. C **44**, 15 (1989).

[11] UA2 Collaboration, J. Alitti *et al.*, Phys. Lett. B **241**, 150 (1990).

[12] UA2 Collaboration, J. Alitti *et al.*, Phys. Lett. B **276**, 354 (1992).

[13] CDF Collaboration, F. Abe *et al.*, Phys. Rev. Lett. **62**, 1005 (1989).

[14] CDF Collaboration, F. Abe *et al.*, Phys. Rev. Lett. **65**, 2243 (1990); Phys. Rev. D **43**, 2070 (1991).

[15] CDF Collaboration, F. Abe *et al.*, Phys. Rev. Lett. **75**, 11 (1995); Phys. Rev. D **52**, 4784 (1995).

[16] UA1 Collaboration, G. Arnison *et al.*, Phys. Lett. **134B**, 469 (1984).

[17] Here, natural units in which $\hbar = c = 1$ are used, except for units of momentum (GeV/c) and mass (GeV/c^2).

[18] R. M. Barnett *et al.*, Phys. Rev. D **54**, 1 (1996).

[19] CERN-PPE/95-172, LEP Electroweak Working Group, 1995.

[20] A. Sirlin, Phys. Rev. D **22**, 971 (1980); W. Marciano and A. Sirlin, *ibid.* **22**, 2695 (1980).

[21] P. Gambino and A. Sirlin, Phys. Rev. D **49**, 1160 (1994).

[22] M. L. Swartz, Phys. Rev. D **53**, 5268 (1996); A. D. Martin and D. Zeppenfeld, Phys. Lett. B **345**, 558 (1995); S. Eidelmann and F. Jegerlehner, Z. Phys. B **67**, 585 (1995); H. Burkhardt and B. Pietrzyk, Phys. Lett. B **356**, 398 (1995).

[23] J. Smith, W. L. van Neerven, and J. A. M. Vermaseren, Phys. Rev. Lett. **50**, 1738 (1983); V. Barger, A. D. Martin, and R. J. N. Phillips, Z. Phys. C **21**, 99 (1983).

[24] For the light leptons, momenta will be equated with energies. Transverse energy will then sometimes appear as a vector, $\vec{E}_T$.

[25] The effect of the width is to reduce the height and smear the distribution slightly to the high side of the peak. The transverse motion of the W boson reduces the height of the peak and smears the shape toward the low M_T side; p_T^W will not significantly affect the high edge of the spectrum.

[26] DØ Collaboration, S. Abachi *et al.*, Nucl. Instrum. Methods Phys. Res. A **338**, 185 (1994).

[27] DØ Collaboration, S. Abachi *et al.*, Phys. Rev. D **52**, 4877 (1995).

[28] The coordinate system in DØ is right-handed, with the $+z$ axis pointing in the direction of the proton beam (south); the $+x$ axis horizontal, with the positive direction away from the center of the accelerator; and the $+y$ axis, up. The origin of this coordinate system is centered at the midpoint of the detector where the nominal beam intersection would occur. Radial directions are measured from that point. Polar angles θ are measured with respect to the $+z$ axis, and azimuthal angles, ϕ, are measured with respect to the $+x$ axis. Pseudorapidity is defined as $\eta = -\ln\tan(\theta/2)$ where θ is the polar angle with respect to the proton beam.

[29] Particle Data Group, L. Montanet *et al.*, Phys. Rev. D **50**, 1173 (1994).

[30] R. D. Schamberger, *Proceedings of the Fifth International Conference on Calorimetry in High Energy Physics*, Upton, New York, 1994, edited by Howard Gordon and Doris Rueger (World Scientific, Singapore, 1994); J. Kotcher, in *Proceedings of the 1994 Beijing Calorimetry Symposium*, Beijing, China, 1994, p. 144; J. A. Guida, in *Proceedings of the 4th International Conference on Advanced Technology and Particle Physics*, Como, Italy, 1994 [Nucl. Phys. B (Proc. Suppl.) **44**, 158 (1995)].

[31] Qiang Zhu, Ph.D. thesis, New York University, 1994.

[32] S. Youssef, Comput. Phys. Commun. **45**, 423 (1987).

[33] F. Carminati *et al.*, GEANT User's Guide, CERN Program Library (1991), unpublished.

[34] The top quark analysis published in Ref. [27] cut this quantity at $\sigma_{trk} < 5$ which was 94% efficient.

[35] T. C. Awes, F. E. Obenshain, F. Plasil, S. Saini, S. P. Soerensen, and G. R. Young, Nucl. Instrum. Methods Phys. Res. A **311**, 130 (1992).

[36] Q. Zhu, in *Proceedings of 9th Topical Workshop on Proton-Antiproton Collider Physics*, edited by T. Kondo and S. Kim (Universal Academy Press, Tokyo, 1994), p. 65.

[37] F. Paige and S. D. Protopopescu, ISAJET Monte Carlo version 6.22, BNL Report No. BNL38034, 1986 (unpublished).

[38] DØ Collaboration, S. Abachi *et al.*, Phys. Rev. Lett. **75**, 1456 (1995).

[39] J. Collins and D. Soper, Nucl. Phys. **B193**, 381 (1981); **B213**,

545(E) (1983); **B197**, 446 (1982); J. Collins, D. Soper, and G. Sterman, *ibid.* **B250**, 199 (1985).

[40] P. Arnold and R. Kauffman, Nucl. Phys. **B349**, 381 (1991).

[41] P. B. Arnold and M. H. Reno, Nucl. Phys. **B319**, 37 (1989).

[42] C. T. H. Davies and W. J. Stirling, Nucl. Phys. **B244**, 337 (1984); C. T. H. Davies, B. Webber and W. J. Stirling, *ibid.* **B256**, 413 (1985).

[43] G. Ladinsky and C. P. Yuan, Phys. Rev. D **50**, 4239 (1994).

[44] A. D. Martin, R. G. Roberts, and W. J. Stirling, Phys. Rev. D **50**, 6734 (1994); A. D. Martin, R. G. Roberts, and W. J. Stirling, *ibid.* **51**, 4756 (1995).

[45] The definition employed here is related to the definition of V. Barger and R. Phillips, *Collider Physics* (Addison-Wesley, New York, 1987), p. 159, by $\mathcal{F} = 2\tau(d\mathcal{L}/d\tau)$, with $\tau = x_1 x_2$. Note that this parametrization of the parton luminosity is different (by a factor $1/m$) from what has been done by other experiments [9,13,15].

[46] H. Plothow-Besch, PDFLIB User's Manual, CERN Program Library entry W5051, Version 5.02 (1994).

[47] H. L. Lai *et al.*, Phys. Rev. D **51**, 4763 (1995).

[48] F. A. Berends and R. Kleiss, Z. Phys. C **27**, 365 (1985).

[49] In approximately 40% of all *W* boson events in the data sample there is at least one jet produced with the *W* boson with $p_T > 8$ GeV/c.

[50] CDF Collaboration, F. Abe *et al.*, Phys. Rev. Lett. **74**, 850 (1995).

[51] W. K. Tung (private communication).

[52] D. Wackeroth and W. Hollik, Phys. Rev. D **55**, 6788 (1997); U. Baur *et al.*, *ibid.* **56**, 140 (1997).

[53] Yung-Su Tsai, Rev. Mod. Phys. **46**, 815 (1974); **49**, 421(E) (1977).

[54] D. Bardin *et al.*, Z. Phys. C **44**, 493 (1989); Comput. Phys. Commun. **59**, 303 (1990); Nucl. Phys. **B351**, 1 (1991); Phys. Lett. B **255**, 290 (1991); and CERN-TH 6443/92 (1992).